Tailoring the Microstructure of 2D Molecular Sieve Materials for Thin Film Applications

A DISSERTATION

SUBMITTED TO THE FACULTY OF

UNIVERSITY OF MINNESOTA

BY

Meera Hemant Shete

IN PARTIAL FULFILLMENT OF THE REQUIREMENTS

FOR THE DEGREE OF

DOCTOR OF PHILOSOPHY

Prof. Michael Tsapatsis, Advisor

May 2018

Acknowledgements

I gratefully acknowledge the immense contributions of several people in my PhD journey at the University of Minnesota.

First and foremost, my deepest gratitude and thanks goes to my advisor, Prof. Michael Tsapatsis for giving me an opportunity to work on this dissertation. It has truly been an honor for me to work under his guidance. His enthusiasm, love for science and rigor has always inspired me to give my best. I would like to thank him for always supporting me and being patient with me. It was his constant support that motivated me to keep working even at times when things were challenging. Working with him has taught me to give explicit attention to experimental details, critically analyze the results and to never stop asking questions. Many thanks to him for always being thoughtful about my future career plans and for giving me several opportunities to advance my career. I am indeed fortunate to have found a lifetime mentor in Prof. Tsapatsis.

I would like to thank Prof. Alon McCormick, Prof. Paul Dauenhauer and Prof. Andreas Stein for serving on my doctoral committee and for critically reviewing my thesis.

I have been fortunate to have had the opportunity to collaborate with different researchers on this dissertation. I would like to thank Prof. Jeffrey Rimer and Dr. Manjesh Kumar (University of Houston) for collaborating with me on the *in situ* AFM project; Dr. Zachary Smith (University of California, Berkeley) for advising me on the fabrication of mixed matrix membranes and for several helpful discussions; Dr. Jonathan Bachman (University of California, Berkeley) for performing the mixed gas permeation measurements; Prof. Jeffrey Long (University of California, Berkeley) for his guidance on the MOF nanosheet

project; Prof. Benjamin Stottrup (Augsburg College) for his help with the Langmuir trough experiments.

I would like to thank all the past and present members of the Tsapatsis group for always being helpful and for a wonderful time in the lab and office. I would especially like to thank Dr. Neel Rangnekar for collaborating with me on several projects, including the Langmuir trough project and the in-plane XRD experiments at Argonne National Laboratory; Prashant Kumar for diligently performing the high resolution TEM measurements. Many thanks to Dr. Kumar Varoon Agrawal and Dr. Berna Topuz for training me on several experimental techniques and for helping me get started in the lab. Their constant support and guidance helped me acquire skills sets that were invaluable to me throughout my PhD journey and will remain with me lifelong. I would also like to thank Dr. Han Zhang, Dr. Donghun Kim, Dr. Limin Ren, Dr. Xiaoli Ma, Dr. Garrett Swindlehurst, Dr. Balu for their constant support and help. A special thank you to my present and past officemates – Dr. Maryam Khaleel, Dr. Aparna Iyer, Dr. Sabrina Conrad, Dandan Xu and Feng Xue for always maintaining a lively atmosphere in the office and for many intellectual as well as fun conversations.

The exceptional support provided by the Characterization facility at the University of Minnesota is gratefully acknowledged. I would like to thank Dr. Mike Manno and Dr. Linda Sauer for helping me with the in-plane XRD experiments; Dr. Nick Seaton, Dr. Han Seung Lee and Dr. Jason Myers for their help with the microscopy experiments; Dr. Greg Haugstad for his help with AFM; Dr. Fang Zhou for performing the microtomy experiments for me. I would also like to thank the staff at Argonne National Laboratory for their help with the XRD experiments.

I would like to thank the faculty at the Department of Chemical Engineering and Materials Science, especially Prof. Andre Mkhoyan, Prof. Chris Macosko, Prof. Bharat Jalan, Prof. Lorraine Francis. Special thanks to my mentors and professors from my undergraduate institute – Prof. Ashwin Patwardhan, Prof. Anand Patwardhan, Prof. Sunil Bhagwat and Prof. Aniruddha Pandit for always supporting me and believing in me. Many thanks to Dr. Cordell Hardy for his mentorship and for his guidance on my future career plans.

I would like to acknowledge the University of Minnesota Graduate School for the doctoral dissertation fellowship.

Many thanks to Julie Prince, Teresa Bredahl, Susan Wermager and Daniel Williams for their support with the administrative matters.

A huge thank you to all my friends – Gauri Nabar, Kristeen Joseph, Manjiri Moharir, Sajna Hameed, Akash Arora, Mansi Shah, Shreyas Bhaban, Vaidyanathan, Shankali Pradhan, Bhumika Sule, Karan Gupta, Pooja Jambunathan, Arpan Bandopadhyay, Sampada Koranne, Aditi Potdar, Manish Yadav for their constant support and wonderful camaraderie.

Finally, I would like to thank my family without whose support and motivation this would not have been possible. I am forever indebted to my parents Hemant Shete and Ashwini Shete for always believing in me and motivating me to give my best. It is their unconditional love and care that has made me into the person I am today. Special thanks to my brother Mihir Shete for always being there for me.

Dedicated to my parents Hemant and Ashwini Shete

Abstract

Zeolites and metal organic frameworks (MOFs) are microporous materials, with pores of molecular dimensions, that are of interest in a variety of applications including catalysis, adsorption, ion-exchange, separation membranes etc. With a global need of developing clean energy resources and reducing the carbon footprint of existing processes, they are being increasingly sought after as catalysts for the conversion of biomass to chemicals and fuels, in separation membranes to replace the existing energy intensive industrial separations with clean energy-efficient processes and for capture and storage of carbon dioxide. Their performance in these applications depends mainly on their pore size but also on our ability to tune their microstructure (crystal morphology and size, orientation, phase purity, defect densities etc.) as desired for an optimum performance. Recent advances in synthesis of molecular sieve materials have resulted in the development of advanced morphologies such as hierarchical materials, core-shell catalysts, two-dimensional nanosheets and thin films. However, a lot of the reports in the literature focus on conventional crystals and studies focusing on nanoscale crystal growth control are still in their infancy. This dissertation focuses on developing synthetic methods that will enable us to tailor the microstructure of 2D molecular sieve materials at a nanoscale approaching single-unit-cell dimensions with a goal of optimizing their performance in thin film applications. A novel coating technique was applied to isolate 2D MFI zeolite nanosheets and form monolayer coatings on versatile supports such as Si wafers. Using this as a prototype, growth conditions were developed that lead to unprecedented control of zeolite MFI growth at a scale approaching single-unit-cell dimensions. It was demonstrated that these growth conditions are robust enough and can be used to grow zeolite MFI crystals of varied sizes and morphology. It also enabled us to precisely control the microstructure of MFI thin films leading to the development of a material that had one of the lowest reported dielectric constant. Furthermore, the nanoscale growth control also allowed us to tailor the design of hierarchical catalysts by controllably thickening the zeolite domains in them and open opportunities to design multifunctional catalysts. A scalable and direct synthesis of Cu(BDC) MOF nanosheets was developed. Hybrid nanocomposites incorporating the MOF nanosheets in polymer matrices were fabricated which demonstrated significantly improved performance for CO_2/CH_4 separation.

Table of Contents

List of Figures

List of Tables

Chapter 1: Introduction

1.1 Motivation

Developing clean energy resources while reducing the carbon footprint of existing processes is necessary to meet the world's energy demands in a sustainable way[1–3]. At the cornerstone of these endeavors is the development of advanced materials that can 1) convert the non-fossil fuel based feedstock to useful chemicals[4–6], 2) replace the existing energy-intensive industrial separations with clean, energy-efficient membrane-based separations[7–9] and 3) mitigate carbon emissions by facilitating capture of CO_2[10–12]. Nanoporous materials – zeolites and metal organic frameworks (MOFs), currently used in catalysis, separation membranes and gas storage, have a tremendous potential for successful application in all the above-mentioned areas.

Zeolites are inorganic crystalline porous materials made of silicon-oxygen and aluminum-oxygen tetrahedral units[13,14] (**Figure 1-1a**). Based on the arrangement of tetrahedral units, different zeolite structures are formed and so far, 235 different framework types have been reported[15]. Depending on the framework type, the channel system and pore widths differ. MOFs on the other hand are organic-inorganic hybrid materials built from organic linkers and inorganic metal nodes[16,17] (**Figure 1-1b**). The combination of different organic linkers with metal nodes makes MOFs very versatile giving researchers the opportunity to tune their functionality and pore size[17].

The pore size and channel width of zeolites and MOFs are on the order of molecular dimensions, making them highly attractive in catalysis, molecular sieving membranes, gas storage and chemical sensing. Traditionally, zeolites have been used as catalysts in

petroleum refining[14,18,19] and more recently have been used for conversion of biomass to fuels and chemicals[20–24]. Zeolite membranes have demonstrated exceptionally high performance in the separation of close boiling isomers such as *para*-xylene from *ortho*-xylene (*para*-xylene is used as a precursor in the manufacture of PET bottles), separation of *n*/*i* butane, separation of alcohol-water mixtures[25–29]. More recently, zeolite thin films are being increasingly studied for their applications in low-*k* dielectrics[30–32] and in chemical sensing[33–35]. Along the lines of zeolites, MOFs are also being studied for their application in catalysis[36,37]. MOF adsorbents have demonstrated exceptional potential for carbon dioxide capture[38,39] and efforts are on the way for their large-scale deployment. MOF membranes and hybrid nanocomposites incorporating MOF particles in polymer matrices have tremendous potential for applications in gas separations[40–44].

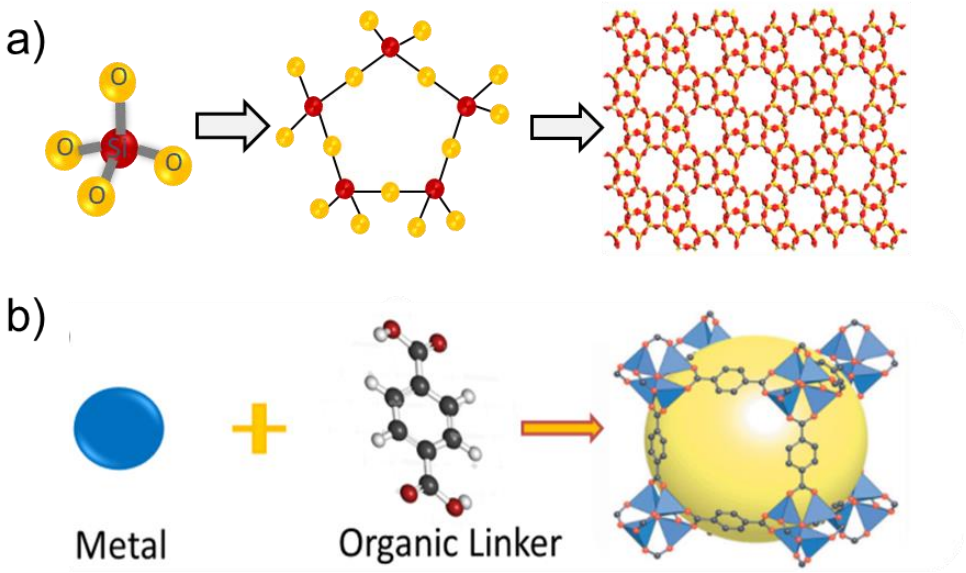

Figure 1-1: (a) Schematic showing build-up of a zeolite structure from the tetrahedral building blocks and primary units. (b) Schematic depicting the building blocks of a MOF framework.

The performance of zeolites and MOFs in the above-mentioned applications depends mainly on their pore size and channel widths but also on precise tailoring of their crystal shape and size. As an example, for optimizing their performance in catalysis and separations, over the years there has been progress in tailoring the crystal size from micron-sized crystals[45] to nanocrystals[46,47], in order to reduce the diffusion path length for molecules. Recent advancements in the synthesis and crystallization of molecular sieve materials have resulted in the development of advanced morphologies such as hierarchical materials[48–50], core-shell catalyst materials[51], two-dimensional nanosheets[26,40,52] and thin films with desired pore orientation and reduced defect densities[27,53]. These developments suggest that a nanometer level growth control of molecular sieve crystals is desirable. However, a lot of the reports in the literature focus on conventional crystals and studies focusing on developing methods to control crystal growth with a nanometer precision are still in their infancy. This dissertation will focus on developing synthetic methods that will enable us to tailor the microstructure of 2D molecular sieve materials at a nanoscale approaching single-unit-cell dimensions.

1.2 Background

Among the different zeolite frameworks, zeolite MFI is the most widely used as its pore size of around 5Å lies in the range of several industrially relevant molecules[54,55]. The structure of zeolite MFI is shown in **Figure 1-2**. It has straight channel pores along the crystallographic *b*-axis and sinusoidal channels run along the crystallographic *a*-axis. The *b*- and *a*- channels are interconnected, allowing diffusion of molecules along the *c*-direction. Owing to the straight channel pores along the *b*-axis, a *b*-orientation for MFI membranes and thin films is highly desirable. Zeolite MFI was first discovered by Mobil

scientists in 1970s[23,56], thereafter considerable research efforts have been directed towards tailoring its crystal morphology and size. Starting from micron-sized coffin shaped crystals developed by Mobil in 1970s, to nanocrystals of MFI that were developed in the 2000s by confined synthesis within three-dimensionally ordered mesoporous carbons[57–59], the morphology has now evolved to two-dimensional nanosheets that were obtained by exfoliation of a layered precursor[26].

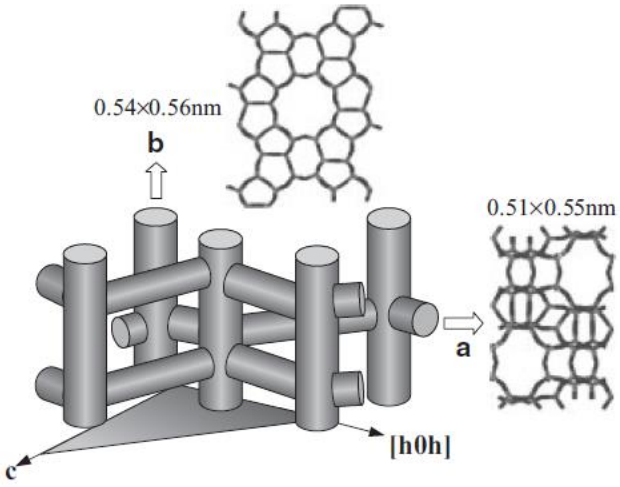

Figure 1-2: Schematic depicting structure of zeolite MFI

(Adapted from Z. Lai et.al., *Adv. Funct. Mater*. 2004, 14, 716-729)

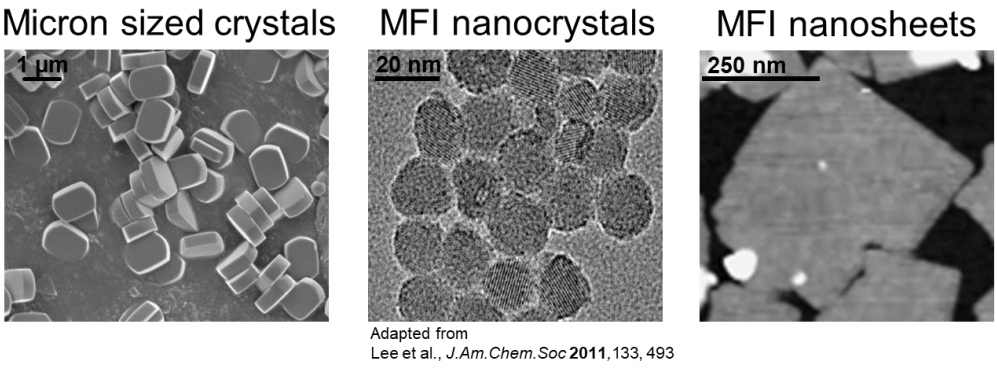

Figure 1-3: Morphology evolution of MFI zeolite over the years

2D MFI nanosheets have a thickness of 1.5 unit cells (3.2 nm) along the crystallographic *b*- axis. This coupled with large lateral dimensions gives them a high aspect ratio and shorter diffusion lengths making them ideal for fabrication of MFI thin films and membranes. Furthermore, since they are precisely 1.5 unit cells thick, their surface termination is better defined as compared to conventional crystals which opens opportunities to study their fundamental growth, dielectric and transport properties[52].

2D MFI nanosheets are synthesized via a top-down approach involving exfoliation of the layered precursor as shown in **Figure 1-4**. A di-quaternary ammonium structure directing agent (SDA) is first synthesized which plays the role of a dual template in the crystallization of multilamellar silicalite-1[49]. The di-ammonium head group of the surfactant directs the structure of MFI zeolite whereas the long hydrophobic tail restricts growth along the *b*-axis leading to the formation of 3 nm thick layers separated by surfactant micelles in the intergallery space (**Figure 1-4a**).

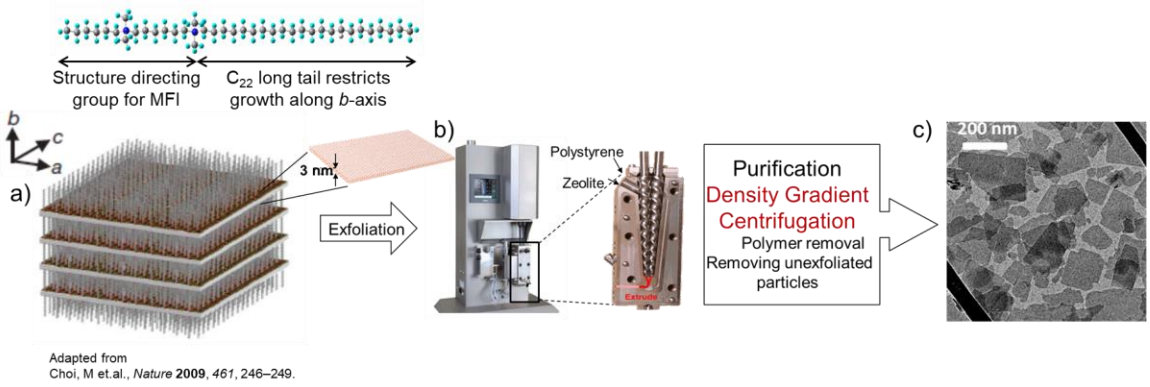

Figure 1-4: Schematic of the top-down approach for synthesis of MFI zeolite nanosheets. (a) Schematic of multilamellar silicalite-1. (b) Polymer melt extrusion equipment used for exfoliation. (c) TEM image of MFI nanosheets suspended in octanol.

The multilamellar zeolite powder is then exfoliated using a polymer melt extrusion technique[26] (**Figure 1-4b**). The nanocomposite obtained is purified using density gradient centrifugation to separate the exfoliated nanosheets from unexfoliated thicker particles[60]. The purified suspension of nanosheets is used in thin film fabrication (**Figure 1-4c**). Very recently, a bottom-up approach to synthesize 5.5 nm thick MFI nanosheets was developed which is more facile as it consists of fewer processing steps and results in a better yield of nanosheets[28].

Most commonly, the fabrication of 2D nanosheets membranes/films is a two-step process (schematic in **Figure 1-5**) involving 1) deposition of nanosheets on an appropriate porous (such as ceramic silica or alumina support, or polymer supports) or nonporous support (such as Si wafer, conductive gold or ruthenium wafers) in a correct orientation such that their pores are perpendicular to the support surface, 2) followed by subjecting them to a mild growth step that preserves their orientation and laterally stitches their edges to fill any interparticle voids or defects while minimizing the increase in thickness (as thinner the membranes, higher the throughput). Step 1 of this process requires availability of purified, well-dispersed and well characterized suspensions of 2D nanosheets in suitable solvents along with development of coating techniques that will ensure quantitative transfer of nanosheets on versatile supports.

Traditionally, a vacuum deposition technique is employed to obtain deposits of nanosheets on porous supports (commonly referred to as seed coatings). While it can result in a quantitative transfer of nanosheets leading to seed coatings that are as thin as few nanometers thin, vacuum deposition is limited to coating on porous supports. Furthermore, it is very difficult to isolate monolayers of nanosheets using vacuum deposition. To address

this issue, in **Chapter 2**, the application of Langmuir trough deposition techniques to 2D MFI nanosheets is discussed. Monolayer coatings are obtained on versatile supports such as Si wafers.

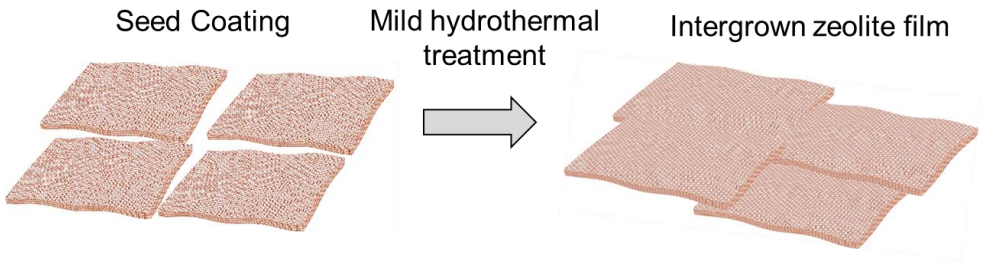

Figure 1-5: Schematic depicting the two-step process that is commonly employed for fabrication of 2D nanosheets thin films and membranes. (Adapted from Agrawal, K. V., 2013, Doctoral dissertation, University of Minnesota)

Step 2 of the process requires development of growth conditions that will preserve the preferred orientation of the seed coating and favor in-plane vs. out-of-plane growth to avoid excessive film thickening. Considerable research efforts have been directed towards achieving this goal. The most widely applied MFI growth and intergrowth conditions use tetrapropylammonium hydroxide (TPAOH) as the SDA; however, it is well established that growth with TPAOH is prone to the commonly observed 90 degree rotational intergrowth (twinning) resulting in misorientation of the starting crystals. To suppress twin formation and preserve orientation of the seed coating, different strategies have been reported and include use of trimer-TPAOH[25], precrystallization of the growth solution[61], use of microwave irradiation[62] and use of very low concentrations of TPAOH[63]. However, as will be shown in **Chapter 3** these conditions are not robust enough to be transferred to MFI crystals of different size and shape, supported on different substrate types.

More recently, a gel less growth method[64] was developed for the fabrication of oriented MFI thin films; nanosheet membranes demonstrating exceptionally high performance were reported using this method[27,28]. The gel less method relies on the use of the support as a source of silica for intergrowth of the seed coating. Support dissolution is enabled by impregnation of the SDA. This method is therefore limited to supports with a top silica layer. Thus, there is a need for developing growth conditions that would allow us to tailor the microstructure of MFI crystals of varied morphologies supported on versatile substrate types. **Chapter 3** addresses this issue and discusses the development of synthesis conditions that allow nanoscale control of zeolite MFI growth.

1.3 Outline

Thus, in a nutshell, the outline of this dissertation is as follows:

In Chapter 2, application of Langmuir trough deposition techniques to 2D MFI nanosheets is discussed. The MFI nanosheets are treated using a novel acid treatment procedure to make them surface active, following which Langmuir trough deposition is used to quantitatively transfer monolayer of nanosheets on versatile supports such as Si wafer. Such an isolation of the 2D MFI nanosheets on non-porous flat supports allowed for their structure characterization using in-plane X-ray diffraction and further opened avenues to study their structure using surface characterization techniques.

In Chapter 3, the prototype developed in Chapter 2 was used for developing growth conditions that allowed homoepitaxial growth of MFI zeolite with a nanoscale control. The slow and controllable growth conditions reported in this chapter, enable us to tailor the microstructure of MFI thin films and hierarchical catalysts at a scale approaching single-

unit-cell dimensions. Further, it was demonstrated that these growth conditions are robust enough and can be transferred for growth of MFI crystals having varied morphologies supported on versatile substrate types.

In Chapter 4, a direct synthesis of Cu(BDC) MOF nanosheets is described which can be easily scaled up. Using in-plane X-ray diffraction and electron microscopy, the structure of Cu(BDC) nanosheets was characterized in detail revealing the presence of a prominent structural disorder. The Cu(BDC) nanosheets were incorporated in a polymer matrix to form hybrid nanocomposites which demonstrated significantly improved performance for the separation of CO_2/CH_4 over that of the neat polymer.

The major conclusions of this dissertation are summarized in the concluding remarks with a note on possible future work directions.

Chapter 2: Langmuir Schaefer Deposition of 3 nm Thick MFI Zeolite Nanosheets

Parts of this chapter are published as:

N. Rangnekar*, M. Shete*, K.V. Agarwal, B. Topuz, P. Kumar, Q. Guo, I. Ismail, A. Alyoubi, S. Basahel, K. Narasimharao, C.W. Macosko, K. A. Mkhoyan, S. Al-Thabaiti, B. Stottrup and M. Tsapatsis., *Angew. Chem Int. Ed.* 54, 6571-6575 (2015).

* Equally contributing authors

Reproduced with permission from Wiley VCH.

2.1 Chapter Overview

In this chapter, application of a novel coating method to isolate monolayers of MFI zeolite nanosheets on Si wafers is described. Stable suspensions of zeolite nanosheets (3 nm thick MFI layers) were prepared in ethanol following acid treatment, which partially removed the associated organic structure-directing agent. Nanosheets from these suspensions displayed surface activity and could be dispersed at the air-water interface and transferred to silicon wafers using Langmuir Schaefer deposition. Using layer-by-layer deposition, a control on the coating thickness was demonstrated. In-plane X-ray diffraction (XRD) revealed that the deposited nanosheets contract upon calcination similar to bulk MFI crystals. Different methods for secondary growth resulted in preferentially oriented thin films of MFI, which had sub-12 nm thickness in certain cases. Upon calcination, there was no contraction detectable by in-plane XRD, indicating well-intergrown MFI films that are strongly attached to the substrate.

2.2 Introduction

2D zeolites, nanosheets with thickness comparable to the unit-cell-dimensions of the corresponding structure type (for a list of structure types see http://www.iza-online.org),[65]

open exciting opportunities for traditional uses in catalysis and separations[49,66–72] and hold promise for emerging applications of zeolite films as membranes,[8] low dielectric constant materials,[73,74] anti-corrosion coatings, etc.[74] Fabrication of thin films of 2D zeolites relies on: (i) the availability of suspensions that exhibit colloidal stability, and are free of amorphous and non-exfoliated contaminants; and (ii) development of deposition techniques by which the suspended zeolite nanosheets can be quantitatively transferred on various supports to form oriented thin coatings.

Following the discovery of multi-lamellar MFI zeolite by Ryoo and co-workers,[49] we used a polymer-melt-compounding technique[26] (for exfoliation) combined with density gradient centrifugation (for purification) to prepare suspensions of exfoliated 2D MFI nanosheets in toluene and octanol.[75-60] In our earlier work, the octanol and toluene suspensions were used to form nanosheet deposits on porous supports by filtration.[26,60] Deposition by filtration ensured transfer of all zeolite nanosheets from the suspension to the surface of the support. Such quantitative transfer from suspension to support, without nanosheet loss, is essential because high quality 2D zeolites cannot be obtained currently in large quantities. However, the filtration approach is only applicable to porous supports. Furthermore, a uniform coating with thickness on the order of a single-layer of nanosheets is not possible by this technique. To overcome these drawbacks, we investigated the application of the Langmuir-Schaefer (LS) deposition technique for the formation of MFI nanosheet coatings.

Deposition from a Langmuir trough is a well-known method used to obtain monolayers of surfactant molecules[76–78] and it has been used to deposit particles including zeolites[79–83] and various 2D non-zeolitic materials.[84,85] To employ the LS deposition, we started from a

nanosheet suspension in octanol prepared according to our previously reported procedure.[60] The nanosheets were then transferred to ethanol and subjected to an acid treatment procedure, reported earlier by Corma and co-workers for the removal of organic structure-directing (OSDA) agents from zeolites.[86] This acid treatment resulted in partial removal of the long-chain OSDA used in the synthesis of multi-lamellar MFI and allowed for the formation of stable suspensions in ethanol. Nanosheets could then be introduced at the air-water interface, and transferred to silicon wafers by using the Langmuir-Schaefer horizontal lifting technique.[77] Secondary growth of these monolayers resulted in intergrown, preferentially oriented, sub-12 nm films, which were firmly attached to the support and did not show in-plane contraction upon calcination. On the other hand, non-intergrown multi-layers, could slide and contract upon calcination. LS provides the opportunity to coat monolayers of 2D zeolites such as MFI and MWW nanosheets. Secondary growth can allow formation of sub-12 nm, crack-free, intergrown zeolite films, of which to the best of our knowledge, there are no reports in the literature.

2.3 Experimental

2.3.1 Synthesis and exfoliation of multilamellar silicalite-1

Multilamellar silicalite-1 (ML-MFI) was synthesized following the procedure reported in literature.[26,49,60] First, the bromide form of the di-quaternary ammonium structure directing agent ($C_{22}H_{45}$-N^+ $(CH_3)_2$-C_6H_{12}-N^+ $(CH_3)_2$-C_6H_{13} $(2Br^-)$) or $C_{22\text{-}6\text{-}6}Br_2$ was synthesized following the alkylation reaction of *N, N, N', N'*-tetramethyl-1,6,-diaminohexane with 1-bromodocosane followed by alkylation of the product with 1-bromohexane. Hydroxide form of the SDA ($C_{22\text{-}6\text{-}6}(OH)_2$) was obtained by ion-exchange of the bromide form using silver (II) oxide (predominantly silver (II) oxide, Sigma Aldrich). For the synthesis of ML-

MFI, tetraethylorthosilicate (98%, Sigma Aldrich) was hydrolyzed in the aqueous solution of $C_{22\text{-}6\text{-}6}(OH)_2$ for a day, to obtain a gel with composition 100 SiO_2: 15 $C_{22\text{-}6\text{-}6}(OH)_2$: 4000 H_2O. The gel was then transferred into Teflon-lined stainless steel autoclaves and set for hydrothermal synthesis under rotation at 150º C for 8 days. The product obtained was washed and dried. Exfoliation was performed using polymer-melt compounding[26]. A mixture of ML-MFI (0.6 g) and polystyrene (14.4 g; Piccolastic A75 hydrocarbon resin, M_w 1300 g/mol) was fed to a twin screw extruder (DSM Xplore micro compounder) and allowed to mix sequentially at 120º C for 15 min, 95º C for 15 min and 75º C for 45 min and then extruded at 80º C to obtain the polymer-zeolite nanocomposite containing exfoliated 2D-MFI nanosheets.

2.3.2 Acid treatment of MFI nanosheets

MFI nanosheet suspensions in octanol were prepared according to the previously reported procedure.[60] The octanol suspension was then centrifuged (Beckman Coulter, Model: Avanti J-20 XP equipped with JA25.50 rotor) at 40000 g for 3 hours and the supernatant was discarded. The resulting cake was dispersed in approximately 50 mL filtered ethanol (200 proof, Decon Labs). The dispersion was centrifuged at 40000 g for 3 hours and the supernatant was discarded. This ethanol washing step was repeated two more times. The final cake was dispersed in 20 mL of filtered ethanol by vortexing (Fisher Scientific vortex mixer). For the first step of acid treatment, 0.098 g of H_2SO_4 (98%, EMD Chemicals) was taken in a 50 mL glass reaction vial. The nanosheet dispersion in ethanol was then added to it. The vial was sealed and placed in an oil bath set to 80º C for 16 hours under stirring.

Following this, the vial was cooled and uncapped. The contents were centrifuged at 40000 g for 3 hours and the supernatant was discarded. This was followed by an ethanol washing

step, as before. Further, 7.89 g (10 mL) of filtered ethanol was added to the cake and dispersed by vortexing. 1.5 g of HCl solution in water (1 M, Sigma-Aldrich) was taken in a 50 mL glass vial followed by the addition of the nanosheet suspension. 10 mL of filtered heptane (anhydrous 99%, Sigma-Aldrich) was then added to the vial. The vial was capped and placed in an oil bath at 90º C for 16 hours under stirring.

On completion of this step, the vial was cooled and the contents were centrifuged at 40000 g for 3 hours. The supernatant was discarded and 40 mL ethanol was added to the cake followed by vortexing. A drop of the resulting suspension was deposited on a holey carbon grid for analysis by TEM.

2.3.3 Langmuir-Schaefer deposition (LS)

Commercially available 4-inch Si wafers (Silicon Quest International, Inc.) in <100> orientation were used as substrates. They were either used as-purchased or after subjecting them to thermal oxidation. For the latter, the Si wafers were heated at 900-1000º C in an oxygen atmosphere in a Tylan tubular furnace in order to grow 50 nm oxide. The wafers were then cut into 1 cm x 1 cm squares using a wafer saw (Disco DAD 2H/6T) equipped with a diamond blade (Disco NBC-ZH2030-SE). The substrates were sonicated in DI water (generated by EMD Millipore Elix 5 water purifier) in a bath sonicator (Branson 5510R-DTH, 135 Watts) for about 5 min, dried at ambient temperature and used for LS experiments.

In a typical LS experiment, 1.5 mL of nanosheet suspension in ethanol was carefully deposited on the air-water interface in a Langmuir barrier trough (Nima Liquid-Liquid trough with IU4 interface and Nima LB dipping mechanism, maximum area 120 cm^2,

minimum area 23 cm^2) using a micropipette. After the deposition was completed, the trough was left without disturbance for 30 min in order to allow the ethanol to evaporate.

Following this, the trough was set to attain a specific surface pressure and the trough barriers were compressed such that the trough area reduced at a speed of 30 cm^2/min. Once the desired pressure was attained, a previously prepared Si substrate, mounted horizontally on the dipper (NIMA), was lowered at a speed of 1 cm/min until it just touched the air-water interface. Once contact was made, the Si substrate was lifted upwards at the same speed. The substrate was detached from the dipper and left to dry. Following the coating process, the surface pressure dropped by 5-10 mN/m. The barriers were further compressed in order to compensate for this. The coating process was then repeated using another substrate. Multilayer coatings were obtained by repeating the coating procedure on the same substrate for the desired number of cycles.

In order to collect surface pressure - area isotherms, the barriers were compressed and expanded between the limits of maximum and minimum area for multiple cycles, without taking coatings.

2.3.4 Secondary growth

Prior to secondary growth, the nanosheet-coated substrates were first calcined at 500º C for 6 hours in 150 mL/min air flow in order to remove the OSDA.

2.3.4.1 TPA-silica sol-based growth

Clear sol secondary growth was performed according to a previously reported procedure.[61] The growth solution was prepared by sequentially adding tetrapropylammonium hydroxide (TPAOH, 1M Sigma Aldrich), tetraethylorthosilicate (TEOS, 98% reagent grade Sigma

Aldrich) to distilled water in a molar composition of 5TEOS:1TPAOH:1000H_2O. The solution was hydrolyzed at room temperature for 15 hours under stirring. After hydrolysis, it was filled in a HF-cleaned Teflon liner, sealed in a stainless steel autoclave and placed in an oven set to 150º C for 2 hours. This pretreated solution was filtered using a 0.2 μm GHP Acrodisc syringe filter (Pall Corporation) into a HF-cleaned Teflon lined autoclave. Calcined nanosheet coating deposited on as-purchased silicon wafer was placed vertically in the solution using a Teflon holder and secondary growth was carried out at 90º C for 5 hours. The autoclave was then cooled and the substrate was removed, washed for 2-3 min with DI water, dried at ambient conditions in air and characterized.

2.3.4.2 TEAOH gel growth

Gel growth was carried out according to a previously reported procedure.[87] The gel composition used was 4TEOS:1.92TEAOH:0.36$(NH_4)_2SiF_6$:40H_2O (molar ratios). The gel was prepared by mixing 2/3 of the total amount of TEAOH (35% w/w Alfa Aesar) and DI water, followed by the addition of TEOS (98%, Sigma Aldrich) to the mixture and stirring with a magnetic stirrer for 30 min. In a separate container, the remaining TEAOH, DI water and $(NH_4)_2SiF_6$ (Sigma Aldrich) were mixed until complete dissolution of $(NH_4)_2SiF_6$, about 30 min. The contents of the second container were quickly added to the first under vigorous stirring. After the mixture solidified, it was left for 6 hours under static conditions for aging. 100 g of the mixture was then blended in a 500 mL glass beaker with a handheld food blender (KitchenAid) for about 10 min. Approximately 10 g of the blended mixture was loaded into the bottom of a Teflon liner. Calcined nanosheet coating on as-purchased silicon wafer was inserted vertically into the gel. The liner was sealed in a stainless steel autoclave and placed in an oven at 150º C for 6 hours. The autoclave was then removed

from the oven and cooled. The substrate was removed from the liner and thoroughly washed with DI water to remove any adhering gel. Following this, the substrate was soaked in 0.2 M aqueous solution of NH_4F (Sigma-Aldrich) for 6 hours to remove amorphous silica from the surface. It was then removed, washed with DI water, dried at ambient conditions in air and characterized.

2.3.4.3 Gel less growth

Gel-less growth was done according to a previously reported procedure.[64] The calcined nanosheet coating on silicon wafer with 50 nm thermally-grown oxide was spin-coated with 0.005 M TPAOH aqueous solution (prepared from 1 M TPAOH solution, Sigma Aldrich) and then placed horizontally on a Teflon holder in a Teflon-lined stainless steel autoclave. 0.2 g of 0.005 M TPAOH was added to the bottom of the liner. The autoclave was sealed and placed in a convection oven set to 220º C for 72 hours under static conditions. At the end of this period, the autoclave was removed from the oven and cooled. The substrate was then removed from the liner and characterized.

2.3.4.4 Characterization

TEM samples were prepared by drop-casting suspensions of nanosheets in octanol and acid-treated nanosheets in ethanol on TEM grids (ultrathin carbon film on holey carbon support film, 400 mesh Cu, Ted Pella). The grid was dried at room temperature and imaged. Bright-field conventional transmission electron microscopy (BF-CTEM) was performed on a FEI Tecnai G2 F30 (S)TEM with TWIN pole piece, a Schottky field-emission electron gun operating at 300 kV and equipped with a Gatan 4k × 4k Ultrascan CCD. High angle annular dark field, scanning transmission electron microscopy (HAADF-STEM) was performed at 300 kV with an incident semi-convergent angle of 19 mrad and detector

collection angles of 47.5–200 mrad on an FEI Titan™ G2 60–300 scanning transmission electron microscope (STEM). To resolve the crystal structure of MFI-zeolite nanosheets, we performed BF-CTEM and high angle annular dark-field scanning transmission electron microscopy (HAADF-STEM) imaging. Data was collected using low dose of electrons to avoid beam damage of these nanosheets, thus resulting in low signal to noise ratio (SNR) in the images. In order to improve structural visibility, BF-CTEM images were digitally processed using periodic Bragg filtering to reduce the noise and resolve the structure of MFI nanosheets.

TGA analysis was performed using a PerkinElmer TGA-7 analyzer to estimate the OSDA content of nanosheets before acid treatment. This was compared with weight loss from nanosheets before acid treatment.[60] Analysis was carried out by heating a few mg of the nanosheet cake obtained after centrifugation in air flow (100 mL/min) from 130 to 550º C (heating rate of 1º C/min) and holding the sample at 550º C for 8 hours.

Scanning electron microscopy (SEM) images of the nanosheet films were acquired using JEOL 6700 microscope operating at 1.5 kV.

For the preparation of atomic force microscopy (AFM) specimens, nanosheet coating was made by LS at 25 mN/m surface pressure on a thermally oxidized silicon wafer. The sample was calcined in air flow at 500º C for 6 hours to remove the OSDA from the pores and surface of the nanosheets. AFM was carried out in tapping mode in the repulsive regime using a Bruker Nanoscope V Multimode 8 AFM. Analysis of AFM images was done using Gwyddion 2.31 software. In order to calibrate the AFM height data, freshly cleaved muscovite mica was etched in 50% hydrofluoric acid for 4 hours to produce 2.0 nm steps on mica.[88] These steps were used as the calibration standard.

FTIR spectra were recorded in transmission mode on a Thermo Scientific Nicolet iS50 FT-IR spectrometer equipped with a liquid nitrogen cooled MCT detector. The spectrometer was purged with dry air and the spectra were acquired in the range of 4000-650 cm^{-1} and averaged over 16 scans. The data analysis was performed using Omnic software.

X-ray diffraction scans were performed using a Panalytical X'Pert Pro diffractometer in in-plane mode. The incident beam optics consisted of an x-ray lens with cross-slit collimator with beam in point focus. The diffracted beam optics consisted of a parallel plate collimator (PPC). The X-ray wavelength used was mainly Cu Kα1. Cu Kα2 stripping was done using MDI-Jade 2010 software. Scans were done in in-plane mode with 2θ varying from 22.5º to 24.5º with a step size of 0.02º and dwell time of 150 s.

The secondary grown MFI layer deposited on a silicon substrate was coated with a 150 nm gold layer before performing focused ion beam (FIB) milling. This gold coated layer was further coated with platinum to perform thinning experiments using a dual beam FEI Quanta 200 3D FIB-SEM instrument. Thinning was done using a Ga-As ion beam. The thinned sample was analyzed in an aberration corrected FEI-Titan transmission electron microscope (TEM). High angle annular dark field scanning TEM (HAADF-STEM) imaging was done at <30 pA electron beam current at 17 mrad convergence angle. Spatially resolved STEM energy dispersive X-ray imaging performed on a 150 nm x 250 nm section revealed that the SiO_2 + MFI layer is ~ 50 nm thick. It is not possible to distinguish between SiO_2 and MFI zeolite since the elemental composition of both layers is same.

2.4 Results

Following acid treatment (details given in section 2.3.2), removal of OSDA ($C_{22}H_{45}$-$N^+(CH_3)_2$-C_6H_{12}-$N^+(CH_3)_2$-C_6H_{13}.($2OH^-$)) was quantified by thermogravimetric analysis (TGA) of zeolite nanosheets. Specifically, the nanosheet cake recovered by centrifugation was analyzed by TGA after acid treatment and compared with TGA from nanosheet cake prior to acid treatment (**Figure 2-1**). Before acid treatment, the zeolite nanosheets contain ~29 wt% OSDA, the majority of which is expected to reside inside their straight pore channels.[60] After acid treatment, the amount of OSDA is reduced to less than ~8 wt%. The partial removal of OSDA is also indicated by a color change of the nanosheet cake from yellow to white. We believe that the acid treatment procedure reduces the lipophilicity of nanosheets and allows for their transfer out of octanol to form a stable suspension in ethanol.

Figures 2-2a and 2-2e show transmission electron microscopy (TEM) images of nanosheets, deposited on carbon coated copper TEM grids, before and after acid treatment, respectively. Nanosheets deposited from both octanol and ethanol suspensions appeared well dispersed. In contrast, nanosheets suspended in ethanol without acid treatment formed agglomerates (not shown). High-resolution TEM images (**Figure 2-2b and 2-2f**) and electron diffraction patterns (**Figure 2-2c and 2-2g**) showed that the acid treatment process does not alter their crystal structure. More detailed crystallographic investigations regarding the structural integrity and thickness of the nanosheets were performed by diffraction tilting experiments in the TEM.[89] The experimental and simulation data shown in Figures **2-2d** and **2-2h**, confirmed that the nanosheets were 1.5 unit cells thick (which

corresponds to approximately 3 nm) and further confirm that the crystalline structure of MFI was preserved.

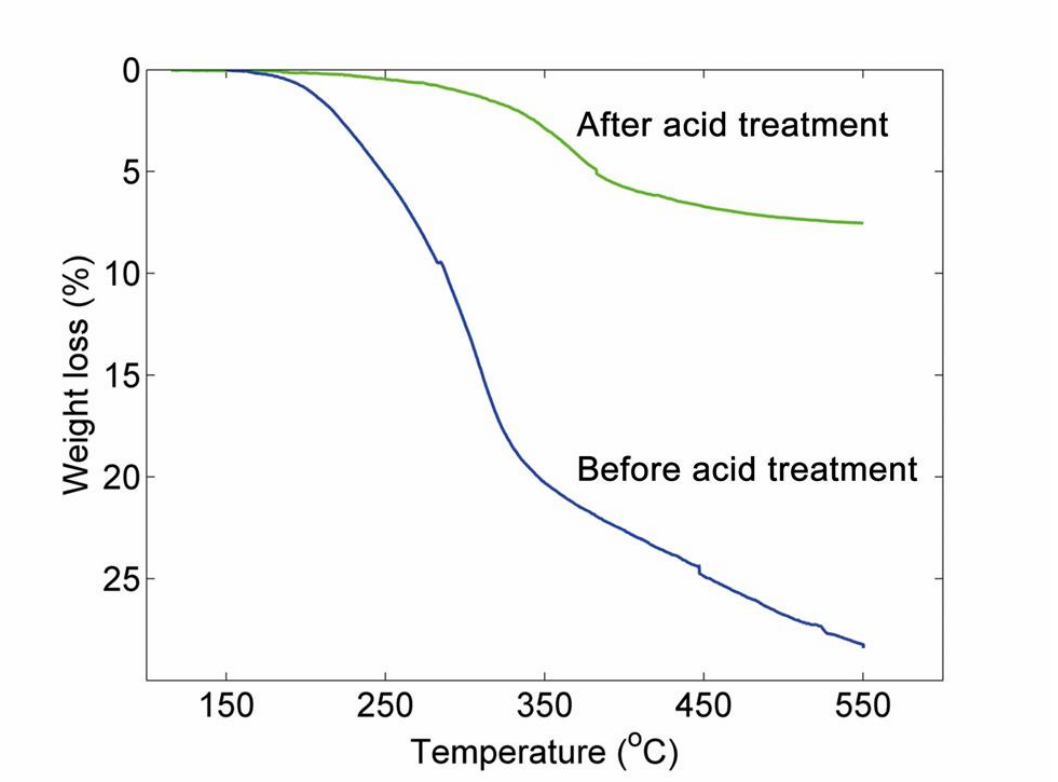

Figure 2-1: TGA analysis of as-synthesized nanosheets without acid treatment (obtained from Ref. 60) and acid-treated nanosheets. Acid-treated nanosheets show a weight loss of about 8% compared with about 29% for as-synthesized nanosheets.

Although a major fraction of the OSDA was removed, the remaining OSDA appears to be occluded in the micropores as Ar-adsorption measurements failed to detect any microporosity (data not shown). Moreover, the presence of the remaining OSDA makes the nanosheets retain some hydrophobicity which prohibits their dispersion in water.

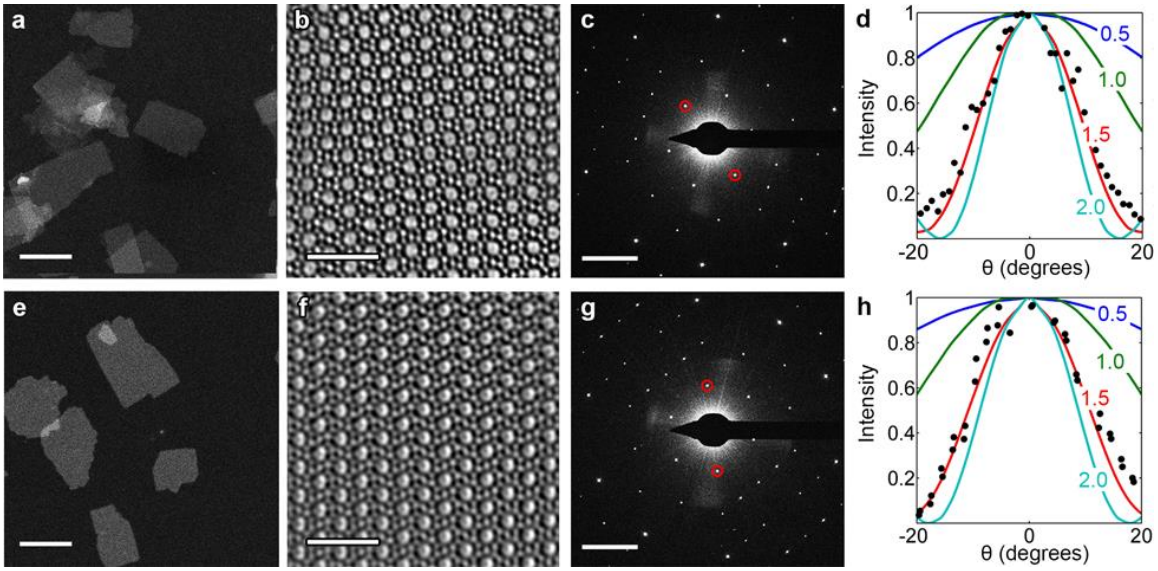

Figure 2-2: Top row: MFI nanosheets before acid treatment (deposited from octanol); Bottom row: MFI nanosheets after acid treatment (deposited from ethanol). (a),(e) Low magnification HAADF-STEM images of MFI nanosheets supported on a ultrathin carbon films showing uniform thickness of nanosheets; scale bars: 500 nm; (b),(f) High resolution Bragg filtered CTEM images of MFI nanosheets; scale bars: 2 nm; (c),(g) [010] zone axis diffraction pattern with the red circles highlighting (101) and (-10-1) spot; scale bars: 1 nm-1 (d),(h) Multi-slice simulated modulation of encircled diffraction spots in (c),(g) with tilting for nanosheets of different thickness (solid lines) and corresponding experimental scatter data (solid circles) confirming that the nanosheets are 1.5 unit cells thick.

The dispersed nanosheets in ethanol can be transferred to the air-water interface by simply adding droplets of the suspension on the surface of water. Ethanol evaporates or dissolves in water, leaving behind the nanosheets which spread on the surface of water. The surface pressure isotherm obtained during a typical LS experiment is shown in **Figure 2-3a**. At large trough areas, the isotherms remained horizontal until, at a certain trough area, a rapid increase in surface pressure was observed due to the onset of interactions between adjacent

particles. When a certain minimum trough area (i.e., maximum surface pressure) was reached, the barriers were expanded, and a decrease in surface pressure was observed, which did not follow the surface pressure vs. area curve obtained during compression. The slower increase and sharper decline of surface pressure during compression and expansion, respectively, may indicate loss of particles to the water subphase and/or irreversible aggregation of the nanosheets. In what follows, we report nanosheet deposits formed on silicon wafers transferred during the first compression. Silicon wafers, as-purchased or with a ~50 nm thermally-grown oxide layer were used as the substrates for nanosheet coatings. **Figures 2-3b to 2-3d** show scanning electron microscopy (SEM) images of the coatings made on thermally oxidized silicon wafers at various surface pressures. Surface coverage by nanosheets increased with increasing surface pressure. Closely packed monolayers were obtained at 20 and 25 mN/m surface pressure while at even higher surface pressures we observed the onset of nanosheet overlapping (**Figure 2-4**).

The thickness of a monolayer coating of nanosheets was confirmed by atomic force microscopy (AFM), as shown in **Figures 2-5a and 2-5b**. The coating imaged by AFM was deposited at 25 mN/m surface pressure on a thermally oxidized silicon wafer (similar to the coating shown in **Figure 2-3d**). Line profiles across three randomly chosen nanosheets are shown in **Figure 2-5b**. The average thickness is measured to be 2.9 ± 0.09 nm. Almost all the nanosheets seen in **Figure 2-5a** have similar contrast, which indicates uniform thickness of the coating. A few overlapped regions are present (seen as bright spots in **Figure 2-5a**) but mostly there is monolayer coverage of nanosheets on the substrate.

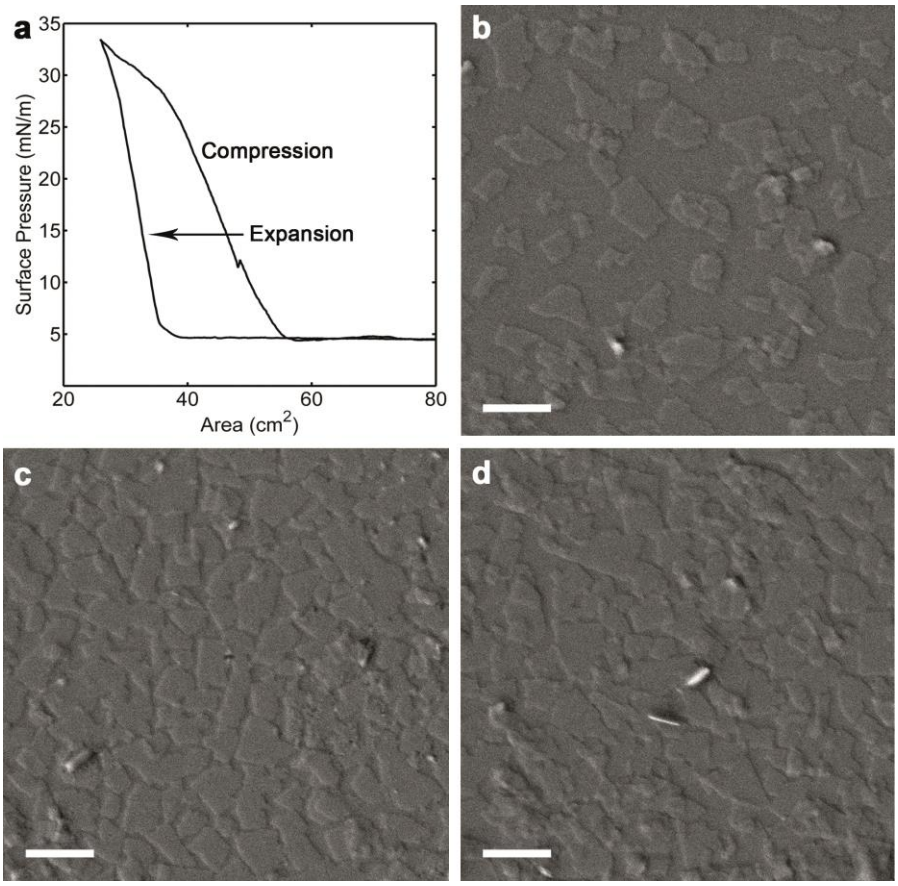

Figure 2-3: (a) Surface pressure isotherm from the first compression-expansion cycle obtained during a typical LS experiment; (b)-(d) Coatings made at 15, 20 and 25 mN/m surface pressure on thermally oxidized silicon substrates showing that packing of nanosheets increases with surface pressure, eventually resulting in overlapped coatings; scale bars: 400 nm.

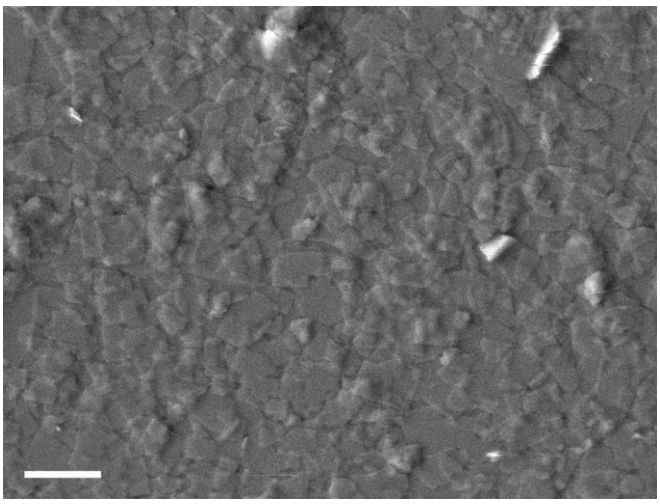

Figure 2-4: SEM image of nanosheet coating on thermally oxidized Si wafer, obtained by LS at 30 mN/m surface pressure. It reveals that considerable overlap of nanosheets occurs at high surface pressure. Bending of some nanosheets is also evident in areas of bright contrast. Scale bar: 400 nm.

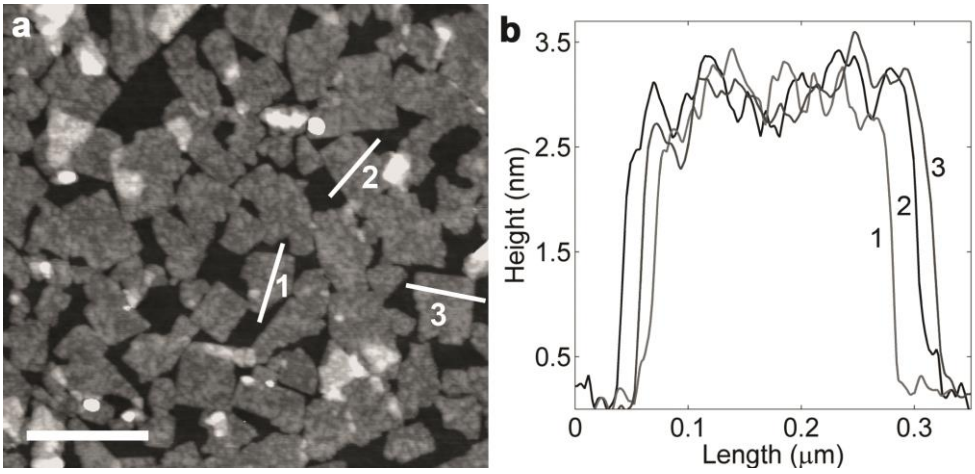

Figure 2-5: (a) AFM image of nanosheets deposited on silicon substrate using LS; scale bar: 500 nm and (b) the corresponding height profiles showing that nanosheets are approximately 3 nm in thickness. Calibration was done using 2.0 nm steps on HF-etched mica, as in Ref. 88.

The surface coverage of nanosheets could be increased by repeating LS several times on the same substrate. As seen in **Figure 2-6c**, some curling was observed after 10 cycles of deposition. However, the films exhibited high coverage on the silicon substrate, compared to the single-layer coating shown in **Figure 2-6a**. Infrared spectroscopy (IR) was used to detect the presence of OSDA (**Figures 2-6b and 2-6d**). As expected, peaks corresponding to the C-H stretching mode of OSDA were observed in the region from 2800-3000 cm^{-1} for as-deposited single-layer and multi-layer films, while no IR signal corresponding to the OSDA was detected after calcination at 500º C.

Multi-layer coatings of nanosheets were analyzed by in-plane X-ray diffraction (in-plane XRD), as seen in **Figures 2-6e and 2-6f**. Such an analysis could not be done for single-layer coatings due to the low signal-to-noise ratio obtained by the in-house diffractometer used. The deposited nanosheets were not intergrown but remained in contact through weak non-covalent bonding interactions (e.g., van der Waals and hydrogen bonding). It was, therefore, expected that they can slide with respect to each other. Indeed, in-plane XRD revealed significant differences in the crystallographic dimensions of the deposited nanosheets before and after calcination, as shown in **Figure 2-6f**. Shifts in the (501) and (303) Bragg peaks indicated in-plane contraction of the lattice. The observed in-plane contraction of the nanosheets is comparable to that expected from bulk silicalite-1 upon OSDA removal (Table 2-1).[15,90]

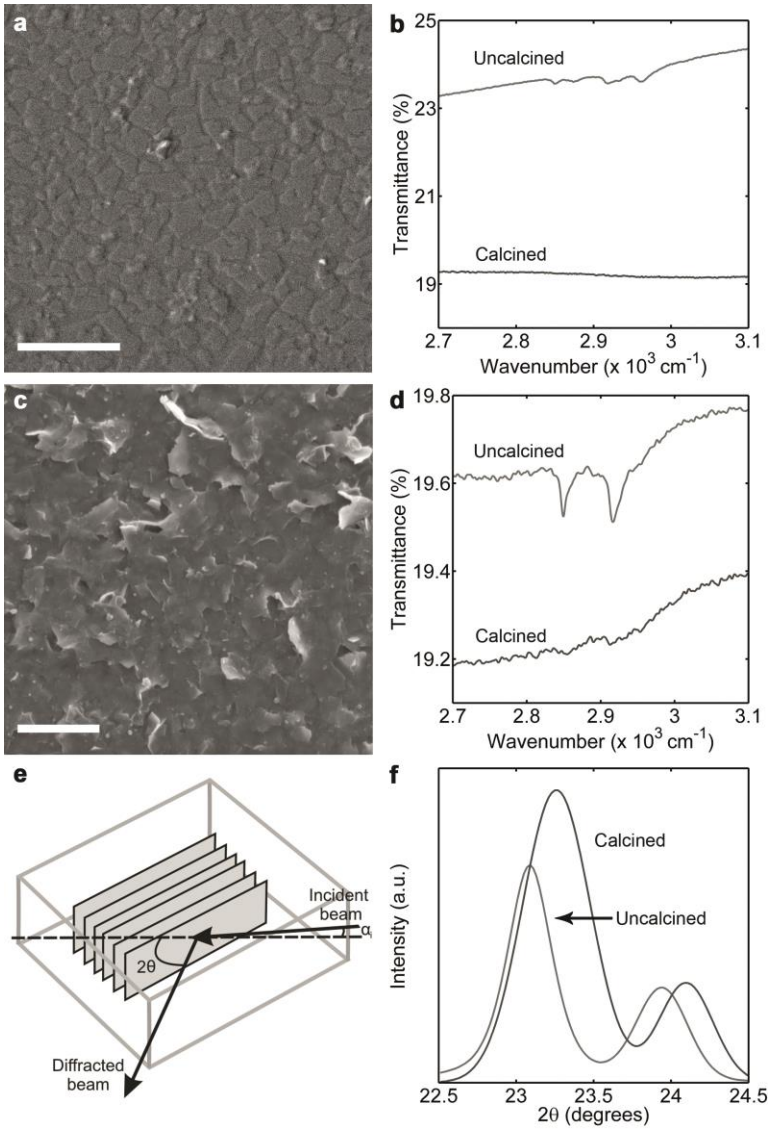

Figure 2-6: (a), (c) Single and multi-layer nanosheet films made by LS; scale bars: 1 μm; (b), (d) FT-IR spectra obtained from nanosheet films similar to those shown in (a) and (c) respectively, showing that the peaks corresponding to OSDA are absent after calcination; (e) Schematic of in-plane X-ray diffraction, where α_i is the angle of incidence and 2θ is the angle between the incident beam and the detector; (f) In-plane X-ray diffraction patterns obtained from a multi-layer nanosheet film showing that there is in-plane contraction of the crystalline framework caused by OSDA removal on calcination.

hkl	Multilayer LS coating		Bulk silicalite-1	
	Uncalcined	Calcined	Uncalcined	Calcined
501	3.85	3.82	3.84	3.80
303	3.71	3.69	3.71	3.68

Table 2-1: (501) and (303) d-spacings (in Å) obtained from X-ray diffraction on multilayer LS coatings of nanosheets (see Figure 2-6f) and from bulk silicalite-1 (from www.iza-online.org).

After calcination, the deposited monolayers were subjected to secondary growth in order to obtain intergrown films. Depending on the secondary growth procedure and conditions, distinct microstructures were obtained. **Figures 2-7a and 2-7b** show SEM images of films after secondary growth, carried out with the nanosheet coating in direct contact with a TPA-silica sol[61,91] (5TEOS:1TPAOH:1000H_2O) and a TEAOH-silica gel[87] (4TEOS:1.92TEAOH:0.36$(NH_4)_2SiF_6$:40H_2O), respectively. In both cases, the substrates used were as-purchased silicon wafers. In the case of secondary growth using the TPA-silica sol, after hydrolysis and pretreatment of the sol at 150º C, the coating was placed in the sol and heated to 90º C in a sealed autoclave. After 5 hours, oriented films were obtained but some twinning was seen, a common occurrence for TPA-silica sol-based secondary growth procedures. Specifically, *a*-oriented twins are visible in **Figure 2-7a** as thin protruding plates on the otherwise *b*-oriented film. For secondary growth using the TEAOH gel method, the solid gel was aged and then mixed by a blender. Nanosheet coating was inserted into the gel and heated to 150º C in a sealed autoclave. The morphology obtained after 6 hours is shown in **Figure 2-7b**. Incomplete intergrowth was observed due to faster in-plane growth along the *c*-axis. Further optimization of the secondary growth conditions in order to obtain thin and *b*-oriented films should be possible.

We also tried the "gel-less" method in which growth of MFI can be induced on a silicon wafer with oxide coating in the presence of TPA^+ ions.[64,92] Here, the silica source is not externally introduced but comes from the substrate. Nanosheet coatings deposited on silicon substrates with a 50 nm thermally-grown oxide (which acts as the silica source) were spin-coated with a very dilute TPAOH solution and heated to a high temperature (220º C) for 72 hours. **Figure 2-7c** shows a top view SEM image of a representative film after gel-less secondary growth. An intergrown zeolite layer was obtained, which remained crack-free upon calcination. **Figure 2-7d** shows in-plane XRD of the same film before and after calcination at 500º C. Unlike the multi-layer as-deposited films of similar thickness (**see Figure 2-6f**), the intergrown MFI films do not exhibit changes in their in-plane crystallographic dimensions. This is probably a result of strong attachment to the support and to the neighboring grains by Si-O-Si bonds. Apparently, these films are under compressive strain but remain crack free.

To determine the thickness of the films after gel-less growth, we prepared cross sections using focused ion beam (FIB) milling. The region containing Si and O was determined to be approximately 50 nm (**Figure 2-8**). This is comparable to the thickness of the SiO_2 thermal oxide layer, which was determined to be 48.8 ± 0.3 nm by ellipsometry. At this time, it was not possible to discriminate what part of this layer is SiO_2 and what part is zeolite, most likely due to amorphization of the zeolite layer by the FIB. Therefore, this technique was inconclusive in determining the exact thickness of the zeolite layer but it indicates that the film cannot be thicker than 50 nm.

To resolve the issue of zeolite film thickness, we used sparse monolayers by depositing them at low pressures (see **Figure 2-3b**). When these layers were grown using gel-less

secondary growth conditions identical to those of **Figure 2-7c**, they do not cover the entire substrate allowing one to measure the thickness of the intergrown regions by reference to the nearby exposed substrate surface. From these measurements we determine the thickness to be less than 12 nm (**Figure 2-9**).

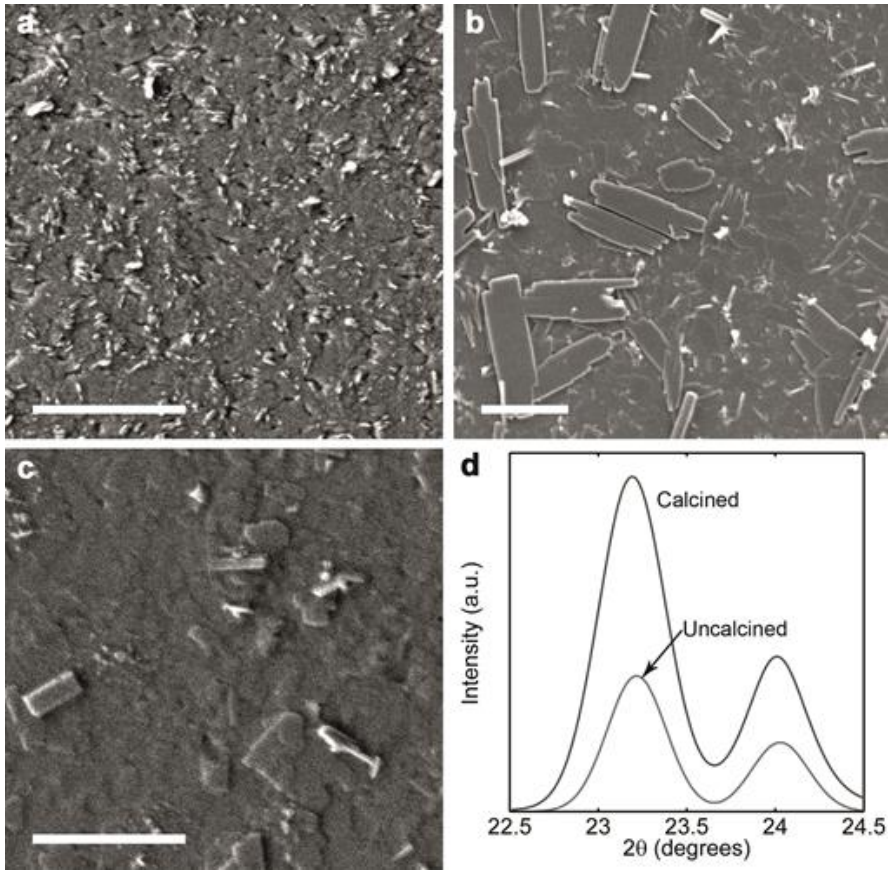

Figure 2-7: Secondary growth of single-layer nanosheet films using: (a) TPA-silica sol, (b) TEAOH silica gel and (c) gel-less growth using TPAOH; scale bars: 1μm. (d) In-plane X-ray diffraction before and after calcination at 500º C obtained from the film shown in (c), indicating that there is no detectable in-plane crystallographic change caused by calcination.

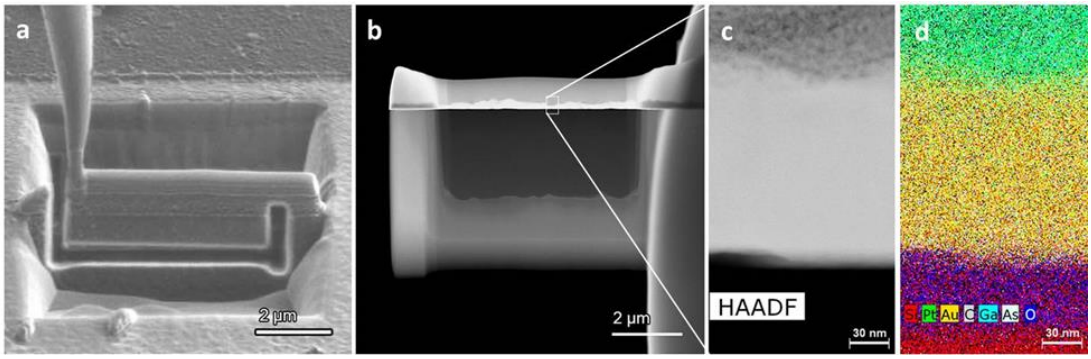

Figure 2-8: (a) Ion beam image showing a platinum and gold coated film before thinning by a focused ion beam. (b) HAADF-STEM image of a ~70 nm thin section shown in (a). Heavier atomic number (Z) elements appear brighter in the STEM image. (c) HAADF-STEM image of a 150 nm x 250 nm section from (b). (d) Spatially resolved STEM EDX composite map showing the distribution of elements in the section shown in (c). The thickness of the SiO_2 + MFI layer is ~50 nm.

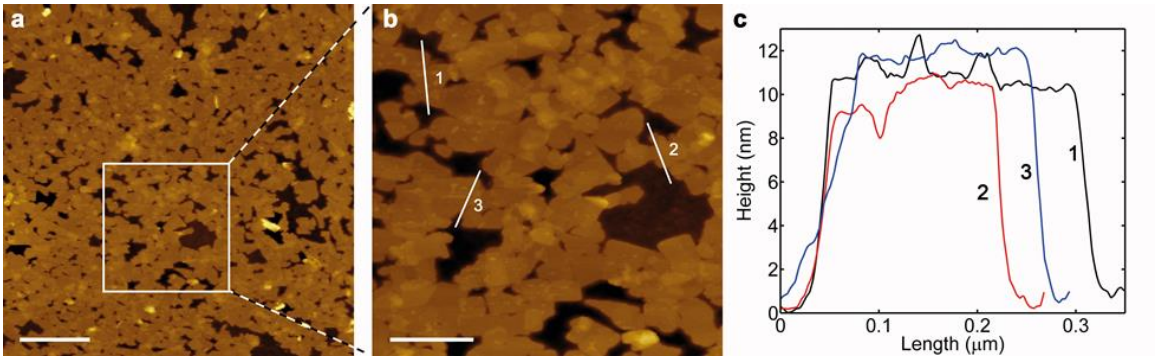

Figure 2-9: (a) Low magnification AFM image of gel-less secondary grown film. The initial seed layer was sparse resulting in gaps where substrate is visible. Scale bar: 1 µm. (b) Magnified image of area shown in (a); scale bar: 400 nm. (c) Height profiles corresponding to the lines in (b) show that the film thickness does not exceed 12 nm.

2.5 Conclusions

In summary, we report here that acid treatment of MFI nanosheets facilitated partial removal of the OSDA without altering their MFI crystal structure and thickness. This allowed for nanosheets to be dispersed in ethanol and subsequently transferred to the air-water interface. Using the Langmuir Schaefer deposition technique, nanosheets could be transferred to solid substrates to form monolayer coatings ranging from sparse to close-packed. Successive depositions resulted in oriented multi-layer films with control over their thickness, while secondary growth of monolayers yielded intergrown, oriented films with sub-12 nm thickness. This unprecedented control over thickness and orientation uniformity of zeolite films may open new opportunities for investigating adsorption, transport, dielectric and mechanical properties of zeolites.

Chapter 3: Nanoscale Control of Homoepitaxial Growth on a 2-Dimensional Zeolite

Parts of this chapter are published as:

M. Shete, M. Kumar, D. Kim, N. Rangnekar, D. Xu, B. Topuz, K.V. Agarwal, E. Karapetrova, B. Stottrup, S. Al-Thabaiti, S. Basahel, K. Narasimharao, J. D. Rimer and M. Tsapatsis., *Angew. Chem Int. Ed.* 56, 535-539 (2017).

3.1 Chapter Overview

Nanoscale crystal growth control is crucial for tailoring 2-dimensional (2D) zeolites (crystallites with thickness less than two unit cells) and thicker zeolite nanosheets for applications in separation membranes and as hierarchical catalysts. However, methods to control zeolite crystal growth with nanometer precision are still in their infancy. Here, we report solution-based growth conditions leading to anisotropic epitaxial growth of 2D zeolites with rates as low as few nanometers per day. Contributions from misoriented surface nucleation and rotational intergrowths are eliminated. Growth monitoring at the single-unit-cell level reveals novel nanoscale crystal growth phenomena associated with the lateral size and surface curvature of 2D zeolites.

3.2 Introduction

Zeolites, crystalline microporous materials with pores of molecular dimensions, are currently used as catalysts,[14] adsorbents and separation membranes,[93–96] while being considered for new applications.[74,97] Their performance depends mainly on their pore structure, but also on precise control of their crystal shape and size.[25,47,98,99] Recent advances in the synthesis of core-shell zeolite catalysts,[51] 2-dimensional (2D) and

hierarchical zeolites,[48–50] exfoliated zeolite nanosheets,[26,60] and thin zeolite films,[27,64] suggest that nanometer level control of zeolite crystal growth is desirable. However, studies of zeolite crystallization are limited to conventional crystals[100,101] and nanoscale growth events have not been resolved. Here, growth of a 2D zeolite with nanometer resolution is presented. Conditions leading to slow and controllable growth of 3nm-thick 2D-MFI nanosheets (for description of MFI structure, see http://www.iza-online.org) with rates of few nanometers per day are identified and provide unprecedented control towards the design of thin films and hierarchical catalysts. Anisotropic growth in the absence of misoriented domains is achieved and allows observation of new crystal growth phenomena associated with the size and local curvature of zeolite nanosheets.

3.3 Experimental

3.3.1 Synthesis and exfoliation of multilamellar silicalite-1

Multilamellar silicalite-1 (ML-MFI) was synthesized following the procedure reported in the literature.[26,49,60] First, the bromide form of the di-quaternary ammonium structure directing agent ($C_{22}H_{45}$-N^+ $(CH_3)_2$-C_6H_{12}-N^+ $(CH_3)_2$-C_6H_{13} $(2Br^-)$) or $C_{22\text{-}6\text{-}6}Br_2$ was synthesized following the alkylation reaction of *N, N, N', N'*-tetramethyl-1,6,-diaminohexane with 1-bromodocosane followed by alkylation of the product with 1-bromohexane. Hydroxide form of the SDA ($C_{22\text{-}6\text{-}6}(OH)_2$) was obtained by ion-exchange of the bromide form using silver (II) oxide (predominantly silver (II) oxide, Sigma Aldrich). For the synthesis of ML-MFI, tetraethylorthosilicate (98 %, Sigma Aldrich) was hydrolyzed in the aqueous solution of $C_{22\text{-}6\text{-}6}(OH)_2$ for a day, to obtain a gel with composition 100 SiO_2: 15 $C_{22\text{-}6\text{-}6}(OH)_2$: 4000 H_2O. The gel was then transferred into Teflon-lined stainless steel autoclaves and set for hydrothermal synthesis under rotation at

150° C for 8 days. The product obtained was washed and dried. Exfoliation was performed using polymer-melt compounding[26]. A mixture of ML-MFI (0.6 g) and polystyrene (14.4 g; Piccolastic A75 hydrocarbon resin, M_w 1300 g/mol) was fed to a twin screw extruder (DSM Xplore micro compounder) and allowed to mix sequentially at 120° C for 15 min, 95° C for 15 min and 75° C for 45 min and then extruded at 80° C to obtain the polymer-zeolite nanocomposite containing exfoliated 2D-MFI nanosheets.

3.3.2 Preparation of ethanol suspensions of 2D-MFI nanosheets

To remove the polymer and non-exfoliated zeolite material, the polymer-zeolite nanocomposite was treated following the density-gradient centrifugation procedure reported earlier.[60] The resultant exfoliated 2D-MFI nanosheets suspension in octanol was centrifuged (Beckman Coulter, Model: Avanti J-20 XP equipped with JA25.50 rotor) at 40,000 g for 3 h at 4° C to obtain a cake. The cake was solvent exchanged with ethanol (200 proof, anhydrous >99.5 % pure, Sigma Aldrich) by centrifuging it 3 times, each time discarding the supernatant ethanol and adding fresh ethanol. An acid treatment procedure adapted from an earlier work[102] and reported in detail in section 2.3.2 was used for partial detemplation of exfoliated 2D-MFI nanosheets to obtain a stable suspension in ethanol. Accordingly, after the final wash with ethanol, the cake was dispersed in 16 g filtered ethanol (filtered using 0.2µm GHP Acrodisc syringe filter, Pall Corporation). To this, 0.196 g of 98 % sulphuric acid (EMD chemicals) was added and the mixture, sealed in a glass reaction vial, was heated at 80° C for 16 h in an oil bath. After reaction the mixture was centrifuged at 40,000 g for 3 h and the supernatant discarded to remove unreacted sulphuric acid. The cake obtained was redispersed in 8 g ethanol. To this, 6.2 g of filtered heptane (anhydrous 99 %, Sigma Aldrich; filtered using 0.2µm PTFE syringe filter, Pall

Corporation) and 0.12 g of hydrochloric acid (37 %, Sigma Aldrich) were added and the mixture, sealed in a glass reaction vial, was heated at 90° C for 16 h in an oil bath. 2D-MFI nanosheets were then recovered by centrifugation at 40,000 g for 3 h. The 2D-MFI nanosheet cake was washed with ethanol 2-3 times to remove traces of heptane and remaining hydrochloric acid. To the washed acid-treated cake, 40 g of filtered ethanol was added and the cake was dispersed by vortexing (Fisher Scientific vortex mixer) for 15 min followed by bath sonication (Branson 5510R-DTH ultrasonic cleaner) for 15 min to obtain a suspension in ethanol. The suspension quality was confirmed by Transmission electron Microscopy (TEM) imaging as reported.[102]

3.3.3 Preparation of Si wafer substrates

Silicon wafers (CZ silicon, p type) with a <1 0 0> orientation from Silicon Quest International were used as the substrate. Typically, 4 inch Si wafers were cut into 1 cm x 1 cm square pieces using a wafer saw (Disco DAD 2H/6T) equipped with a diamond blade (Disco NBC-ZH2030-SE). An indent was made at the center of the 1cm x 1cm square piece using a diamond indenter with a load of 980.7 mN on the Buehler Micromet 2100 series microhardness tester. The indent was made to act as a marker to identify the same region of nanosheets before and after growth. After indentation, the 1cm x 1cm Si wafer substrates were sonicated (Branson 5510R-DTH ultrasonic cleaner) in distilled water for about 20 min to remove any metallic dust that could have been attached on the surface during the saw cutting and indenting process. After sonication, the substrates were immersed in a piranha solution bath (3:1 v/v mixture of sulphuric acid to hydrogen peroxide) maintained at 120° C for about 1 h. After cleaning in piranha solution, the substrates were washed with copious amounts of distilled water. They were then placed in an oven set at 70° C to dry

off the water on the surface. The dried wafers were plasma treated (PDC – 326, Harrick Plasma) using air plasma for about 1 min before being used for coating.

3.3.4 Deposition of 2D-MFI nanosheets on Si wafers using Langmuir-Blodgett deposition

A KSV-Nima Liquid-Liquid trough with an IU4 interface having a maximum area of 120 cm^2 and a minimum area of 23 cm^2 was used. The trough was rinsed thoroughly with distilled water before each coating. Millipore water (18.2 MΩ.cm) was used as the subphase. Typically, around 1.5 ml of the MFI nanosheets suspension in ethanol was dispersed at the air-water interface in the Langmuir trough (with the barriers fully open) using a micropipette. The interface was allowed to equilibrate for around 30 min before starting the coating experiment. Typical equilibrium surface pressures of around 2-3 mN/m were observed. The interface was then compressed by bringing the barriers close together at a speed of 30 cm^2/min. Surface pressure changes were recorded in the surface pressure vs. area isotherm. Surface pressures in the range of 15-20 mN/m were desired for transferring the 2D-MFI nanosheets at the air-water interface to the Si wafers using the Langmuir Blodgett (LB) vertical deposition. A 1 cm x 1 cm Si wafer substrate, cleaned as mentioned before, was held vertically at the corner using the Nima LB dipping mechanism. As the desired surface pressure was reached, the Si wafer substrate was lowered to the interface at a speed of 2 cm/min. Once the wafer was completely submerged in the subphase, it was lifted up at a speed of 1 cm/min thus transferring the 2D-MFI nanosheets onto it. The coating obtained was allowed to air dry before calcining it at 500° C for 6 h under air flow rate of 150 ml/min. Temperature ramp rates were 1° C/min during the ramp up and ramp down steps of calcination.

3.3.5 Chemicals used in the solution-based growth of 2D zeolites

Tetraethylorthosilicate (TEOS, 98 %, Sigma Aldrich), tetrapropylammonium hydroxide (TPAOH, 1M solution, Sigma Aldrich), tetraethylammonium hydroxide (TEAOH, 35 % w/w solution, Alfa Aesar).

3.3.6 *In situ* atomic force microscopy (AFM) growth experiments

The TPAOH-based growth sol for *in situ* AFM experiments was prepared by hydrolyzing TEOS in an aqueous solution of TPAOH to form a sol of molar composition 0.2 TPAOH: 1TEOS: 200H_2O. Typically, to obtain a 30 g growth sol, 1.58 g of 1M TPAOH solution and 1.63 g of TEOS were added sequentially to 26.79 g of distilled water and hydrolyzed for around 24 h. After hydrolysis, the sol was filtered using a 0.2 µm GHP filter (Pall Corporation) and transferred to Teflon-lined stainless steel autoclaves. It was then pretreated in a convection oven set at 150° C for 2 h. After pretreatment, the sol turned cloudy and was filtered twice using a 0.2 µm GHP filter to obtain an optically clear growth sol which was used for *in situ* AFM studies. The TEAOH-based growth sol for *in situ* AFM experiments was prepared by hydrolyzing TEOS in an aqueous solution of TEAOH and TPAOH to form a sol of molar composition 0.198 TEAOH: 0.002TPAOH: 1TEOS: 100H_2O. Typically, to obtain a 30 g growth sol, 1.23 g of TEAOH solution, 0.03 g of 1M TPAOH and 3.07 g of TEOS were added sequentially to 25.68 g of distilled water and hydrolyzed for around 24 h. After hydrolysis, the sol was filtered and pretreated at 150° C for 2 h. After pretreatment, the sol remained optically clear and therefore was not filtered. *In situ* AFM measurements were performed on an Asylum Research MFP-3D-SA instrument[103] (Santa Barbara, CA) equipped with a custom-designed liquid sample cell for imaging in solvothermal conditions (for details of the cell design and specifications, refer

to 5). A silicon wafer coated with *b*-oriented 2D-MFI nanosheets was firmly placed on a 15-mm specimen disk (Ted Pella, Inc.) using quickset Loctite epoxy that was cured in an oven at 60° C for 1 h. The sample was cooled in air, gently rinsed with DI water, and dried under Argon gas to remove any dust. The sample was placed within a closed AFM liquid cell (volume ≈ 3 ml). AFM images were collected using a silicon nitride cantilever coated with Cr/Au with spring constant 0.82 N/m (Olympus RC800PB). The 2D-MFI nanosheet coated silicon wafer surface was first scanned in air to locate a desired imaging area. The growth sol was then introduced into the AFM cell by syringe and the sample was left to equilibrate in contact with the sol at room temperature for ca. 30 min. The temperature was then ramped to a set point at a rate of 1° C/ min. Growth sol was continuously supplied to the liquid cell using a syringe pump (Razel Scientific Instruments, Model R100-E) at the rate of 0.4 cc/h. Once the sample cell reached the set point temperature, the liquid flow rate was reduced to 0.2 cc/h and the sample cell was allowed to equilibrate for 1 h before continuous imaging. AFM images were collected in both contact and tapping modes at a scan rate of 1.5 Hz and 256 lines/scan. Multiple regions of the sample and different scanning area sizes were compared to confirm the absence of tip artifacts.

3.3.7 *Ex situ* growth experiments in the TPAOH-based clear sols

TEOS was hydrolyzed in an aqueous solution of TPAOH for ~24 h to obtain a growth sol with a molar composition of 0.2 TPAOH: 1TEOS: 200 H_2O. Typically, to obtain a 30 g growth sol, 1.58 g of 1M TPAOH solution and 1.63 g of TEOS were added sequentially to 26.79 g of distilled water and hydrolyzed for around 24 h. After hydrolysis, the sol was filtered using a 0.2 µm GHP filter (Pall Corporation) and transferred to Teflon-lined stainless steel autoclaves. It was then pretreated in a convection oven set at 150° C for 2 h.

After pretreatment, the sol turned cloudy and was filtered twice using a 0.2 µm GHP filter to obtain an optically clear growth sol which was transferred to Teflon-lined autoclaves. A calcined coating of 2D-MFI nanosheets on Si wafer was held vertically using a Teflon holder and placed in the growth solution. Growth was carried out at 90° C for 5 h and at 60° C for 24 h. After growth, the coating was removed and washed with distilled water and air dried before AFM analysis.

3.3.8 Prolonged intergrowth in the TPAOH-based clear sols leading to *a*-&*b*-oriented films

TEOS was hydrolyzed in an aqueous solution of TPAOH for ~8 h to obtain a growth sol with a molar composition of 0.15 TPAOH: 1TEOS: 135 H_2O. Typically, to obtain a 30 g growth sol, 1.75 g of 1M TPAOH solution and 2.34 g of TEOS were added sequentially to 25.97 g of distilled water and hydrolyzed for ~8 h. After hydrolysis, the sol was filtered using a 0.2 µm GHP filter (Pall Corporation) and transferred to Teflon-lined stainless steel autoclaves. The sol was then pretreated in a convection oven set at 90° C for 40 h. After pretreatment, it was filtered twice using a 0.2 µm GHP filter and transferred to Teflon-lined autoclaves. A calcined coating of 2D-MFI nanosheets on Si wafer was held vertically using a Teflon holder and placed in the growth sol. Growth was carried out at 90° C for 24 h. After growth, the coating was removed and washed with distilled water and air dried before SEM analysis.

3.3.9 *Ex situ* growth in TEAOH-based clear sols

TEOS was hydrolyzed in an aqueous solution of tetraethylammonium hydroxide TEAOH for 24 h to obtain a growth sol with a molar composition of 0.2 TEAOH: 1TEOS: 100 H_2O.

Typically, to obtain a 30 g growth sol, 1.24 g of TEAOH solution and 3.07 g of TEOS were added sequentially to 25.69 g of distilled water and hydrolyzed for 24 h. After hydrolysis, the solution was filtered using a 0.2 μm GHP filter (Pall Corporation) and transferred to Teflon-lined stainless steel autoclaves. It was then pretreated in a convection oven set at 150°C for 2 h. After pretreatment, the sol remained optically clear and no filtration was done. A calcined coating of 2D-MFI nanosheets on Si wafer was held vertically using a Teflon holder and placed in the growth sol. Growth was carried out at 110° C and 130° C for 3 days. After growth, the coating was removed and washed with distilled water and air dried before AFM analysis. In order to fill most of the interparticle voids and to obtain a well-intergrown film, multiple growth steps were required. Multiple growth steps were performed under conditions similar to the first growth, calcining the film after each growth step at 500° C for 6 h under airflow of 150 ml/min.

3.3.10 TEAOH-based growth of self-pillared pentasil (SPP)

All silica SPP was synthesized as reported in literature.[48] For TEAOH-based growth, a sol with molar composition of 0.2TEAOH: 1TEOS: 100H_2O was prepared by hydrolysis of TEOS in an aqueous solution of TEAOH for 24 h. After hydrolysis, the solution was filtered using a 0.2 μm GHP filter (Pall Corporation) and transferred to Teflon-lined stainless steel autoclaves. It was then pretreated in a convection oven set at 150° C for 2 h. After pretreatment, the sol remained optically clear and no filtration was done. 50 mg of calcined SPP was introduced into the pretreated growth sol. Growth was carried out at 110° C for 17 h. After growth, the SPP particles were collected by centrifugation and washed with distilled water to lower the pH to around 8. A suspension of SPP in water after TEAOH-growth was used for TEM analysis. Calcined SPP before TEAOH-growth was

dispersed in ethanol before TEM analysis. TEM samples were deposited on a lacey carbon film on a 400 mesh copper grid.

3.3.11 Characterization methods

3.3.11.1 Ex situ atomic force microscopy

A Bruker Nanoscope V Multimode Scanning Probe Microscope was used in tapping mode in the repulsive regime for collecting AFM images. A silicon nitride tip was used and AFM images were collected at a scan rate of 0.8 Hz and 512 lines/scan.

Calcined, Si wafer supported 2D-MFI nanosheets were imaged before growth. The indent on the Si wafer was located at first in the optical microscope attached to the AFM and the tip was positioned near the indent. Regions on the coating close to the indent were imaged. After growth, the same region on the film that was imaged before growth was located with the help of the indent and imaged.

For analysis of AFM images, Gwyddion 2.4 software was used. The lateral dimensions of MFI nanosheets before and after growth were measured along the edges using the "measure distance" functionality in Gwyddion. The direction of maximum lateral growth was assigned as the *c*-axis (as it is known that TEAOH-based sols favor growth along the *c*-axis[87]). The direction perpendicular to it was thus assigned as the *a*-axis. Measurements were made on several different nanosheets and average values for growth along the *c*- and *a*- axes were determined. The AFM height data were calibrated using the 2 nm and 1 nm steps etched on muscovite mica.[88] Data reported in Fig. 3-6 d, f is from flat-large, non-fragmented, non-overlapping nanosheets.

3.3.11.2 Scanning electron microscopy (SEM)

A JEOL 6700 scanning electron microscope equipped with a field emission gun and operating at 1.5 kV was used for SEM analysis.

3.3.11.3 Out-of-plane X-ray diffraction (XRD)

Out-of-plane XRD data were collected using Panalytical X'Pert Pro diffractometer. A Ge 4-bounce hybrid prefix module with a 1/2° divergence slit was used as the incident beam optics while the diffracted beam side consisted of a triple axis – rocking curve optics with a 1/2° receiving slit. Out-of-plane scans were run in the 2θ (Cu- Kα) range from 5-50 degrees with a step size of 0.02° and a dwell time of 5 seconds. The data obtained were processed using the MDI-JADE 2.6.5 software. Profile fitting was undertaken using skewness of the peaks as a fixed variable to fit profiles and to subtract a linear background and strip Kα2. The fitted profile data so obtained were plotted and used to determine the exact peak positions and to index the peaks.

3.3.11.4 In-plane X-ray diffraction

In-plane XRD data were collected at the synchrotron beam line 33-BM-C at the Advanced Photon Source, Argonne National Laboratory. The beam line X-ray source of 15 keV (corresponding to a wavelength of 0.827Å) was used to scan a 2θ range of 3-30 degrees with a step size of 0.01°, collecting in total 2720 points. Helium atmosphere was maintained around the sample to minimize loss in intensity due to air scattering. A collimator tube with slits of dimensions 1000 μm × 1000 μm was used on the detector side. X-ray data obtained were converted to Cu- Kα wavelength and processed using the MDI-JADE 2.6.5 software. A linear background was subtracted and profile fitting was undertaken using skewness of the peaks as a fixed variable to fit profiles. The fitted profile

data so obtained were plotted and used to determine the exact peak positions and to index the peaks.

3.3.11.5 Transmission electron microscopy (TEM)

A FEI-Tecnai T12 TEM with LaB_6 filament gun operating at 120 kV and equipped with a Gatan MSC794 CCD camera was used for TEM analysis.

3.4 Results

3nm-thick 2D-MFI nanosheets (thickness of 1.5 unit cell along their *b*-axis) were prepared according to previously reported exfoliation and purification procedures[26,60] and deposited on Si wafers using a Langmuir-Blodgett trough[102] (As discussed in sections 3.3.1-3.3.4). They were then calcined in air at 500° C to remove the occluded structure directing agent (SDA, $C_{22}H_{45}$-$N^+(CH_3)_2$-C_6H_{12}-$N^+(CH_3)_2$-C_6H_{13}.($2OH^-$)). Nanosheet structural integrity after calcination and their expected *b*-out-of-plane preferred orientation upon deposition on Si wafers were confirmed as reported earlier.[102] It was then attempted to grow these SDA-free Si-supported nanosheets wider, eventually causing them to laterally intergrow, while minimizing increase in thickness and non-oriented growth (due to rotational and random intergrowths). First, typical MFI growth sols based on tetrapropylammonium hydroxide (TPAOH) were investigated. However, MFI growth with TPAOH as the SDA is prone to a commonly observed orthogonal rotational intergrowth (twinning) causing loss of preferred crystallographic (and pore) orientation. Within 25 min after reaching the growth temperature, the surfaces of MFI nanosheets start to roughen (**Figure 3-1a**), indicating growth by attachment of precursor silica nanoparticles known to be present in these sols.[91,104] The nanosheets progressively thicken and at 4 h, surface roughness increases and the characteristic morphology of overgrown twins is noticeable (**Figure 3-**

1b). Even though oriented films using TPAOH-based sols have been reported in certain cases for conventional MFI crystals,[61–63] it was not possible to find robust conditions transferrable to 2D-MFI nanosheets.

To avoid loss of orientation, the strategy to manipulate crystal growth rates by altering the SDA[105–107] was adopted. Instead of using TPAOH-based SDA designs, tetraethylammonium hydroxide (TEAOH), known to delay MFI nucleation[108] was selected in an attempt to favor growth by homoepitaxy. Indeed, *in situ* atomic force microscopy (AFM) monitoring of 2D-MFI nanosheet growth with a sol of composition 0.198TEAOH: 0.002TPAOH: 1TEOS: 100H_2O showed extension of the in-plane and out-of-plane dimensions without surface roughening. Representative images obtained at different times are shown in **Figure 3-1c** (2 h) and **Figure 3-1d** (20 h). Differences in nanosheet morphology evolution in TPAOH- and TEAOH-based sols are striking. *In situ* AFM indicates surface roughening for TPAOH-based sols, consistent with a contribution to crystal growth by attachment of precursor nanoparticles.[91] However, despite the presence of nanoparticles in optically clear sols of all tetraalkylammonium cations,[104] roughening was not observed for TEAOH-based sol growth. In light of these observations, we hypothesize that TEAOH steers growth predominantly towards a classical pathway via addition of soluble silica species even in the presence of silica nanoparticles that mostly serve as spectators. In-plane growth rate of 4 nm/h (**Figure 3-1e**) was observed for TEAOH-based sols, while the corresponding out-of-plane growth rate was 0.1 nm/h (**Figure 3-1f**). This slow growth, likely dominated by molecular species, enables unprecedented control of zeolite crystallization and is worth exploring further.

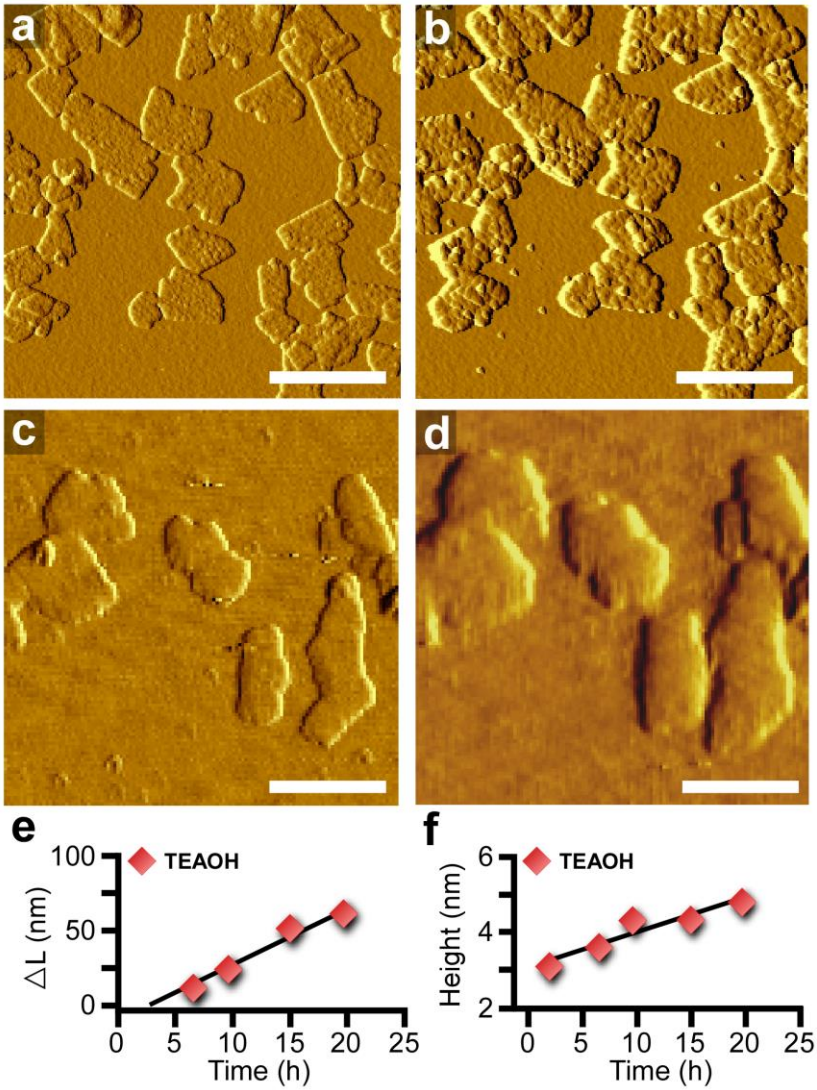

Figure 3-1: *In situ* AFM measurements during growth of Si-supported MFI nanosheets. (a), (b) Amplitude mode images obtained by continuous imaging of MFI nanosheets grown in a TPAOH-based clear sol for (a) 0.4 h and (b) 4.0 h at 70° C. (c), (d) Deflection mode images during continuous imaging of MFI nanosheets grown in a TEAOH-based clear sol of composition 0.198TEAOH: 0.002TPAOH: 1TEOS: 100H_2O for (c) 2.0 h and (d) 20 h at 60° C. (e) Lateral dimension evolution of MFI nanosheets in the TEAOH-based clear sol. (f) Height evolution of MFI nanosheets grown in the TEAOH-based clear sol. (Scale bars: 500 nm)

However, the instrumentation used for in situ AFM observations[103] poses limits on the temperature and duration of growth. In order to access more pronounced nanosheet growth and to completely eliminate the use of TPAOH, we investigated the effect of higher temperatures and longer times in TEAOH-based sols by *ex situ* AFM.

Similar to *in situ* AFM studies, a deposit consisting of 2D-MFI nanosheets was formed on Si wafer (**Figure 3-2a**). The same region of 2D-MFI deposit was imaged after growth with a sol of composition 0.2TEAOH: 1TEOS: 100H_2O for 3 days (**Figure 3-2b**). Nanosheet thickening, extension of the in-plane dimensions of nanosheets, and lateral intergrowth were evident. The sample shown in **Figure 3-2b**, was then subjected to a second 3-day growth (**Figure 3-2c**). Tracking the same region after two 3-day growths revealed further merging of nanosheets (**Figures 3-3 and 3-4**). A highly laterally intergrown and thin MFI film was fabricated after four 3-day growths (**Figure 3-2d**). Only (0 *k* 0) peaks were detected in the out-of-plane X-ray diffraction (XRD) pattern (**Figure 3-2e**) from the film shown in **Figure 3-2d**, confirming that TEAOH-grown films are *b*-oriented, in contrast to the *a*-&*b*- oriented films using TPAOH-based sols (**Figure 3-5**). Consistently, grazing incidence in-plane XRD measurements from uncalcined and calcined coatings and TEAOH-grown films (**Figure 3-2f**) show only the (*h* 0 *l*) peaks. Although in-plane Bragg peaks for the coatings of 2D-MFI nanosheets shift upon calcination (indicating a contraction of the in-plane crystallographic dimensions), peak positions for the TEAOH-grown films exhibit no shift upon calcination due to strong attachment to other nanosheets and the support.[102]

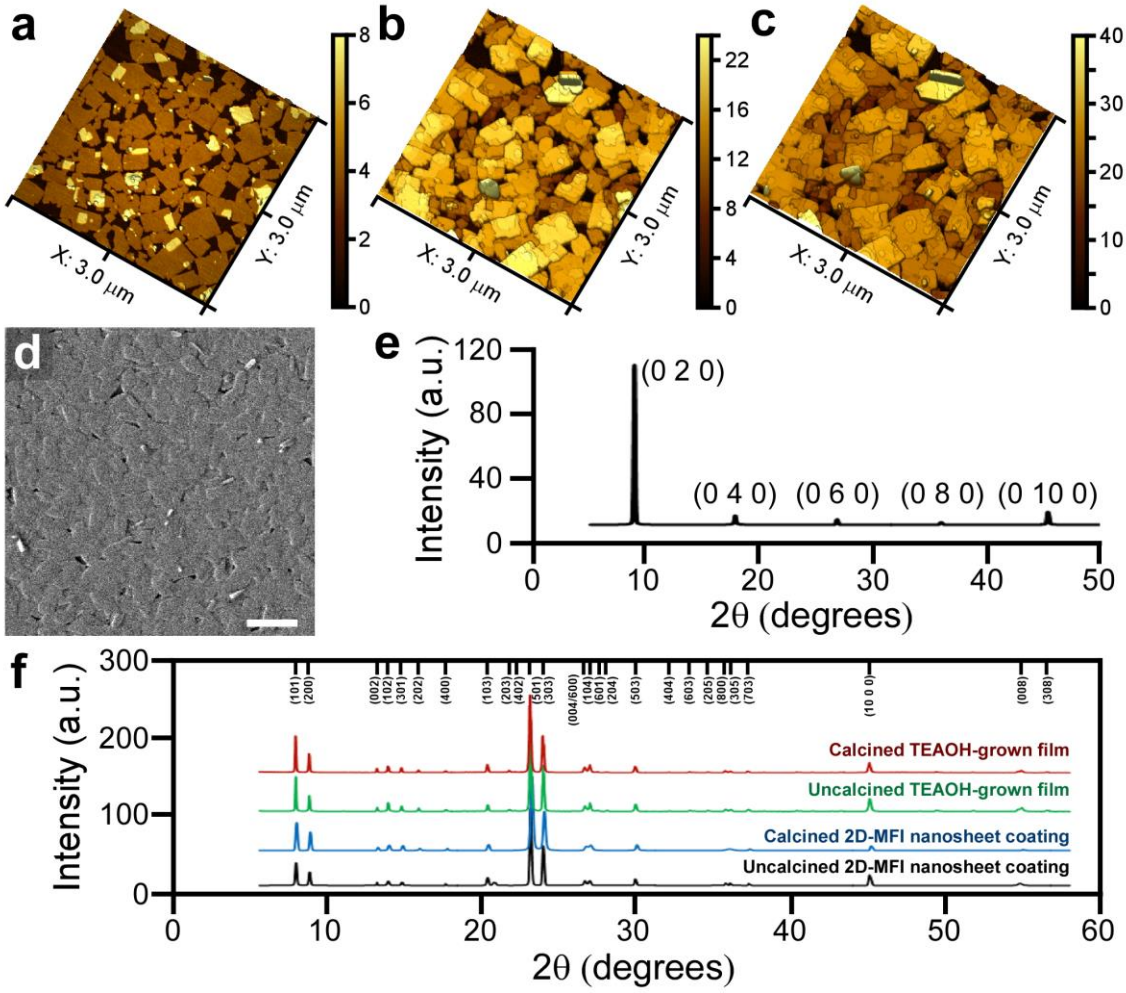

Figure 3-2: Growth of 2D-MFI nanosheets in TEAOH-based sols. (a) AFM 3D height image of 2D-MFI nanosheets supported on Si wafer. (b) AFM 3D height image of the same region as in (a) after the first 3-day growth in a TEAOH-based clear sol of molar composition 0.2TEAOH: 1TEOS: 100H_2O at 110° C. (c) AFM 3D height image of the same region as in (a, b) after the second 3-day growth at same conditions (Height scale: nm). (d) SEM image of a TEAOH-grown MFI film on Si wafer fabricated after four 3-day growths at 110° C. (Scale bar: 1 micron). (e) Out-of-plane XRD pattern from the film in (d); only (0 *k* 0) peaks are detected confirming that TEAOH-grown films are *b*-oriented. (f) Grazing incidence in-plane XRD patterns from calcined and uncalcined 2D-MFI nanosheet coatings and TEAOH-grown films; only (*h* 0 *l*)

peaks are detected confirming the *b*-out-of-plane orientation of nanosheet coatings and TEAOH-grown films.

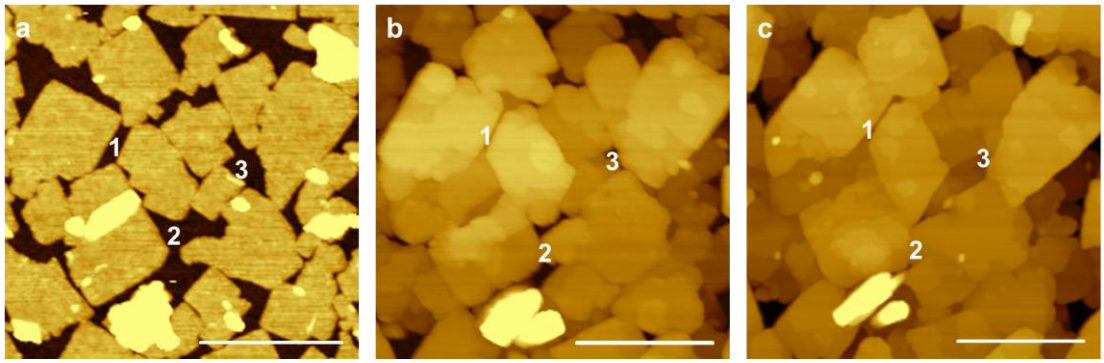

Figure 3-3: (a) AFM height image of 2D MFI nanosheets supported on Si wafer, showing certain interparticle void regions marked "1", "2" and "3". (b) AFM height image of the region in (a) after first 3-day growth depicting the gradual merging (lateral intergrowth) of nanosheets to partially seal the interparticle voids ("1", "2" and "3"). (c) AFM height image of the region in (a, b) after second 3-day growth showing merging of nanosheets to completely seal the interparticle voids ("1", "2" and "3"). A sol with molar composition of 0.2TEAOH: 1TEOS: 100H_2O was used for both 3-day growths at 110° C. (Scale bars: 500 nm)

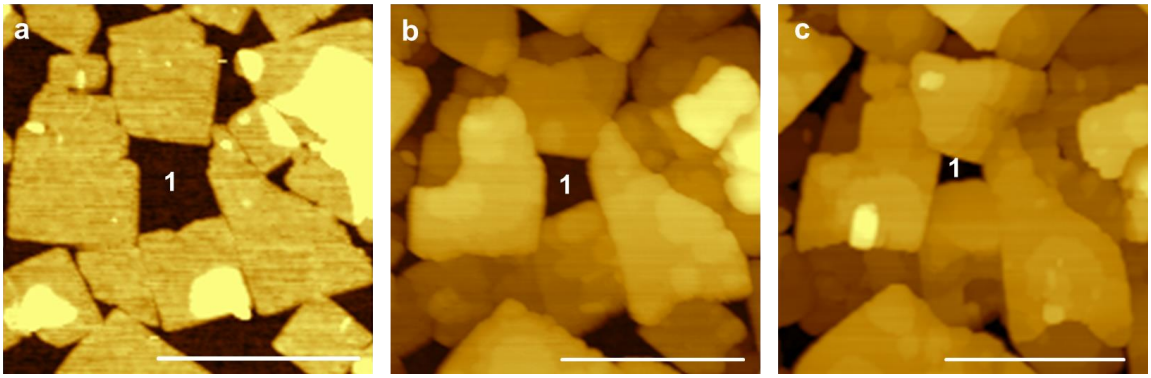

Figure 3-4: (a) AFM height image of 2D-MFI nanosheets supported on Si wafer, forming an interparticle void region "1". (b) AFM height image of the region in (a) after first 3-day growth depicting the gradual merging of nanosheets to partially seal the interparticle void "1". (c) AFM height image of the region in (a, b) after second 3-day growth showing a pinhole remaining due to incomplete merging of nanosheets. Growth conditions as described in Figure 3-3. (Scale bars: 500 nm)

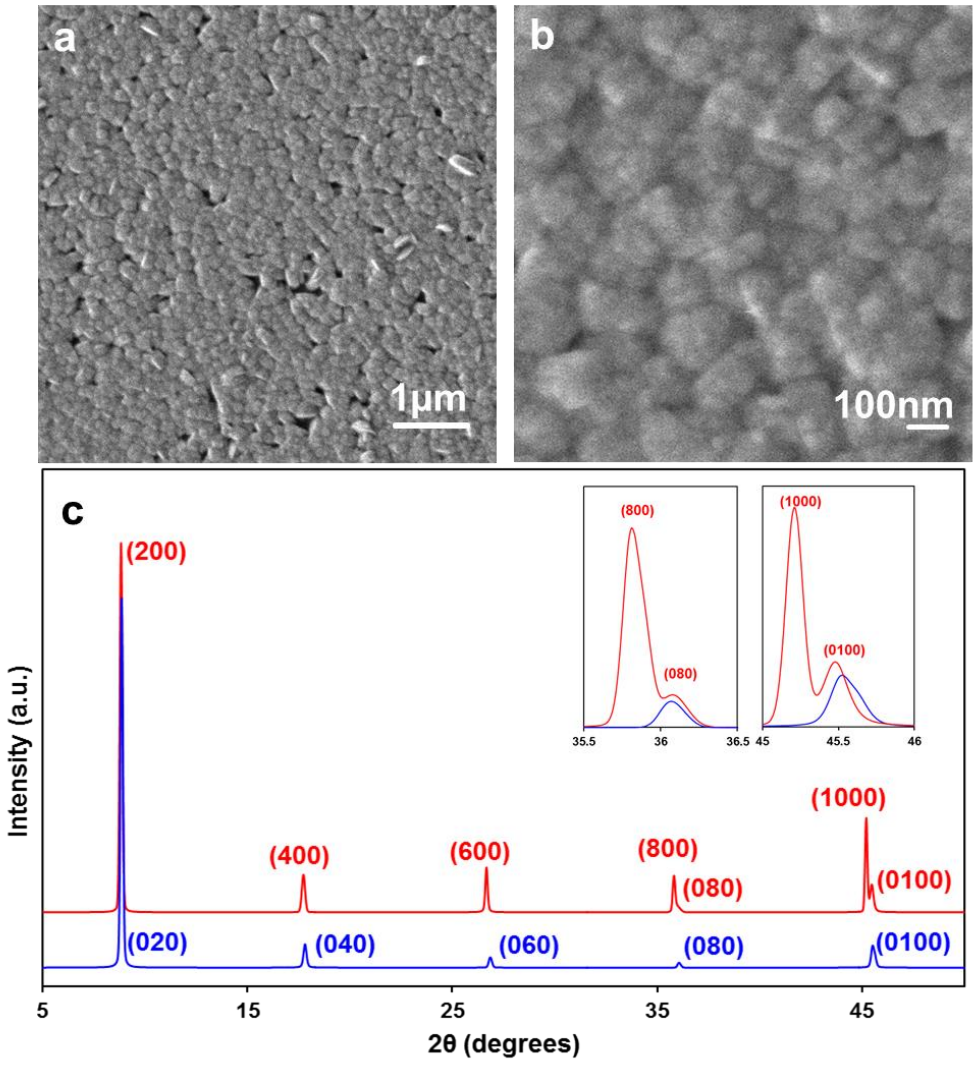

Figure 3-5: (a) SEM image of a *a*-&*b*-oriented film formed after growth of a *b*-oriented coating of 2D-MFI nanosheets in a sol of composition 0.15 TPAOH: 1TEOS: 135H_2O at 90° C for 24 h. (b) Higher magnification image of the film in (a). (c) Out-of-plane XRD pattern from the film in (a), shown in red, overlaid with the corresponding pattern of a film grown using TEAOH-based sol, shown in blue. The film grown using a TPAOH-based sol is *a*-&*b*-oriented whereas the one from TEAOH-based sol is *b*-oriented as evidenced by the presence and absence of splitting, respectively, of the corresponding high angle peaks shown in the insets.

In addition to lateral growth, thickening and appearance of steps on the previously flat nanosheet surfaces are evident (**Figures 3-6a and 3-6b**). Representative step heights measured along the marked *line-1* in **Figure 3-6b** are plotted in **Figure 3-6c** and show that the steps are predominantly 1 nm in height. Additional measurements of various sheets (**Figures 3-7 and 3-8**) showed that 90% of the step heights are approximately 1 ± 0.2 nm, which is equal to the height of a pentasil chain, the fundamental building unit of MFI (**Figure 3-9**). These observations indicate that under the conditions reported here nanosheet thickening proceeds via 2D nucleation followed by step propagation.

In-plane growth was quantified by comparing the lateral dimensions of nanosheets before and after growth along their *a*- and *c*- axes (**Figures 3-6a and 3-6b**). The direction of maximum in-plane growth was assigned to the *c*-axis on the basis of an earlier report showing that TEAOH leads to faster growth along the *c*-axis.[87] The direction perpendicular to it was assigned as the *a*-axis of nanosheets. Dimensional changes calculated along the *c*- and *a*- axes of nanosheets after growth at different temperature and time are plotted against the corresponding change in thickness in **Figure 3-6d and 3-6e**, respectively. The anisotropy ratio – here, defined as the growth along in-plane directions (*c*- and *a*- axes) vs. change in thickness (growth along the out-of-plane *b*-axis) – is plotted against temperature in **Figure 3-6f**. The slow growth along the *a*- axis in TEAOH-based sols (to be contrasted with similar growth rates along *a*- and *c*- axes in TPAOH-based sols, **Figure 3-10**) suppresses the formation of *a*-oriented rotational intergrowths.

The above analysis of growth rates is based on observations from straight edges of nanosheets; however, some of the 2D-MFI nanosheets have fragmented edges resulting from damage during exfoliation and purification (**Figure 3-6g**).

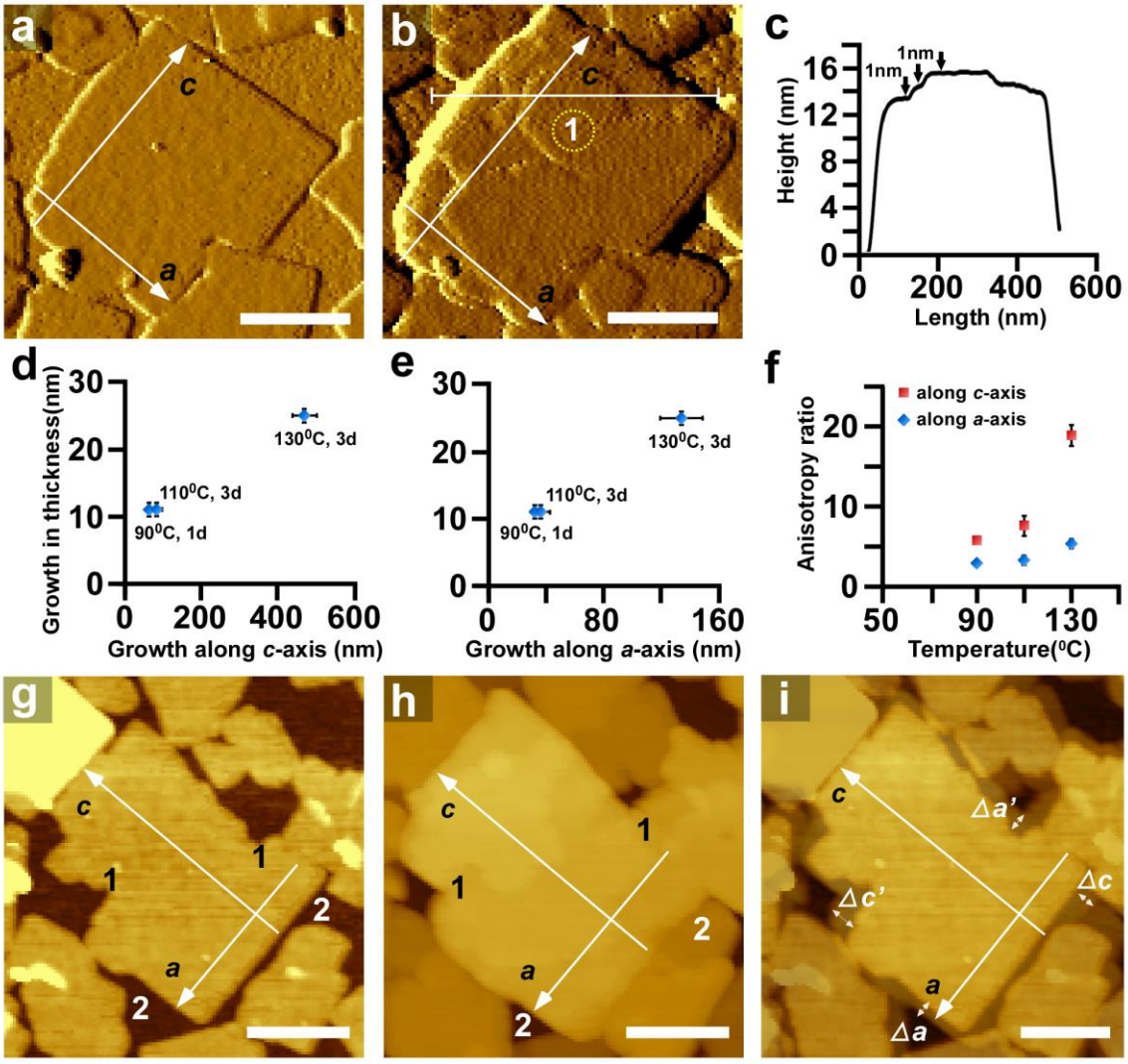

Figure 3-6: Quantification of nanosheet growth anisotropy in TEAOH-based sols. (a), (b) AFM amplitude mode images of a MFI nanosheet on Si wafer, before (a) and after (b) growth in a TEAOH-based sol at 110° C for 3 days. The *a*- and *c*-axes of the nanosheet are indicated. (c) Height profile along the marked *line-1* in (b) shows that the maximum thickness of the MFI nanosheet after growth is 16 nm with several 1 nm steps evident. (d), (e) Plots of nanosheet growth in thickness (along *b*-axis) vs. growth along *c*- axis (d) and *a*- axis (e) at different temperatures. Data at 90° C are from a sol composition of 0.198TEAOH: 0.002TPAOH: 1TEOS: 100H_2O. Data at 110° C and 130° C are from 0.2TEAOH: 1TEOS: 100H_2O. (f) Plot of anisotropy ratio vs. temperature,

where anisotropy ratio is the ratio of change of in-plane dimensions (nanosheet growth along *c*- or *a*- axes) over the change in thickness (out-of-plane growth, along *b*-axis). (g) AFM height image of a 3 nm thick MFI nanosheet supported on Si wafer showing irregularly fragmented edges (e.g., two regions marked "1" expose crystal faces other than (100) or (001), whereas regions such as the ones marked "2" expose the (100) and (001) crystal planes). (h) AFM height image of the same nanosheet shown in (g) after growth in a TEAOH-based sol. (i) Superposition of AFM height images shown in (g) and (h) to highlight differences in growth between regions marked "1" and "2". For irregularly fragmented edges, the change in dimensions along *a*- and *c*- are noted as Δ*a'* and Δ*c'* while the corresponding changes along flat edges are noted Δ*a* and Δ*c.* Typical ratios are 1.2 for (Δ*c'*/Δ*c*) and 2.8 for (Δ*a'*/Δ*a*). (Scale bars: 200 nm).

These irregularly fragmented edges expose crystal faces other than (100) or (001). It was observed that in-plane growth along the fragmented edges was greater as compared to that along well-defined edges (**Figures 3-6h, 3-6i and 3-11**). Growth rate ratios (growth along the *c*- or *a*- axes of a fragmented edge vs. growth along the same direction for non-fragmented edge) of 2.8 and 1.2 were observed along the nominal *a*- and *c*- axes, respectively. This observation suggests that irregularly fragmented nanosheets can self-heal to regular shapes during lateral intergrowth under the conditions reported here.

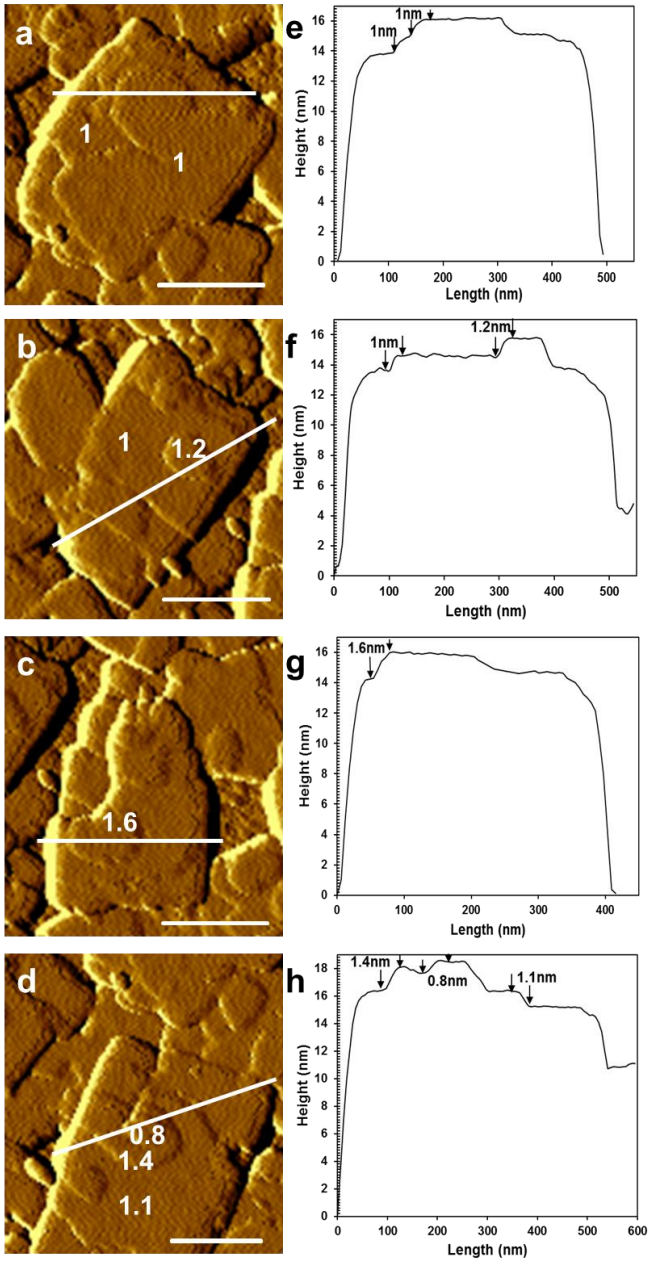

Figure 3-7: (a-d) AFM amplitude mode images of MFI nanosheets showing steps on their surfaces after growth in TEAOH-based sols of molar composition 0.2 TEAOH: 1TEOS: 100H_2O at 110° C for 3 days; Profiles used to determine step heights are marked and certain step heights are indicated in nm. (e-h) Plots of step heights along the marked profiles in figures (a-d), respectively. (Scale bars: 200 nm)

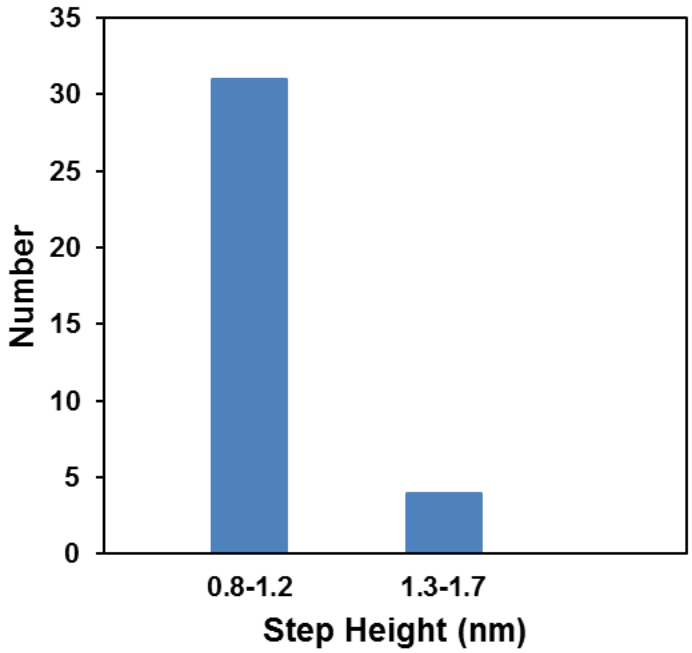

Figure 3-8: Histogram of step heights showing, 90% of the steps are ~1 nm.

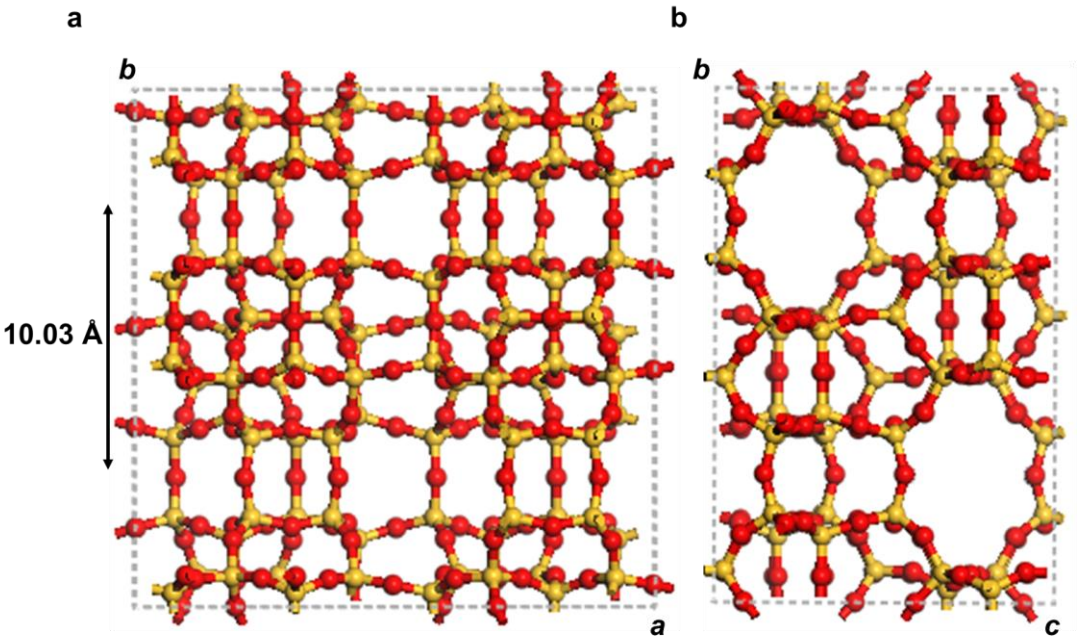

Figure 3-9: (a) Schematic of MFI crystal structure projected along the *c*-axis, showing the ~ 1 nm height of a pentasil chain layer. (b) Projection down the *a*-axis.

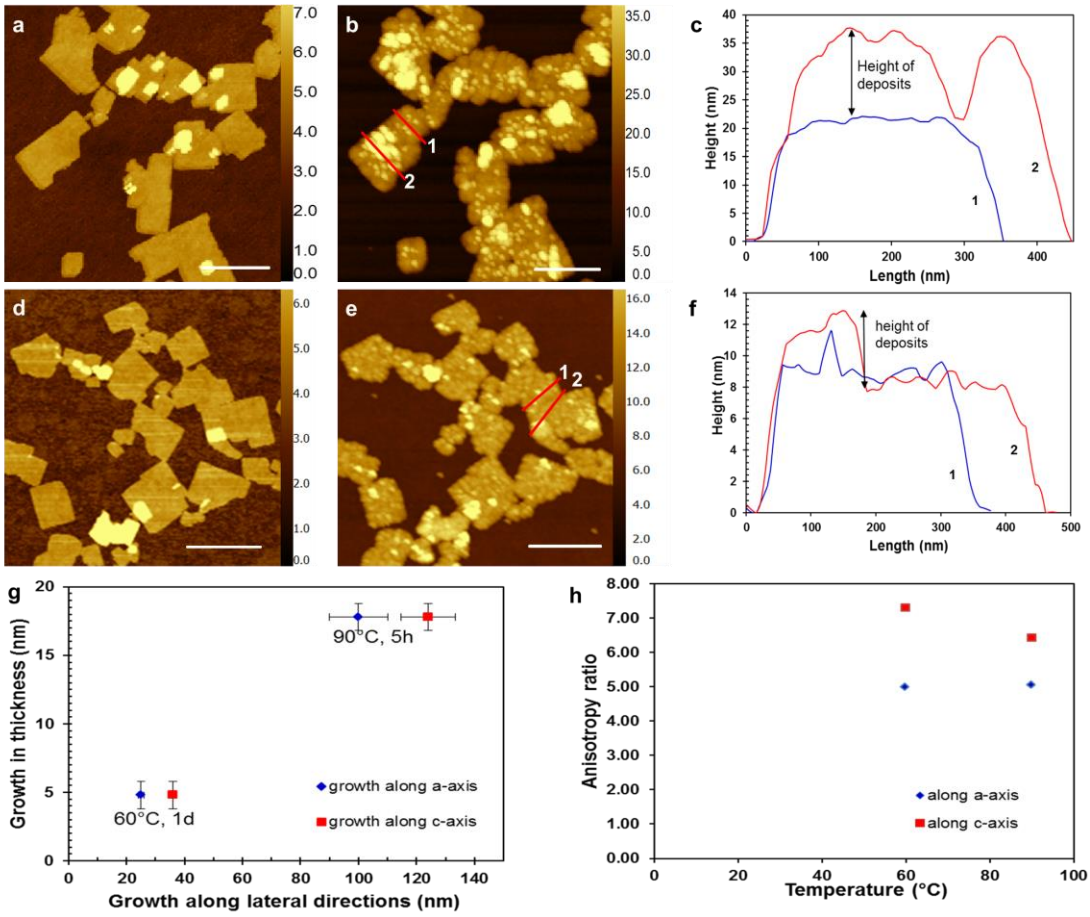

Figure 3-10: (a) AFM height image of a 2D-MFI nanosheet coating. (b) AFM height image of the same region as in (a) after growth in a TPAOH-based sol of composition 0.2TPAOH: 1TEOS: 200H_2O at 90° C for 5 h. (c) Heights along the profiles shown in (b), by lines marked 1 and 2, revealing deposit roughness as high as 20 nm. (d) AFM height image of a 2D-MFI nanosheet coating. (e) AFM height image of the same region as in (d) after growth in a TPAOH-based sol of composition 0.2TPAOH: 1TEOS: 200H_2O at 60° C for 24 h. (f) Heights along the profiles shown in (e), by lines marked 1 and 2, indicating roughness of 5 nm. (g) Plot of increase in thickness vs. growth along the indicated (*a*- and *c*-axes) in-plane directions. (h) Plot of the anisotropy ratio as a function of temperature. Thicknesses reported in panels (g) and (h) consider only the flat regions, not accounting for regions of large roughness. (Scale bars: 500 nm)

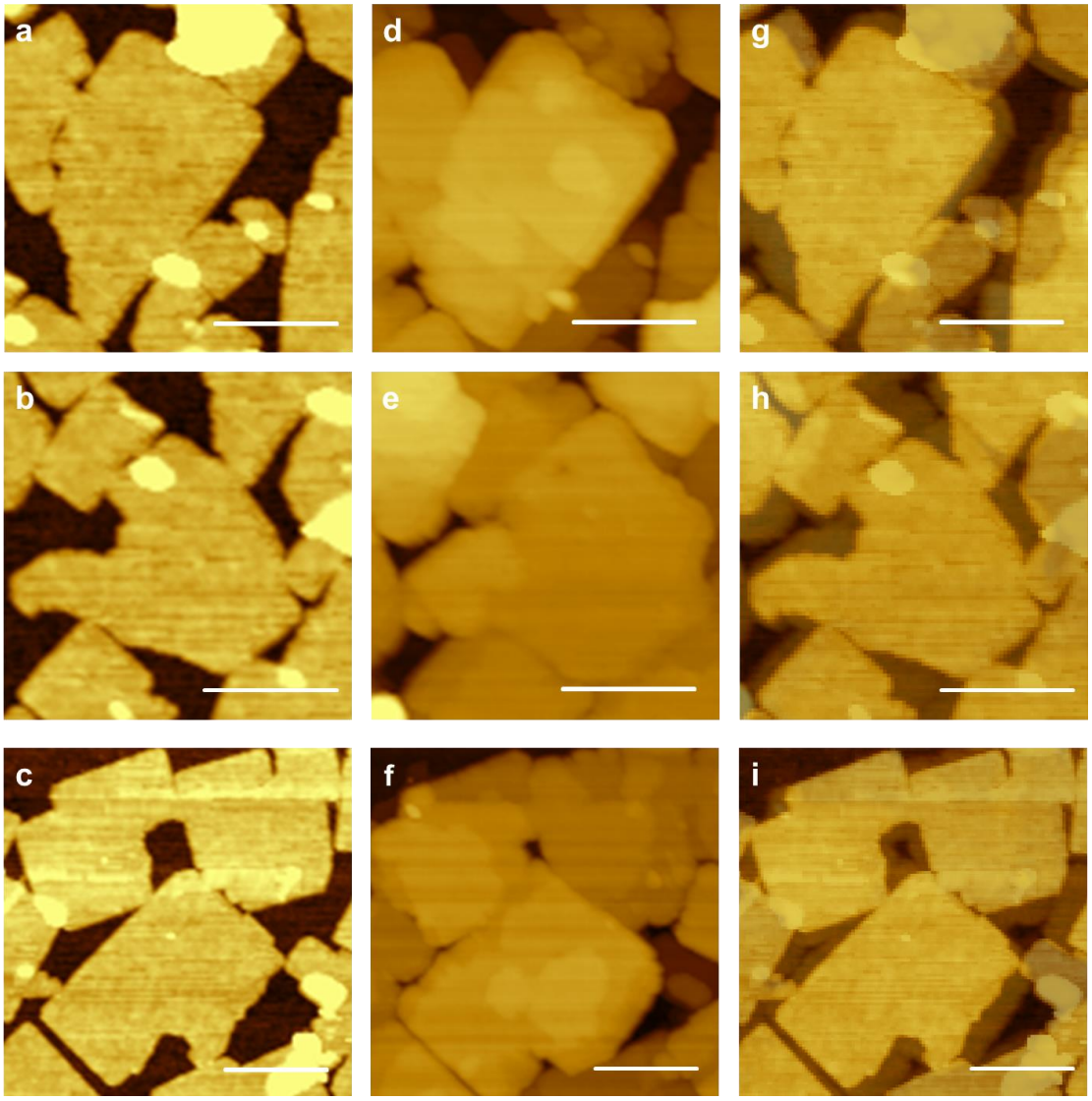

Figure 3-11: (a-c) AFM height images of 2-D MFI nanosheets having fragmented edges exposing crystal faces other than (100) and (001) in the in-plane directions. (d-f) AFM height images of the nanosheets shown in (a-c) respectively, after growth in a TEAOH-based sol at 110° C, for 3 days (conditions as described in Figure 3-6), showing enhancement of growth along the irregularly fragmented edges. (g-i) Superimposition of height images before and after growth. (Scale bars: 200 nm)

Another important observation is that nanosheets with smaller lateral dimensions thickened less as compared to neighboring larger nanosheets (**Figures 3-12a, 3-12b and 3-13**), which is consistent with thickening rate being determined by the frequency of surface nucleation events (expected to be positively correlated with nanosheet lateral surface area). This finding could have implications in the evolution of film microstructure during nanosheet growth for membrane applications because it suggests that an optimal aspect ratio of nanosheets exists that achieves a balance between the efficient coverage of porous supports (requiring large lateral dimensions) and the reduced propensity to thickening during lateral intergrowth (favored by smaller nanosheets).

Size correlated suppression in thickening was also evident in cases where a small nanosheet on top (top layer) of a relatively large nanosheet thickened less as compared to the larger underlying nanosheet (bottom layer) (**Figure 3-14**). This observation also highlights that layer growth is inhibited when the growth front encounters the misoriented step caused by the top layer. Another case of inhibited nanosheet thickening is also evident when comparing the growth of overlapping bilayer regions with the corresponding growths for the nanosheets involved in the overlap but far removed from the overlap region. In most cases (i.e., 24 out of 26 overlaps investigated), it was seen that the overlapped regions thickened less as compared to the change in thickness determined in the adjacent non-overlapping regions of the nanosheets (**Figures 3-12c, 3-12d and 3-15**). The inhibition of step propagation for steps nucleated on the bottom layer once they encounter the misoriented step caused by the top layer could be understood based on the above discussion of **Figure 3-14**. But, what could cause the inhibition of step propagation on the surface of the top layer? Apparently, the surface of the top layer when climbing over the bottom layer

adapts a certain curvature causing deviations from its nominal unperturbed crystal structure and this deviation is sufficient to suppress the propagation of steps that have been nucleated in the flat regions. This hypothesis is corroborated by more pronounced cases of surface curvature defects such as *wriggles* within single nanosheets. Indeed, **Figure 3-16** shows two examples where a wriggle, detectable by AFM, inhibits thickening by propagation of steps nucleated on another region of the same nanosheet.

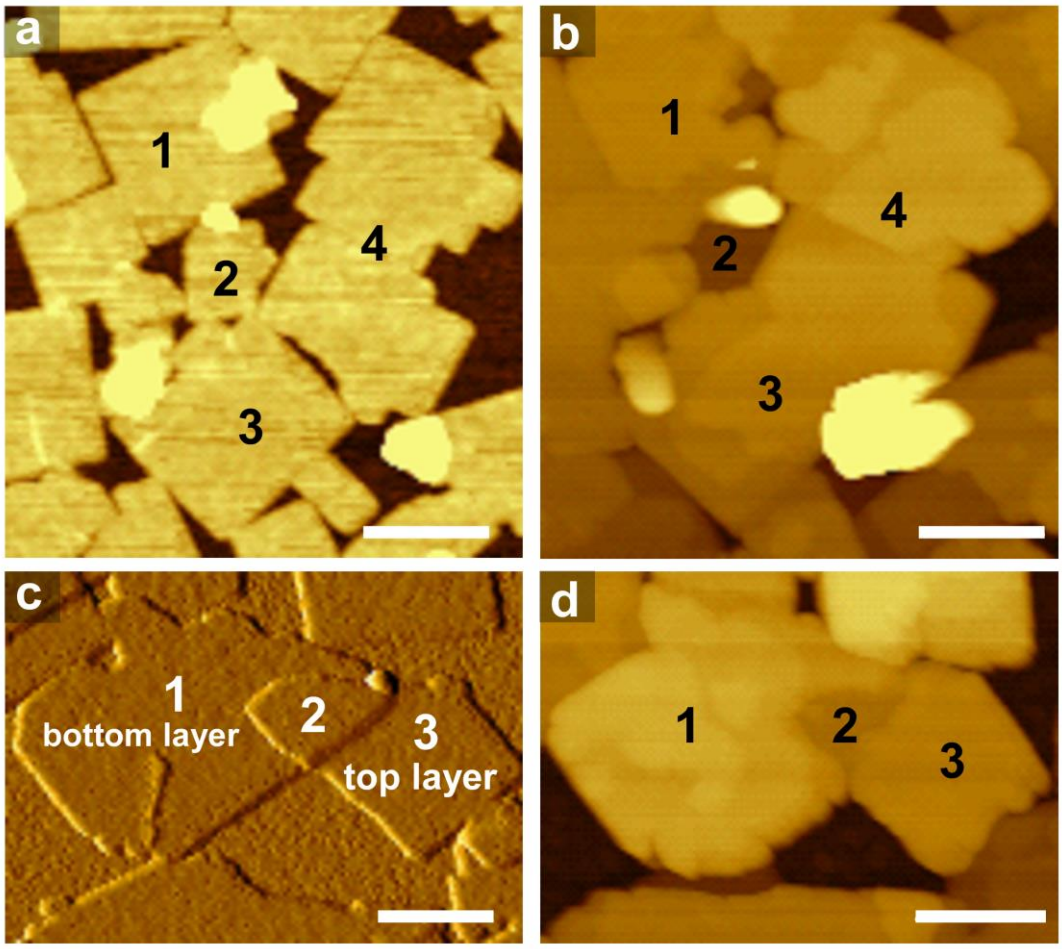

Figure 3-12: Effect of nanosheet size and curvature on TEAOH-based growth. (a) AFM height image of a region with a relatively small nanosheet (marked "2") surrounded by bigger ones ("1", "3" and "4"). (b) AFM height image of the same region as in (a) after growth in a TEAOH-based sol of molar composition 0.2TEAOH: 1TEOS: 100H_2O at 110° C for 3 days. The relatively small nanosheet "2" thickened to 4 nm whereas the larger nanosheets "1, 3, and 4" thickened to 10 nm. (c) AFM amplitude mode image of a nanosheet, "3" (top layer-TL), on top of another nanosheet, "1" (bottom layer-BL), giving rise to an overlap region, "2". (d) AFM height image of the same region as in (c) after growth in a TEAOH-based sol at 110° C for 3 days, where the overlap region "2" has thickened to 6 nm as compared to 14 and 10 nm thickening of regions "1" and "3", respectively. (Scale bars: 200 nm)

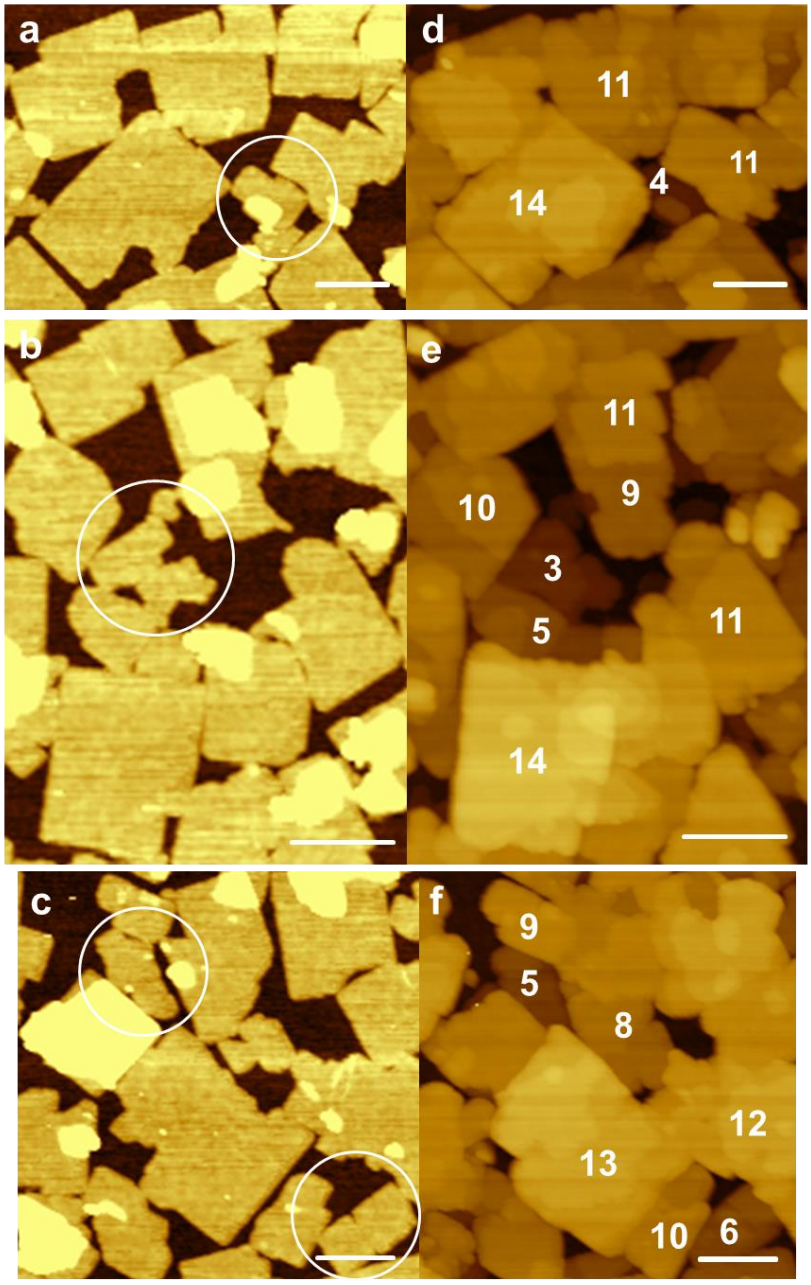

Figure 3-13: (a-c) AFM height images of regions with relatively small nanosheets (circled) surrounded by larger ones. (d-f) AFM height images of the regions in (a-c), respectively, after growth (conditions as described in Figure 3-12). Numbers on the nanosheets denote a change (in nm) in their thickness after growth. Small nanosheets thicken less as compared to the larger ones. (Scale bars: 200 nm)

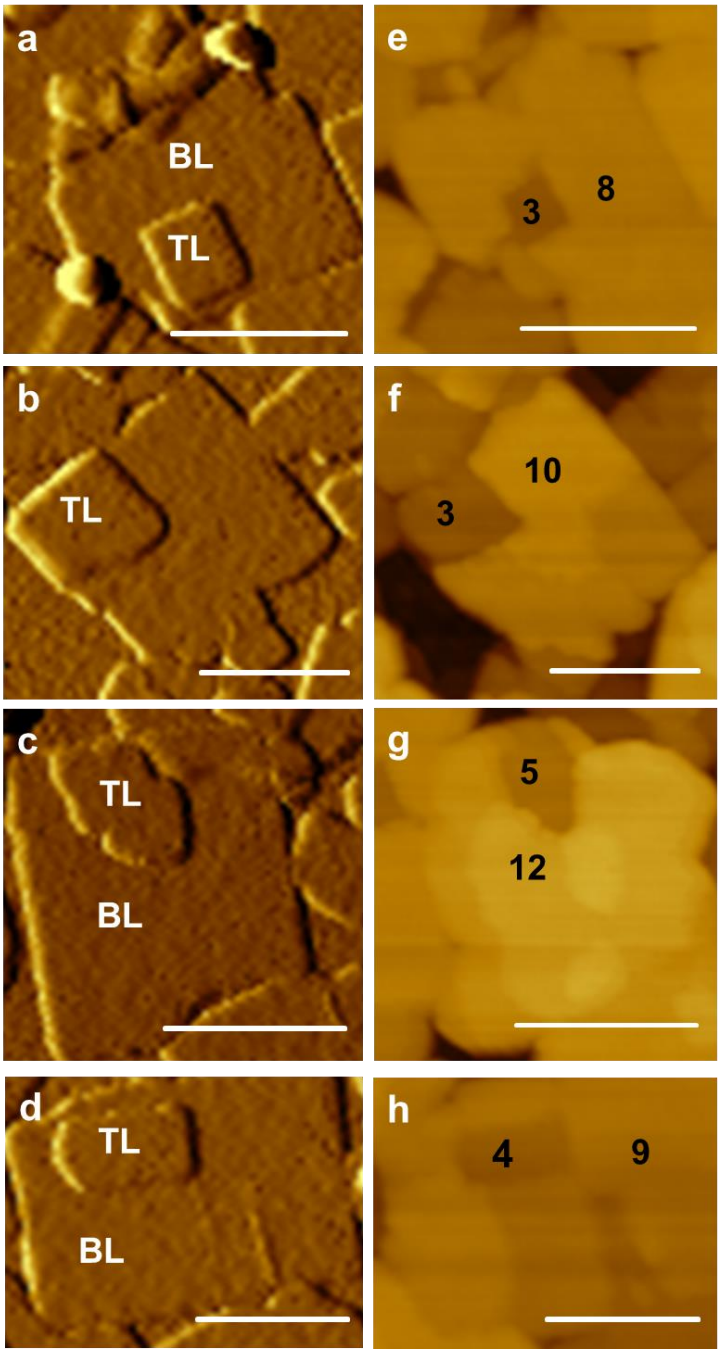

Figure 3-14: (a-d) AFM amplitude mode images of larger nanosheets with a small nanosheet on top before growth. (e-h) AFM height images after growth in a TEAOH-based sol (conditions as described in Figure 3-12). Numbers on the sheets denote a change in their thickness after growth (in nm). Small nanosheets on top (TL – top layer) thicken less as compared to the larger ones beneath (BL – Bottom layer). (Scale bars: 200 nm)

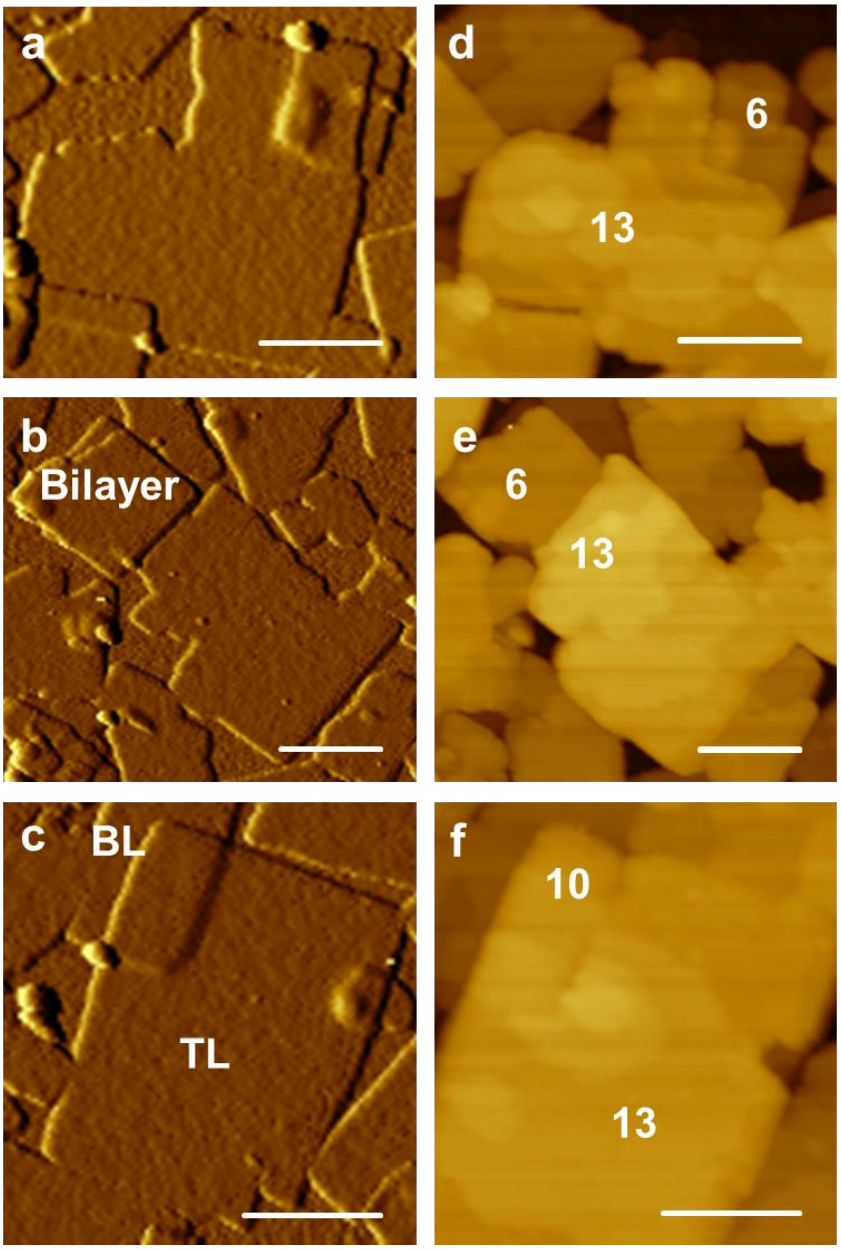

Figure 3-15: (a-c) AFM amplitude mode images, of overlapping bilayer regions before growth. (d-f) AFM height images after growth in a TEAOH-based sol (conditions as described in Figure 3-12). Numbers on the sheets denote a change in their thickness after growth (in nm). The overlapped regions thicken less as compared to the nanosheets involved in the overlap but far removed from it. (TL – Top layer, BL – Bottom layer) (Scale bars: 200 nm)

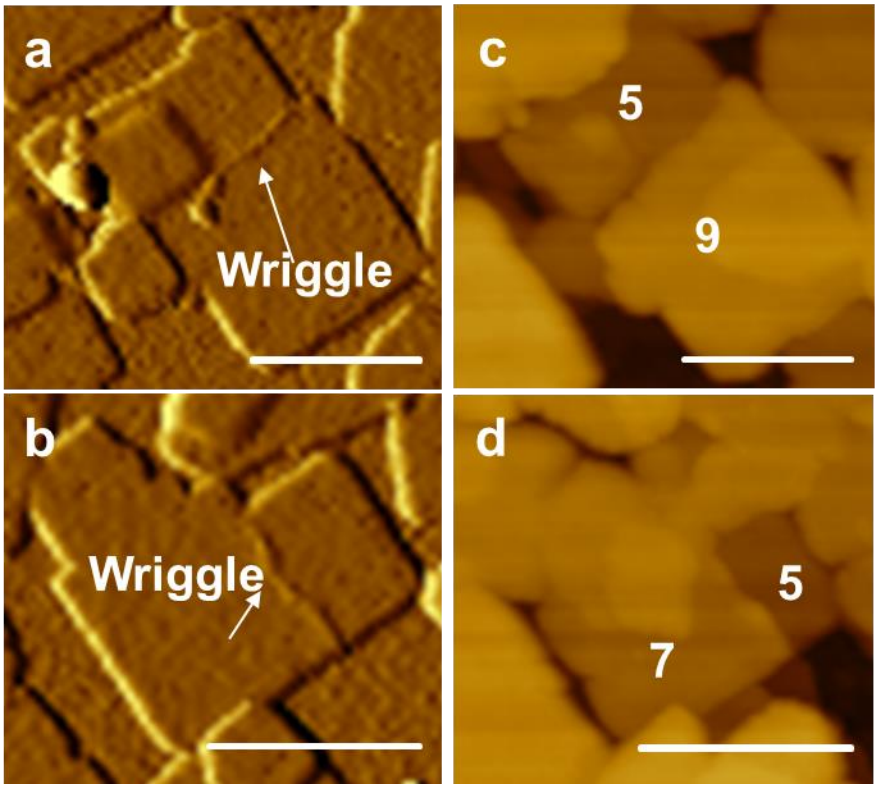

Figure 3-16: (a-b) AFM amplitude mode images of 2D-MFI nanosheets with a wriggle detectable by AFM. (c-d) Corresponding AFM height images after growth in a TEAOH-based sol (conditions as in Figure 3-12) with numbers on the sheets denoting change in their thickness (in nm). (Scale bars: 200 nm)

The slow and controllable growth described here allows for unprecedented nanoscale control of MFI nanosheets and crystals and is expected to find immediate uses beyond the preparation of thin molecular sieve films and membranes. For example, we found it can also be used to tune the thickness of zeolite domains in hierarchical catalysts. Starting from particles of the material called self-pillared pentasil zeolite (SPP),[48] which are made of single-unit-cell (2 nm thick) MFI nanosheets intergrown orthogonally to each-other to create a house-of-cards arrangement, we were able to controllably thicken the zeolite domains with nm resolution (**Figure 3-17**) and preserve the particle morphology.

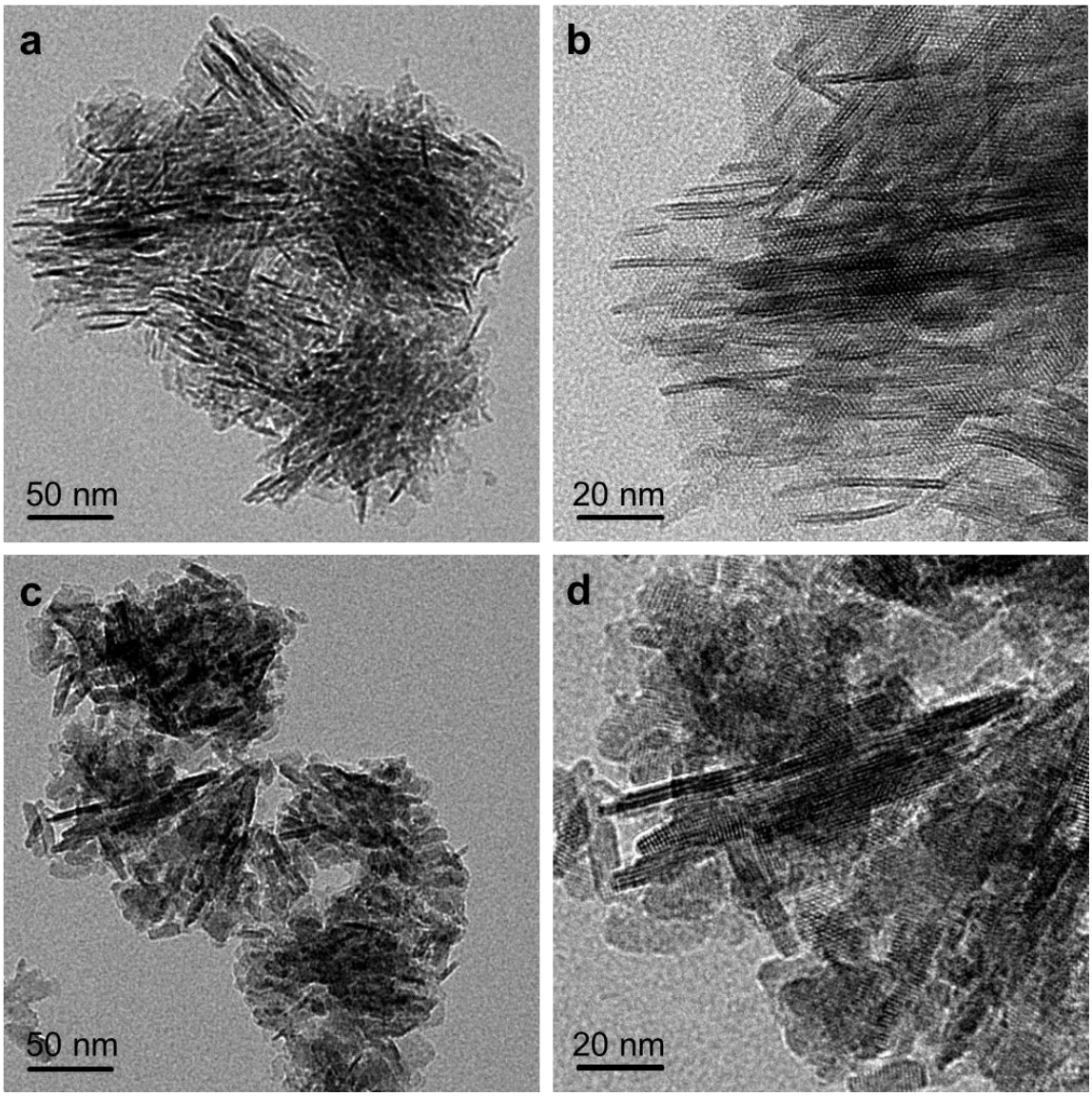

Figure 3-17: (a) TEM image of hierarchical single unit-cell zeolite consisting of intergrown MFI layers, called self-pillared pentasil (SPP). (b) High resolution TEM image of SPP, showing single-unit-cell MFI layers with thickness of ~ 2 nm. (c) TEM image of SPP after growth in a TEAOH-based sol of molar composition 0.2TEAOH: 1TEOS: 100H_2O at 110° C for 17 hours. (d) High resolution TEM image of the material shown in (c), indicating an average layer thickness of 5 ± 1 nm.

3.5 Conclusions

The slow and controllable growth conditions developed in this chapter allow unprecedented control of zeolite MFI crystal growth. This ability to manipulate the microstructure of thin films and hierarchical catalysts at a scale that approaches single-unit-cell dimensions will offer tremendous potential to improve their properties in a range of commercial applications.

Furthermore, the growth conditions developed in this chapter are robust enough to be transferred for the growth of MFI crystals of varied morphologies supported on different substrates. For example, micron-sized coffin shaped MFI crystals supported on gold coated Si-wafer were intergrown using these growth conditions leading to a zeolite thin film having one of the lowest reported dielectric constants[30]. 5.5 nm MFI nanosheets supported on porous silica supports could also be intergrown using these conditions[28].

Chapter 4: Direct Synthesis of Cu(BDC) MOF Nanosheets and Their Performance in Mixed Matrix Membranes

Parts of this chapter are published as:

M. Shete, P. Kumar, J. E. Bachman, X. Ma, Z. P. Smith, W. Xu, K. A. Mkhoyan, J. R. Long and M. Tsapatsis., *J. Memb. Sci,* 549, 312-320 (2018).

Reproduced with permission from Elsevier.

4.1 Chapter Overview

In this chapter, a simple and scalable direct synthesis of Cu(BDC) (BDC^{2-} = 1,4-benzenedicarboxylate) MOF nanosheets is described. High aspect-ratio nanosheets with an average lateral size of 2.5 μm and a thickness of 25 nm are obtained from a well-mixed solution. Characterization of the nanosheets by powder and thin film X-ray diffraction, electron microscopy, and electron diffraction reveals pronounced structural disorder that may affect their pore structure. Incorporation of the Cu(BDC) nanosheets into a Matrimid polymer matrix results in mixed matrix membranes (MMMs) that exhibit a 70 % increase in the CO_2/CH_4 selectivity compared with that of Matrimid. Analysis of permeation data for Cu(BDC) MMMs using a mathematical model for selective flake composites indicates that further performance improvements could be achieved with the selection of different polymers for use in the continuous phase.

4.2 Introduction

Metal-organic frameworks (MOFs) are a class of crystalline porous materials with a wide range of pore sizes and functionalities that render them attractive for a variety of potential applications[16,17], including catalysis[36,37], gas storage[39,109], and separations[38,42,110]. Particularly, certain MOF-based membranes are considered for separation of carbon dioxide from natural gas and flue gas streams[43,111].

Recently, membranes based on zeolite nanosheets were reported to exhibit unprecedented separation performance (high flux and selectivity)[26,27], which motivated the synthesis of MOF nanosheets and exploration of their uses in membrane applications[40,44,112,113]. As with other molecular sieve membranes[96], MOF nanosheet-based membranes are typically prepared either by (i) forming intergrown deposits of MOF nanosheets on porous supports in an effort to obtain the intrinsic separation properties of the nanosheets[40,113], or (ii) incorporating the nanosheets in polymer matrices to form mixed matrix membranes (MMMs)[44] that surpass the Robeson upper bound for polymeric membrane performance[114]. It has been convincingly argued that, from a manufacturing standpoint, the MMM approach is advantageous because it can be readily integrated with existing technologies for forming polymeric membranes[115–117]. Moreover, nanosheet-based MMMs can in principle achieve similar improvements in performance at lower loadings compared to MMMs formed with isotropic crystals[68,118–120].

The strategies employed for the synthesis of MOF nanosheets can be categorized into: (i) a top-down approach involving exfoliation of layered precursors using techniques such as sonication and ball-milling[40,121], or (ii) a bottom-up approach where crystal growth of MOFs having a tendency to grow anisotropically is tuned to favor the formation of plate-like morphologies by restricting growth along the preferred thin direction either via the adsorption of surfactant-like molecules[112] or by altering the manner in which metal and linker ions come into contact with each other[44]. As recently demonstrated for zeolite nanosheets, the bottom-up approach can often be more advantageous, not only because of its simplicity and higher yields, but also in terms of improved nanosheet quality enabling significantly better membrane performance[28].

Building on an earlier report that required nanosheet crystallization in a three-layer (linker-solvent-metal) gradient[44], we report here the bottom-up synthesis of Cu(BDC) nanosheets by direct homogeneous mixing of the metal and linker solutions. We find that it is possible to tune the aspect-ratio of the nanosheets by varying the synthesis temperature, and carry out detailed structural characterization using electron microscopy and X-ray diffraction. Mixed matrix membranes are successfully fabricated by incorporating the nanosheets into a polymer matrix. We obtain effective permeabilities for the Cu(BDC) nanosheets from permeation data and analyze the MMM performance using a mathematical model.

4.3 Experimental

4.3.1 Chemicals

Anhydrous *N*, *N*-dimethylformamide (DMF, 99 %), terephthalic acid (H_2BDC, 98 %) and copper nitrate trihydrate ($Cu(NO_3)_2$, 99 %) were obtained from Sigma Aldrich. Acetonitrile (CH_3CN, 99.9 %), and chloroform ($CHCl_3$, 99.9 %) were obtained from Fisher Scientific. Matrimid 5218 was provided by Huntsman Advanced Materials and was degassed at 180 °C under reduced pressure (0.1 bar) for 16-18 h. Chloroform was filtered using a 0.2 µm PTFE syringe filter (Pall Corporation). All other chemicals were used as received.

4.3.2 Direct Synthesis of Cu(BDC) nanosheets

4.3.2.1 Direct synthesis – no mixing

The metal solution was prepared in a glass vial by adding 1 mL of DMF and 3 mL of CH_3CN to 30 mg of $Cu(NO_3)_2$. The linker solution was prepared by adding 3 mL of DMF and 1 mL of CH_3CN to 30 mg of H_2BDC. The metal solution was added in one portion to the linker solution and the resulting mixture was left to stand at ambient temperature. After

24 h, the solution was centrifuged to obtain Cu(BDC) nanosheets that were then washed 3× in DMF. The nanosheets were stored by suspending them in DMF.

4.3.2.1 Direct synthesis – gentle mixing with shaker

Typically, the metal solution was prepared in a conical flask by adding 30 mL of DMF and 90 mL of CH_3CN to 900 mg of $Cu(NO_3)_2$ while linker solution was prepared by adding 90 mL of DMF and 30 mL of CH_3CN to 900 mg of H_2BDC. The metal solution was then added dropwise to the linker solution over a period of 40 min under magnetic stirring. After complete addition, the resulting solution mixture was shaken in an orbital shaker (Thermo Scientific MAXQ 4000) at a speed of 200 rpm under a constant temperature (15° C, 25° C, or 40° C). After 24 h at the set temperature, the solution was centrifuged to obtain Cu(BDC) nanosheets, which were then washed 3× in DMF. A suspension of the Cu(BDC) nanosheets in DMF was then solvent exchanged in chloroform by repeated centrifugation. The supernatant was discarded each time and ~40 mL of fresh chloroform was added to the sediment (corresponding to ~2.5 mg of wet nanosheet cake per mL of chloroform). The cake was dispersed by vortexing (Fisher Scientific vortex mixer) for ~5 min, sonicated (Branson 5510R-DTH ultrasonic cleaner) for ~15 min, and then centrifuged. This process was repeated 3×. The nanosheets thus suspended in chloroform were eventually used for the fabrication of MMMs.

4.3.3 Characterization of Cu(BDC) nanosheets

4.3.3.1 X-Ray Diffraction (XRD)

After washing in DMF, the cake of Cu(BDC) nanosheets was oven dried at 70° C. The dried as-synthesized powder was then added to a polyimide capillary (Cole-Parmer, 0.0395 inch inner diameter × 0.0435 inch outer diameter, 0.6 inch in length) that was then sealed

at both ends. X-ray diffraction measurements were performed at beamline 17-BM at the Advanced Photon Source, Argonne National Laboratory (APS, ANL). A Perkin Elmer amorphous silicon flat panel detector was used to acquire two-dimensional diffraction patterns with program QXRD. The data were converted to traditional xy files of intensity versus 2θ using the GSAS-II program[122]. The X-ray wavelength was 0.24119 Å. Values of 2θ were correspondingly converted to Cu-Kα radiation.

For out-of-plane X-ray diffraction, a suspension of nanosheets in DMF was drop-cast onto a porous silica support to obtain an oriented coating. Out-of-plane X-ray diffraction measurements were performed at Beamline 33-BM-C at APS, ANL using a source wavelength of 0.77493 Å. After converting 2θ values to Cu-Kα radiation, the data were processed using MDI-JADE 2.6.5 software.

Cu(BDC) nanosheets, solvent exchanged in chloroform, were characterized using in-plane X-ray diffraction. The sample was prepared by depositing nanosheets suspended in chloroform onto porous silica supports by vacuum filtration. In-plane measurements were performed at Beamline 33-BM-C at APS, ANL using a source wavelength of 0.77493 Å, and 2θ values were correspondingly converted to Cu-Kα radiation. The data were processed to subtract a linear background using MDI-JADE 2.6.5 software.

4.3.3.2 Scanning Electron Microscopy (SEM)

SEM analysis was performed using JEOL 6700 and Hitachi SU8230 scanning electron microscopes. An accelerating voltage of 1.5 kV was used with the JEOL 6700 equipped with a field emission gun. The Hitachi SU8230 was operated in the deceleration mode at a

landing voltage of 0.8 kV. Samples for SEM analysis were prepared by drop casting the nanosheet suspension onto a Si wafer.

4.3.3.3 Transmission Electron Microscopy (TEM) and Selected Area Electron Diffraction (SAED).

A FEI-Tecnai T12 TEM with LaB_6 filament gun operating at 120 kV and equipped with a Gatan MSC794 CCD camera was used for TEM imaging and SAED. Cu(BDC) nanosheets were transferred from suspensions onto lacey carbon films supported on 400 mesh copper grids, and the solvent was allowed to evaporate before TEM analysis. Simulated electron diffraction patterns were obtained using the Single Crystal 2.3 software. Radial averaging of electron diffraction pattern was performed using a MATLAB code to determine the center of the ED pattern, followed by radial averaging of the peak intensity in reciprocal space. A line scan (*counts vs* 2θ after exponential background subtraction), starting from the center of the radially averaged ED pattern, was plotted for comparison with the X-ray diffraction pattern.

4.3.3.4 Atomic Force Microscopy (AFM)

A Bruker Nanoscope V Multimode Scanning Probe Microscope was used in tapping mode in the repulsive regime for collecting AFM images. A silicon nitride tip was used, and AFM images were collected at a scan rate of 0.8 Hz and 512 lines/scan. Samples for AFM analysis were prepared by drop casting the nanosheets suspension on a Si wafer. Gwyddion 2.4 software was used to analyze AFM images.

4.3.3.5 Annular Dark-Field Scanning Transmission Electron Microscopy (ADF-STEM)

Samples for ADF-STEM characterization were prepared by drop-casting a suspension of Cu(BDC) nanosheets onto an ultrathin carbon film on holey carbon support film (400 mesh Cu, from Ted Pella) and allowing the sample to air dry at room temperature. ADF-STEM images were acquired using aberration-corrected FEI Titan 60-300 (S)TEM, equipped with SuperX EDX detector, operating at 60 kV, with a 214 mrad electron probe convergence angle and 30 mrad ADF detector inner angle. The acquired ADF-STEM image was filtered by selecting the spots in Fast Fourier Transform (FFT) of the original image, followed by inverse FFT operation to generate a real space image.

4.3.4 Fabrication of MMMs

Nanosheets suspended in chloroform were used for fabricating MMMs. To determine the concentration of the stock suspension a *calibration film* was made. A known volume (2 mL) of the suspension in chloroform was added to a 2 wt% solution of Matrimid in chloroform. The MOF-polymer solution was shaken in an orbital shaker at 250 rpm for 1 h and then sonicated for 30 min (Branson 5510R-DTH ultrasonic cleaner). Shaking and sonication cycles were repeated 3× and then the solution was cast in a home-built flat bottom glass well. The solvent was then allowed to evaporate over a period of 24 h, after which time the film was peeled off. The film was activated at 180° C under reduced pressure (0.1 bar) for 16-18 h. Loading of MOF nanosheets in the *calibration film* was determined by thermogravimetric analysis (TGA) using the data from TGA of MOF nanosheets powder as a reference. TGA was performed using a Shimadzu TGA-50 analyzer. Samples were activated under air (60 mL/min) at 120° C for 1 h before TGA profiles were collected at a ramp rate of 10° C/min up to 850° C. The percentage of mass

remaining after ramping to 850° C was attributed to the mass of metal oxide. By comparing this mass with the mass of metal oxide remaining after TGA on a known weight of MOF powder, the loading of MOF nanosheets in the *calibration film* was determined, and thereby the concentration of the stock solution.

MMMs comprised of different loadings of MOF nanosheets were fabricated following the same procedure as that for the *calibration film*. Film thicknesses were measured using a digital micrometer (Mitutoyo) and found to be in the range of 35-50 μm.

4.3.5 Single gas permeation measurements

Permeation measurements were performed in a constant-volume, variable-pressure apparatus that was built in-house. A 2.2 cm membrane coupon was cut out from the films and affixed to a stainless-steel fender washer using Loctite epoxy. The fender washer was then sealed tightly in a permeation cell. The system was evacuated overnight before gas permeability measurements were initiated. Permeation of N_2, followed by CO_2, was tested at three different feed pressures. The rate of pressure increase observed upon isolation of the permeate side from vacuum was used to determine the gas permeability values. A leak rate of the system (including the membrane cell) was determined by sealing a dense metal disk into the permeation cell and then measuring the pressure increase on the permeate side upon vacuum isolation. The leak rate was subtracted when calculating the gas permeability using equation (1),

$$P = \frac{lV}{Ap_f RT}\left[\left(\frac{dp}{dt}\right)_{ss} - \left(\frac{dp}{dt}\right)_{leak}\right] \quad (1)$$

where l is the film thickness, V is the volume of the chamber into which the gas is allowed to accumulate, A is the area of the film exposed to the gas, p_f is feed pressure, R is universal gas constant, T is the absolute temperature, $(dp/dt)_{ss}$ is the steady state permeation rate and $(dp/dt)_{leak}$ is the leak rate). Permeability values are reported in the units of Barrer. Leak rates correspond to permeabilities smaller than 0.04 Barrer for a 50 μm film.

4.3.6 Mixed gas permeation measurements

Mixed gas measurements were performed using a constant volume variable pressure apparatus as described in Ref. 42. Samples for mixed-gas testing were supported on brass shim stock disks using polydimethylsiloxane (PDMS) glue. Supported membranes were loaded in a stainless-steel filter holder (Millipore XX4404700). Feed consisting of a gas mixture of 50:50 CO_2 in CH_4 was flowed at a rate > 100× permeation rate to avoid concentration polarization. The gas mixture was allowed to permeate the membrane until a steady-state permeation rate was reached (> 6-time lags) after which the permeate volume was evacuated and allowed to accumulate under steady state conditions. The permeate volume collected was then expanded into a mass spectrometer (MKS Microvision 2) for composition analysis. The mass fraction of (mass 44)/ [(mass 44) + (mass15)] was used to determine the mixed gas selectivity. For calibrating the mass fraction, standards with 10 %, 50 % and 90 % CO_2 in CH_4 were used.

4.4 Results

4.4.1 Synthesis of Cu(BDC) nanosheets

The bottom-up synthesis of Cu(BDC) nanosheets was first reported by Rodenas and coworkers[44], wherein they used a three-layer gradient scheme that involved separating layers of the metal and linker solutions by a spacer solution to achieve diffusion-mediated modulation of crystal growth kinetics. We found this method to be robust and readily reproducible (**Figure 4-1**). However, gradient crystal growth methods are low-yield and arguably difficult to scale up. Therefore, we explored bottom-up synthesis conditions that would eliminate the need for gradient synthesis.

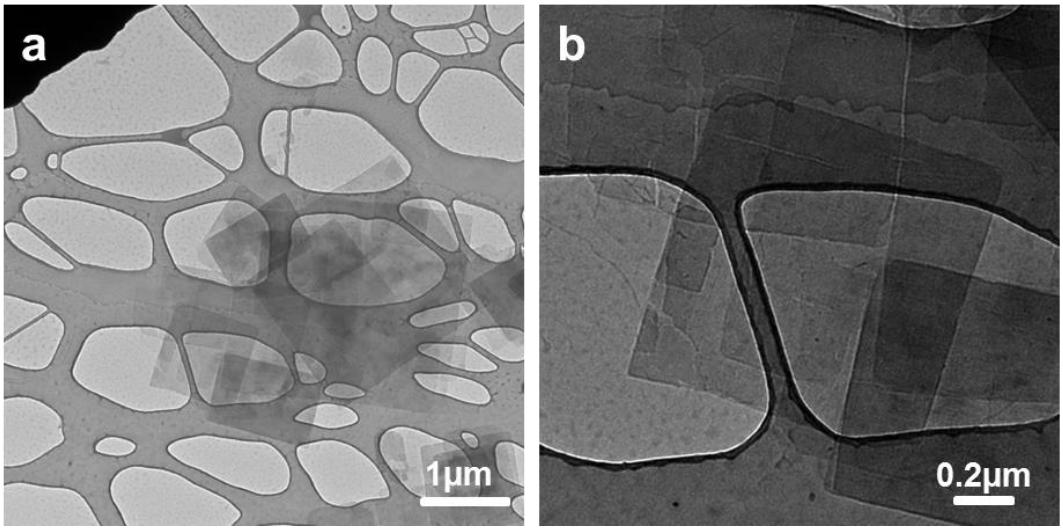

Figure 4-1: (a), (b) Cu(BDC) nanosheets obtained by following the three-layer gradient synthesis method reported by Rodenas et al. (Ref. 44) The nanosheets have average lateral size of 1.8 ± 0.5 µm and average thickness of 25 nm.

Considering that the inherent crystal growth kinetics of Cu(BDC) favor a plate-like morphology[123–125], we hypothesized that it should be possible to tune the thickness of the

bulk crystals and form nanosheets by appropriate variation of the metal and linker concentrations during synthesis as well as the synthesis temperature.

Our first attempt was at synthesis involving direct addition of metal solution to linker solution in one portion and letting the resulting mixture remain static for 24 h at room temperature. Typically, the metal solution was prepared by dissolving the metal salt in a 3:1 volume ratio of CH_3CN: DMF while the linker solution was made by dissolving H_2BDC in a 1:3 volume ratio of CH_3CN: DMF, as described in section 4.3.2.1. As seen from **Figure 4-2a**, direct synthesis without any mixing of the synthesis solution yields Cu(BDC) nanosheets that have an average lateral size of 3 μm. Considerable aggregate formation is also observed, which may be due to the formation of secondary nucleation sites on already nucleated and growing nanosheets. These results confirm that, in principle, a direct, bottom-up synthesis can lead to the formation of high-aspect ratio MOF nanosheets.

To avoid aggregation and obtain high quality dispersible nanosheets, we hypothesized that it is important to control MOF nucleation by controlling the sequence and rate of addition of metal and linker solutions when forming the synthesis solution. We also decided to investigate the type of mixing used during synthesis, i.e., magnetic stirring versus gentle shaking using a shaker, anticipating that the later would better preserve the growing nanosheets from fragmentation. As seen from **Figure 4-2b**, addition of the metal to the linker solution dropwise under stirring results in well-faceted nanosheets with sharp edges that also exhibit smaller average lateral sizes and less aggregation than the sheets prepared from a standing solution. Moreover, the addition sequence was found to be important. For example, addition of metal to linker solution resulted in nanosheets with larger lateral

dimensions (**Figure 4-3a**) than those made by addition of linker to metal solution (**Figure 4-3b**). While the type of mixing used (magnetic stirring versus shaking) did not have a significant effect on the lateral size and quality of the nanosheets, we decided to use mixing using a shaker in our syntheses.

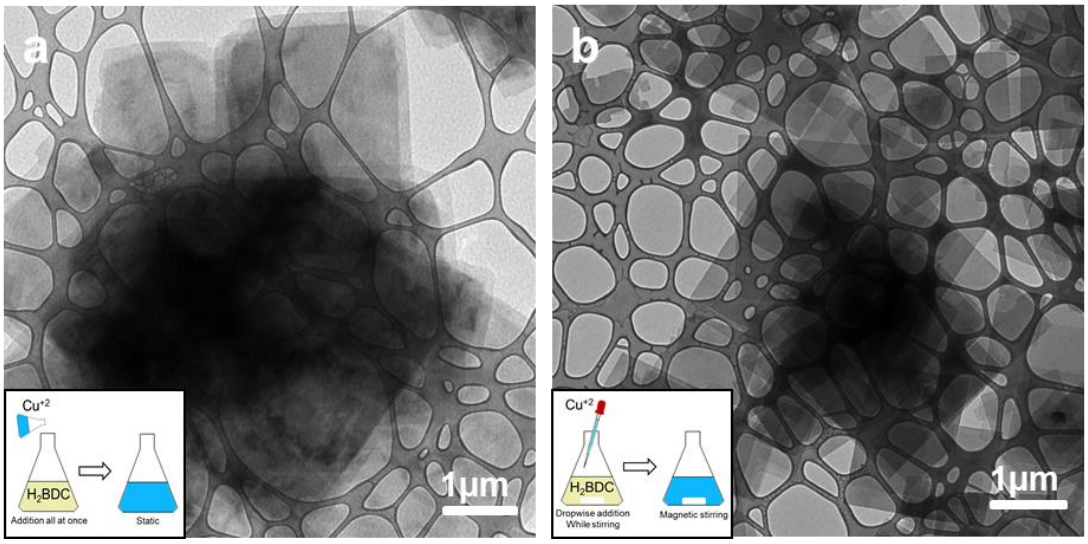

Figure 4-2: (a) Cu(BDC) nanosheets obtained by direct bottom up synthesis consisting of adding metal solution to linker solution all at once followed by keeping the synthesis solution static (no mixing) at 25° C for 24 h. Nanosheets with average lateral dimensions of 3.3 ± 1.5 µm were obtained. (Inset: synthesis schematic) (b) Cu(BDC) nanosheets obtained by direct bottom up synthesis consisting of adding metal solution to the linker solution dropwise under magnetic stirring, followed by crystallization at 25° C for 24 h using magnetic stirring. Nanosheets with average lateral dimensions of 1.6 ± 0.6 µm were obtained. (Inset: synthesis schematic).

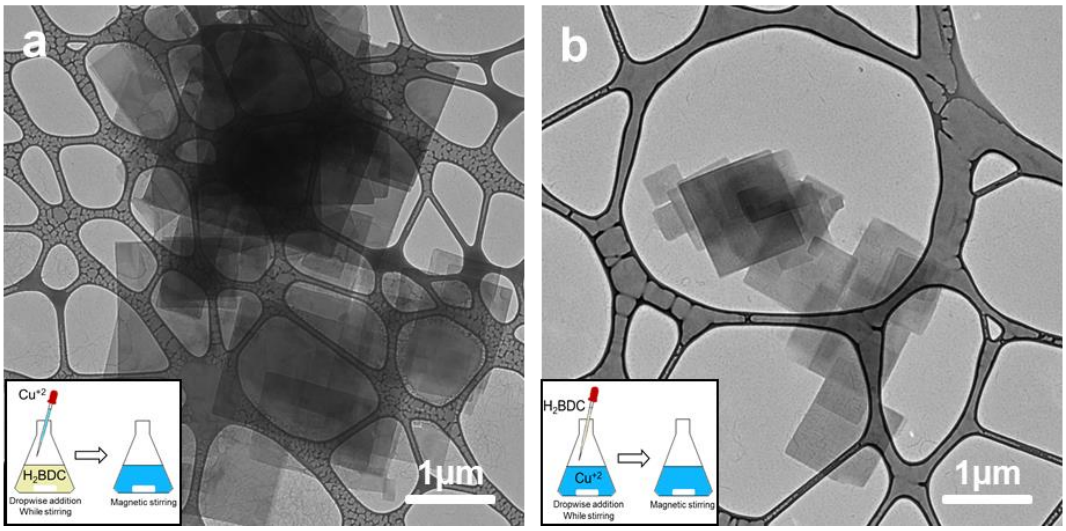

Figure 4-3: (a) Cu(BDC) nanosheets obtained by direct bottom up synthesis consisting of adding metal solution to linker solution under magnetic stirring followed by crystallization under magnetic stirring at 25° C for 24 h. Nanosheets with average lateral dimensions of 1.8 ± 0.7 µm were obtained. (Inset: synthesis schematic) (b) Cu(BDC) nanosheets obtained by direct bottom up synthesis consisting of adding linker solution to the metal solution under magnetic stirring followed by crystallization in a shaker at 25° C for 24 h. Nanosheets with average lateral dimensions of 0.9 ± 0.2 µm were obtained. (Inset: synthesis schematic). Addition sequence of the metal and linker solutions is important; adding metal solution to linker solution results in sheets with larger lateral dimensions.

Based on the screening experiments briefly described above, we adopted a direct synthesis scheme (described in Section 4.3.2.2) where metal solution is added dropwise to the linker solution over several minutes under magnetic stirring and the resulting synthesis solution is then gently shaken in an orbital shaker at the desired temperature and for the required duration (**Figure 4-4a**). Figures **4-4b** and **4-4c** show TEM and SEM images of Cu(BDC) nanosheets synthesized at 15° C using this method. The average sheet thickness was found to be 25 nm by AFM analysis (**Figure 4-4d**).

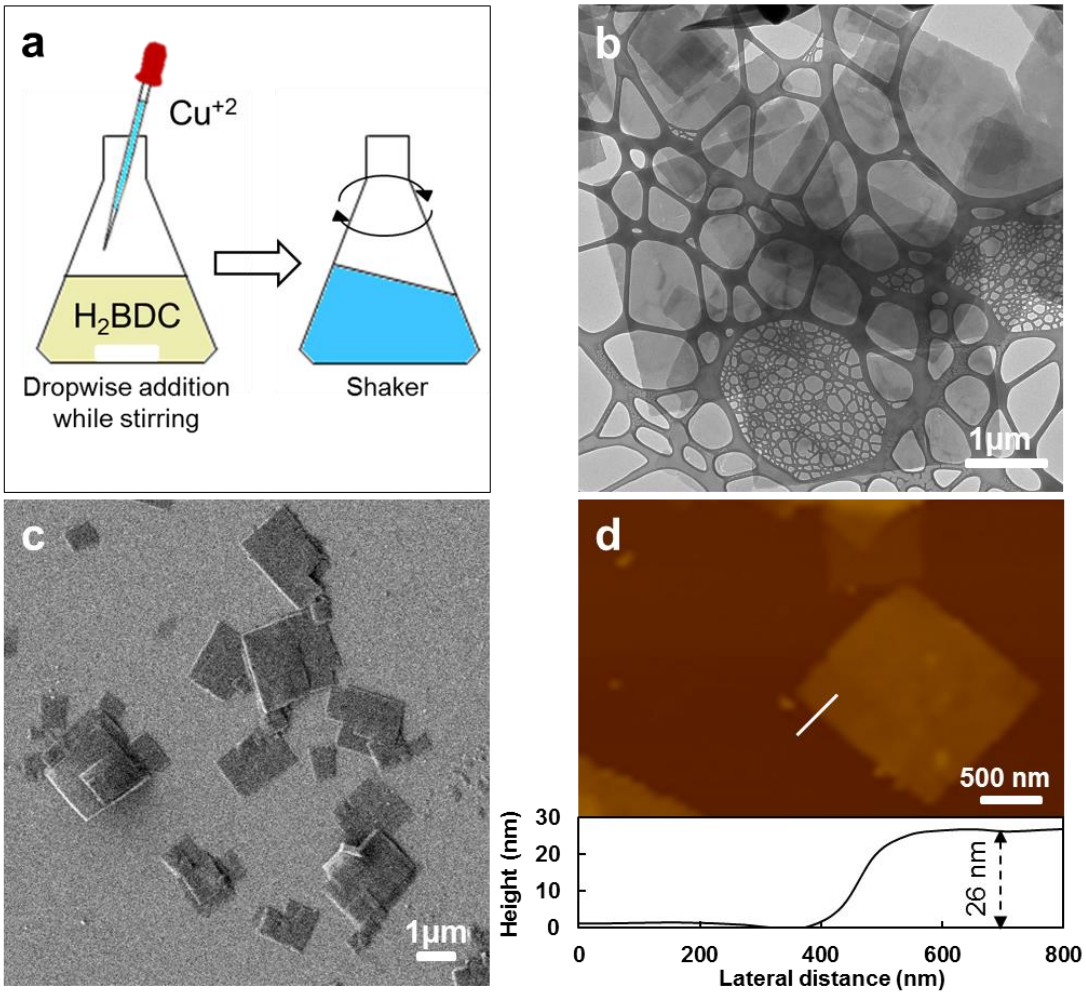

Figure 4-4: Direct synthesis of Cu(BDC) nanosheets performed in a shaker at 15° C for 24 h (synthesis solution was prepared by dropwise addition of Cu^{+2} solution to BDC linker solution under magnetic stirring): (a) Schematic of synthesis procedure, (b) TEM, (c) SEM, and (d) AFM images indicating that the basal dimensions are > 1 µm and the typical thickness is 25 nm.

Figure 4-5 shows the effect of synthesis temperature on the lateral size (measured along the edge of the nanosheet) and thickness of Cu(BDC) nanosheets. We found that lower temperatures favor thinner and larger sheets (**Figures 4-5g and 4-5h**), and a ten-fold increase in aspect ratio (average lateral dimension/thickness) could be achieved by lowering the synthesis temperature from 40° C to 15° C (**Figure 4-4i**). The lateral size

distribution of nanosheets synthesized at different temperatures is quantified in **Figure 4-6**, revealing that 85% of the sheets synthesized at 15° C exhibit lateral sizes between 1-4 µm.

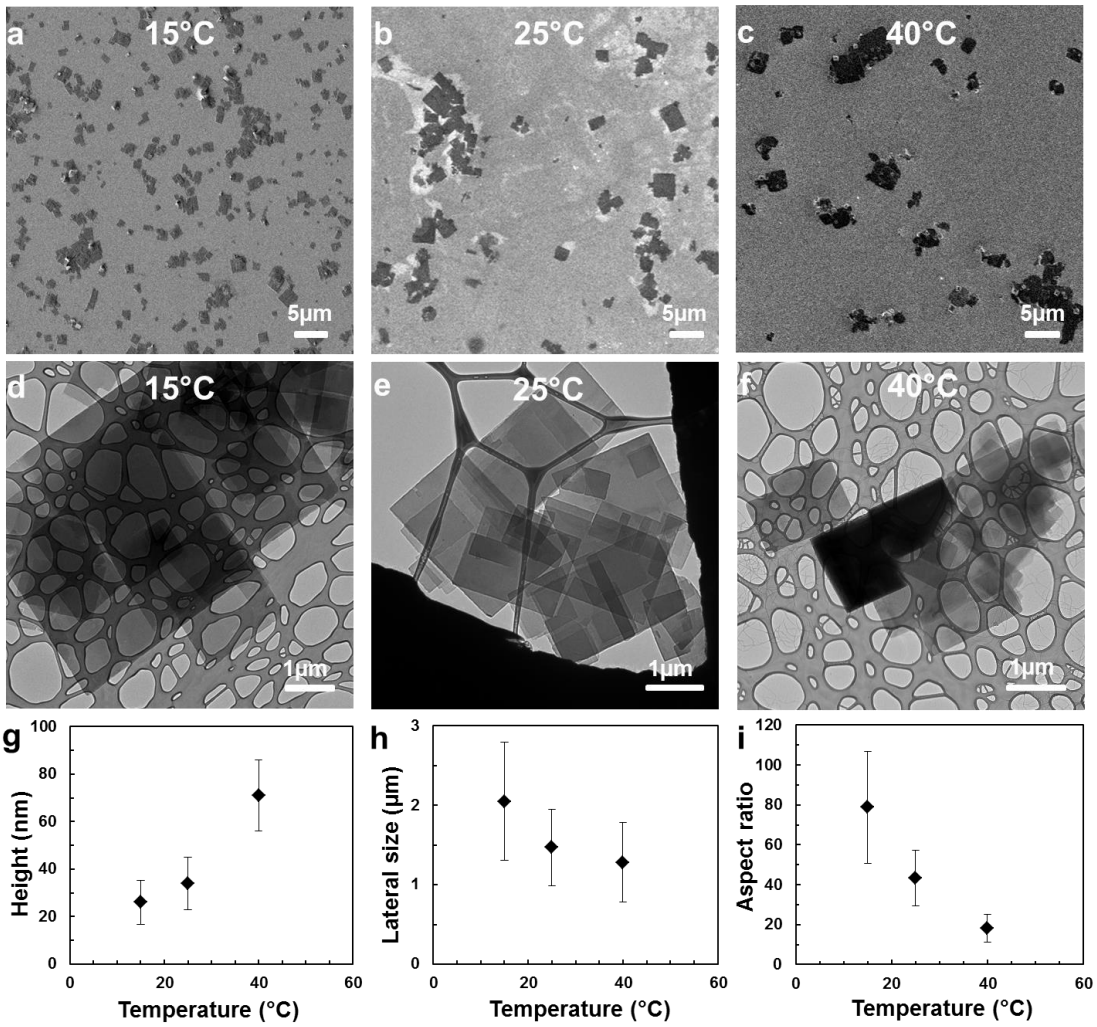

Figure 4-5: Effect of temperature on the direct synthesis of Cu(BDC) nanosheets. Low magnification SEM images of nanosheets obtained by direct synthesis at 15° C, 25° C and 40° C are shown in (a), (b), and (c), respectively. TEM images of nanosheets obtained by direct synthesis at 15° C, 25° C and 40° C, are shown in (d), (e), and (f), respectively. Plots of Cu(BDC) nanosheet thickness (g), lateral size (h), and aspect ratio (i) as a function of synthesis temperature.

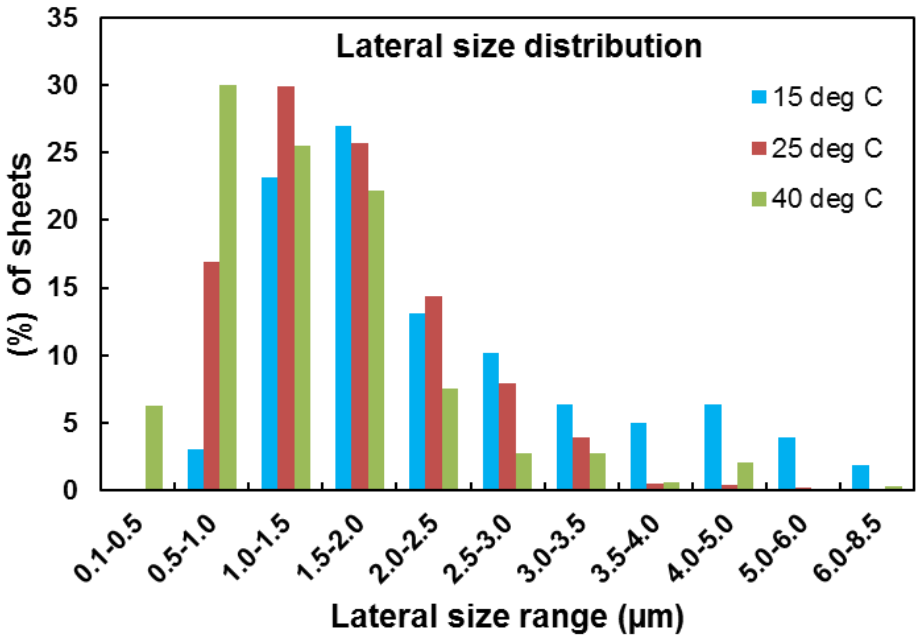

Figure 4-6: Lateral size distribution of Cu(BDC) nanosheets obtained by direct synthesis consisting of adding metal solution to linker solution under magnetic stirring followed by crystallization in a shaker for 24 h at different temperatures. At 15° C, 85% of the sheets have lateral size ranging from 1-4 µm; at 25° C and 40° C, 85% of the sheets have lateral size ranging from 0.5-2.5 µm.

4.4.2 Structure Characterization

Nanosheets obtained from direct synthesis at 15° C were washed in DMF and the as-synthesized, dried powder was characterized using synchrotron powder X-Ray diffraction. The X-ray diffraction pattern from the as-synthesized nanosheets matches well with the reported structure for solvated Cu(BDC)[126], wherein DMF solvent molecules are coordinated to the metal centers (**Figure 4-7a**).

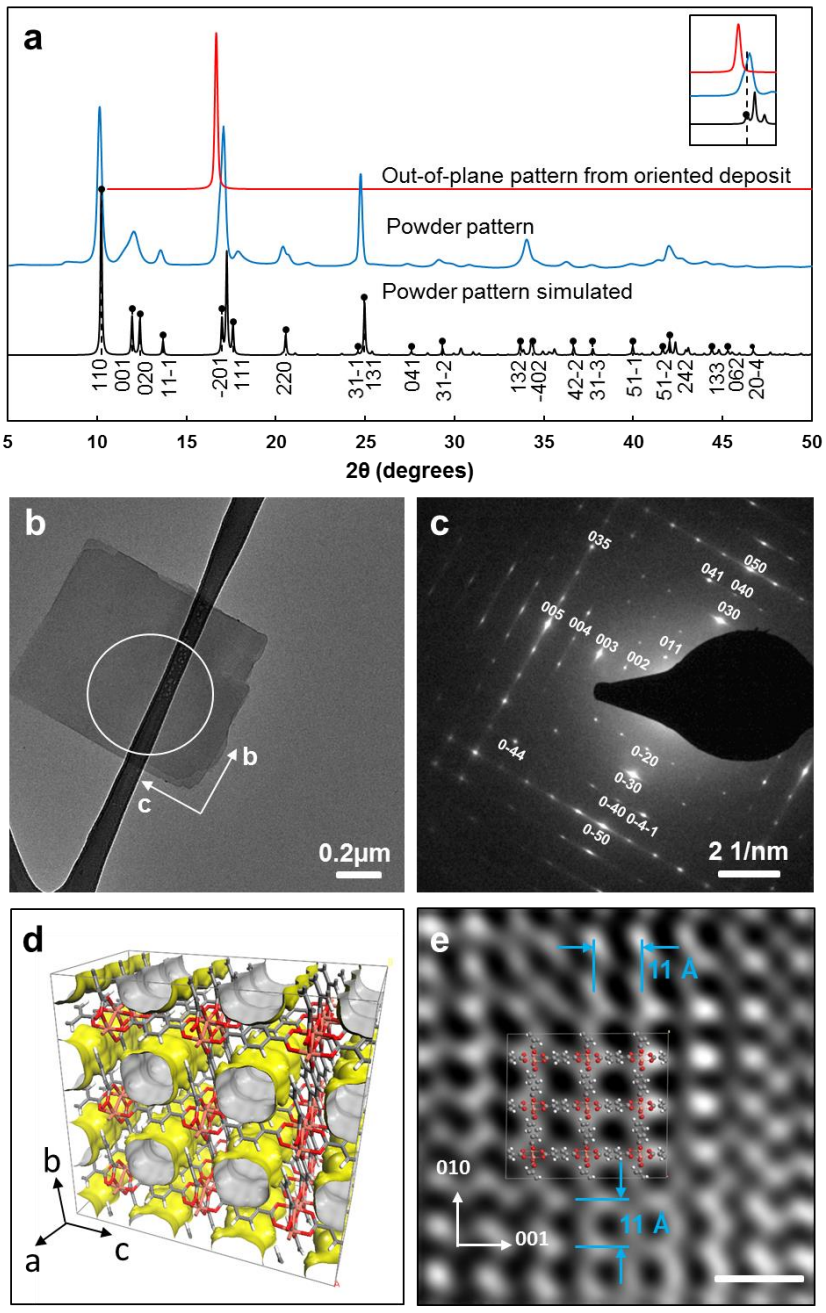

Figure 4-7:(a) XRD characterization of as-synthesized (DMF solvated) Cu(BDC) nanosheets; the black trace is the simulated pattern for the reported solvated structure of Cu(BDC) (monoclinic, space group = C2/*m*; *a* = 11.41 Å, *b* = 14.27 Å, *c* = 7.78 Å, β = 108.12°), the blue trace is the experimental powder pattern, and the red trace is the experimental out-of-plane pattern obtained from oriented Cu(BDC) nanosheets coating on a

porous support; the inset shows magnified region for the ($\bar{2}$01) peak. (b) TEM image of de-solvated (chloroform washed) Cu(BDC) nanosheets. (c) Selected area electron diffraction pattern obtained from the circled region of nanosheet in (b). (d) Schematic of the Cu(BDC) structure highlighting channels running down the *a*-axis. (e) Bragg filtered ADF-STEM image of Cu(BDC) nanosheet and superimposition of structure model indicating pores down *a*-axis. (Scale bar: 2 nm)

We further used out-of-plane X-ray diffraction to confirm the crystallographic direction perpendicular to the basal plane of the nanosheets. Samples were prepared by drop casting a suspension of Cu(BDC) nanosheets in DMF onto a porous ceramic support. A comparison of the nanosheet out-of-plane X-ray diffraction pattern (**Figure 4-7a**, red trace) with the nanosheet powder pattern confirms that the solvated nanosheets are oriented in the ($\bar{2}$01) direction, as previously reported[44,126]. As seen from the inset in **Figure 4-7a**, the *d*-spacing for the ($\bar{2}$01) peak obtained from the out-of-plane pattern (5.31 Å) is ~2 % larger than the simulated powder pattern (5.21 Å), whereas the value obtained from the experimental powder pattern (5.18 Å) is very close to the simulated value. This finding indicates that the crystal structure of the Cu(BDC) nanosheets can be affected by processing steps, including attachment to a substrate.

To facilitate incorporation of the Cu(BDC) nanosheets into polymer solutions, the nanosheet suspension in DMF requires exchanging the solvent to chloroform ($CHCl_3$) by repeated centrifugation, and it is therefore important to characterize the nanosheets dispersed in $CHCl_3$. Such characterization has not been previously reported for Cu(BDC) nanosheets and was performed here using TEM (**Figures 4-7b and 4-8**).

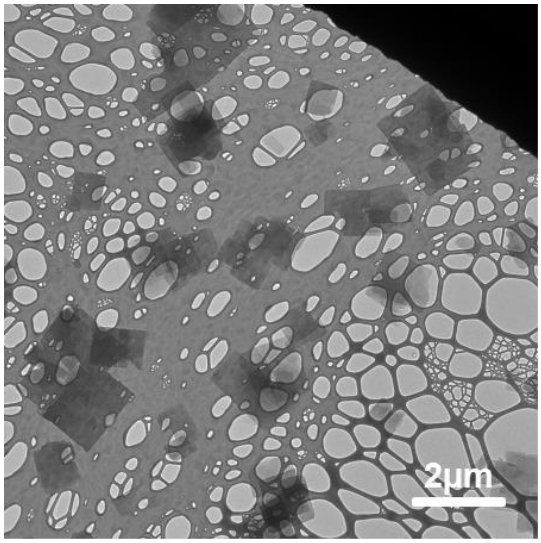

Figure 4-8: TEM image of Cu(BDC) nanosheets dispersed in chloroform.

The selected area electron diffraction (SAED) pattern obtained from the nanosheet imaged in **Figure 4-7b** is shown in **Figure 4-7c**. To index the diffraction spots and identify the basal plane orientation, we compared the experimental pattern to simulated electron diffraction patterns for different orientations of the reported structures for Cu(BDC). Qualitatively, a best match was found with the simulated electron diffraction pattern down the *a*-axis of the reported de-solvated structure[127] (**Figure 4-9**). Thus, the diffraction spots were indexed as (0 *k l*). Interestingly, a tetragonal projection is evident indicating that the ratio of *d*-spacings in the *b* and *c* directions is near one.

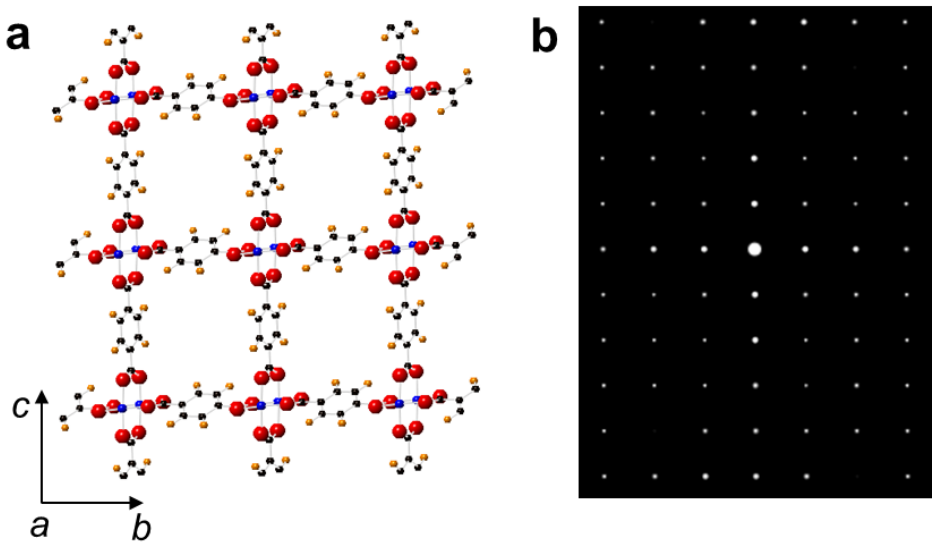

Figure 4-9: (a) Schematic of the de-solvated structure of Cu(BDC) down the *a*-axis. (b) Simulated electron diffraction pattern down the *a*-axis qualitatively matches the experimental selected area electron diffraction pattern (SAED) shown in Figure 3c in the main text.

To complement the SAED analysis of solvent-exchanged nanosheets, we also characterized their oriented coating on a porous support using in-plane X-ray diffraction. The in-plane diffraction pattern and the rotationally averaged selected area electron diffraction (RED) pattern are in good agreement with each other and show peaks that mainly correspond to the (0 *k l*) planes of the de-solvated structure for Cu(BDC) (**Figure 4-10**). Moreover, the in-plane X-ray data are in agreement with the tetragonal projection observed from the electron diffraction pattern, indicating that the length of *b* and *c* axes for the Cu(BDC) nanosheets are equal after solvent-exchange in $CHCl_3$. These results point to a structure model (**Figure 4-7d**) with a *b*-*c* orientation of the basal plane and pores running down the thin dimension, which is the crystallographic *a* axis. These pores should be deformed compared to those in the nominal crystal structure[127,128], which indicates differences in *b* and *c* axis dimensions.

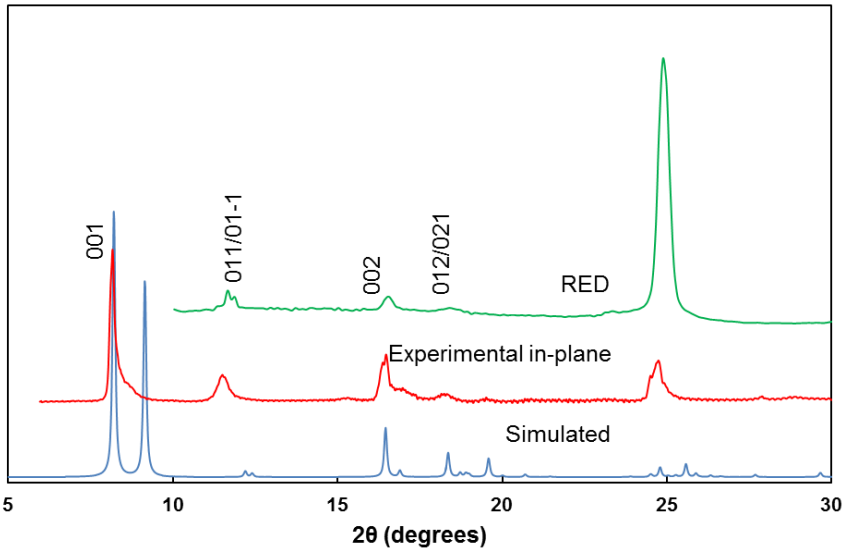

Figure 4-10: XRD patterns of Cu(BDC) nanosheets obtained by direct synthesis and subsequently solvent-exchanged in chloroform. Blue trace is the simulated pattern for the reported de-solvated structure of Cu(BDC) (Triclinic, space group = P-1; *a* = 5.25 Å, *b* = 9.67 Å, *c* = 10.77 Å, α = 90.29°, β = 91.06°, γ = 92.41°); red trace is the experimental in-plane pattern obtained from nanosheets that were deposited on a porous support, with most of them having an orientation such that their basal plane is parallel to the support surface. The green trace is the rotationally averaged electron diffraction (RED) pattern. In-plane and RED patterns show peaks dominated by the (*0 k l*) family of planes, which are in agreement with the tetragonal projection observed in the electron diffraction pattern.

To confirm that the de-solvated Cu(BDC) exhibits a distorted nearly tetragonal structure, we utilized high-resolution transmission electron microscopy. Indeed, Bragg-filtered ADF-STEM imaging (**Figure 4-7e**) obtained along the direction perpendicular to the nanosheet (*a* axis) confirms the presence of pores and shows that the planar distances along the *b* and *c* directions are almost equal, with a *d*-spacing of ~1.1 nm. A Bragg filtered ADF-STEM image over a large region of de-solvated Cu(BDC) nanosheet (**Figure 4-11a**) shows the presence of wavy features along the *b* and *c* axes, which are indicative of structural

disorder. Correspondingly, the spots obtained from Fast Fourier Transform (FFT, **Figure 4-11b**) are streaked and so appear to correlate with the peaks exhibiting tails in the in-plane X-ray diffraction pattern (**Figure 4-10**, red trace). The foregoing results confirm a degree of disorder present in the de-solvated structure that has not been identified in earlier studies, and the role of structural disorder in the adsorption and diffusion properties of Cu(BDC) nanosheets is not yet known.

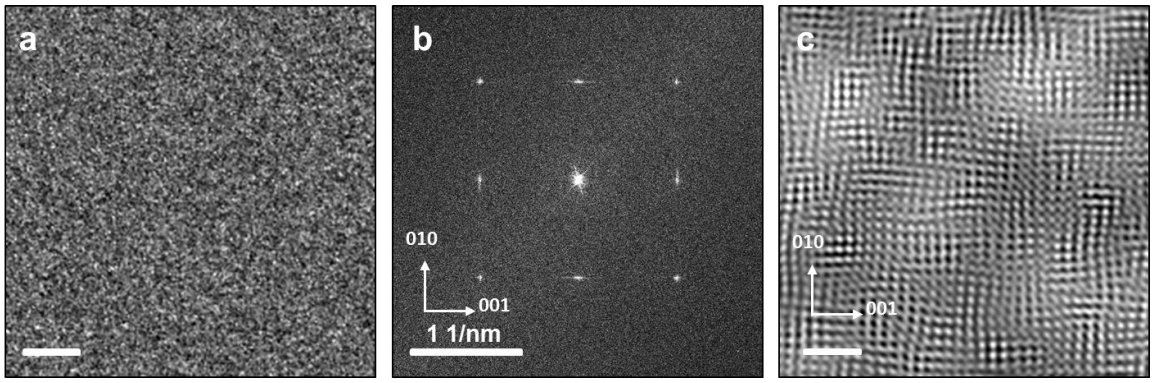

Figure 4-11: (a) Unprocessed ADF-STEM image (Scale bar: 5nm) and (b) its corresponding Fast Fourier Transform (FFT) of de-solvated Cu(BDC) nanosheets as viewed down the *a*-axis. FFT of the image in (a) indicates disorder by the streaking of the spots observed. (c) Bragg filtered ADF-STEM image of Cu(BDC) nanosheets generated from the unprocessed image by masking the FFT spots. Wavy features along the *b*- and *c*- axes indicate flexibility and disorder in the structure. (Scale bar: 5nm)

4.4.3 Membrane Performance

Mixed-matrix membranes were fabricated by incorporating Cu(BDC) nanosheets in Matrimid (as detailed in section 4.3.4). Nanosheets suspended in chloroform were first mixed with Matrimid to obtain the desired MOF loadings (4, 8, and 12 wt%), and the MMMs were then obtained by solution casting. Single gas (CO_2, N_2) and mixed gas (CO_2/CH_4) measurements were conducted at different feed pressures to test the performance of the MMMs.

At 8 wt% loading of the MOF nanosheets, the ideal selectivity for CO_2/N_2 shows a 70 % increase over the pure polymer (**Figure 4-12a**), while the MMM CO_2 and N_2 permeabilities are smaller than those of the neat polymer (**Figures 4-12b and 4-12c**). For example, the CO_2 and N_2 permeabilities were observed to decrease by ~50 % and ~70 %, respectively, for the 8 wt % MMM relative to the pure polymer at 4 bar (**Figures 4-12b and 4-12c**).

The MMMs notably exhibit selectivity for mixed gas feeds at high pressures (**Figure 4-13a-c**). For example, at 12 wt % loading mixed gas measurements show a 70 % increase in CO_2/CH_4 selectivity even at 20 bar feed pressure (**Figure 4-13a**). Taken together, these results agree very well with those reported in the literature[44]. Indeed, Rodenas et al. reported a 60 % increase for the mixed gas CO_2/CH_4 selectivity at 7.5 bar feed pressure and 8 wt% loading of Cu(BDC) nanosheets in Matrimid. This demonstrates that the directly synthesized Cu(BDC) nanosheets behave similarly with the nanosheets synthesized in Ref. 44, in spite of possible differences due to the structural disorder discussed in section 4.4.2.

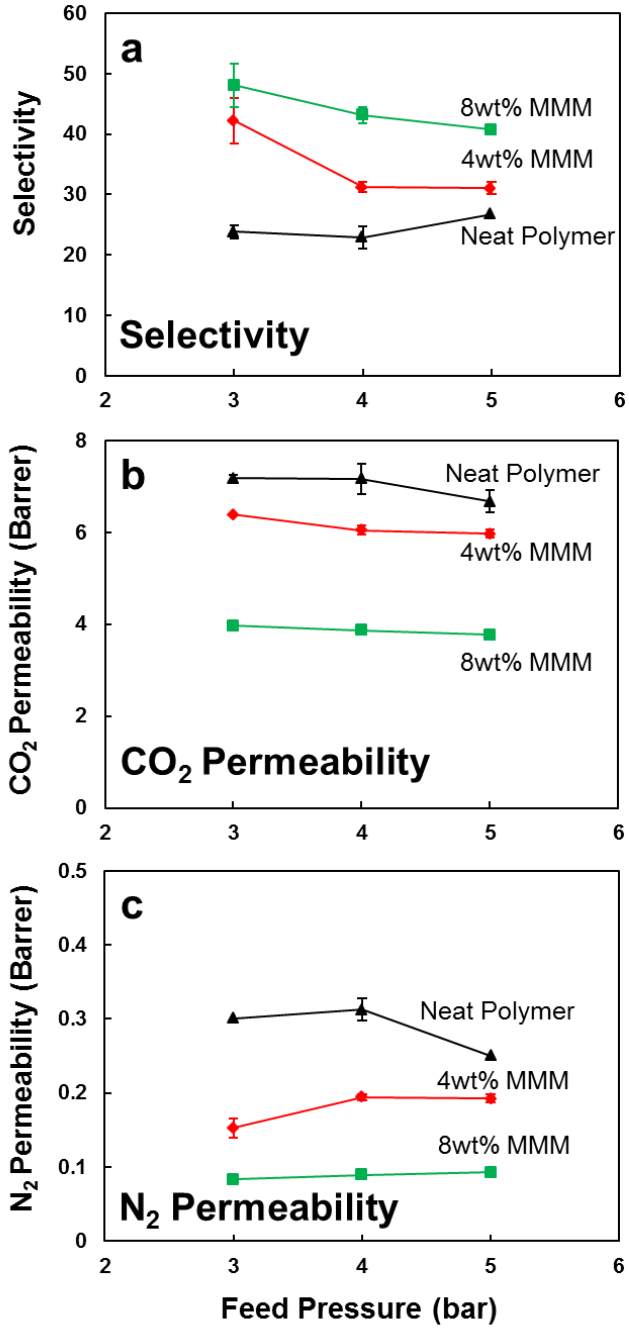

Figure 4-12: Single gas CO_2 and N_2 permeation data for Matrimid and mixed matrix membranes incorporating 4 and 8 wt% de-solvated Cu(BDC) nanosheets in Matrimid, showing (a) Ideal selectivity, (b) CO_2 permeability, and (c) N_2 permeability versus feed pressure.

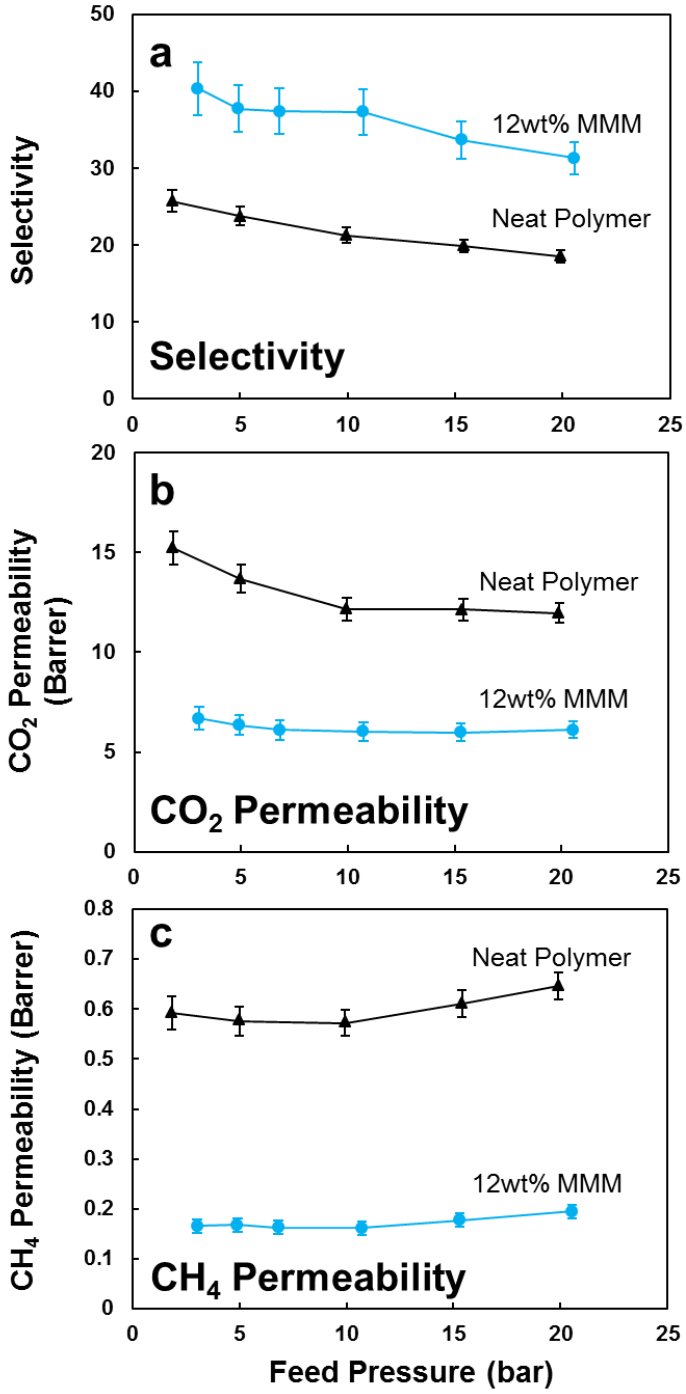

Figure 4-13: Mixed gas permeation data from an equimolar CO_2/CH_4 feed for pure Matrimid and a mixed matrix membrane incorporating 12 wt% de-solvated Cu(BDC) nanosheets in Matrimid, showing (a) CO_2/CH_4 Selectivity, (b) CO_2 permeability, and (c) CH_4 permeability versus feed pressure.

However, we should note two differences between the results presented here and those in **Ref. 44**. First, the selectivity for neat Matrimid reported in **Ref. 44** is ~58, which is much higher than the selectivity value of 24 determined here and more commonly reported for Matrimid in the literature[43,129,130]. These differences could arise due to differences in film fabrication methodology. For example, casting technique, casting solvents, concentration of polymer solution used and film annealing temperature etc. are some of the parameters that can affect the transport properties of polymer films[131]. Second, Rodenas et al. observe an increasing trend in mixed-matrix membrane selectivity as a function of feed pressure, whereas our results show a decreasing trend in selectivity as a function of feed pressure (**Figure 4-13a**).

In a recent study, Yang et al.[132] incorporated Cu(BDC) nanosheets into high permeability polymers such as 6FDA-DAM and PIM-1. They reported a 40 % increase in mixed gas CO_2/CH_4 selectivity at 1 bar feed pressure and 4 wt% loading of Cu(BDC) nanosheets in 6FDA-DAM. Considering our permeation results for Matrimid-based MMMs and the previous reports from Rodenas et al. and Yang et al., we notice that a similar improvement in selectivity is observed by incorporating Cu(BDC) nanosheets in polymers that have CO_2 permeabilities that differ by two orders of magnitude. Given that performance of MMMs depends critically on a good match between the permeability of the polymer matrix and the incorporated nanosheets (selective flake), the following two questions arise. What are the effective permeabilities for Cu(BDC) nanosheets? What are possible polymers that would, in theory, result in a maximum improvement in selectivity?

4.4.4 Analysis of Membrane Performance

To address these questions, we resorted to mathematical models that describe transport in MMMs[118,133,134]. The modified Cussler model[133] is one such model that describes two-dimensional transport across an oriented staggered array of flakes with an aspect ratio, α, dispersed in a polymer matrix at a volume fraction ϕ (Eq. 2).

$$P_i^C = P_i^M * \frac{1}{(1-\phi) + \frac{1}{\left[\left(\frac{1}{\phi}\right)\left(\frac{P_i^F}{P_i^M}\right) + \left(\frac{1-\phi}{\alpha^2\phi^2}\right)\right]}} \qquad (2)$$

In this equation, P_i^C is the permeability of component *i* in the mixed matrix membrane (composite); P_i^M is the permeability of component *i* in polymer matrix; and P_i^F is the permeability of component *i* in the flake (incorporated nanosheet). The model assumes idealized flakes that are regularly spaced and dispersed uniformly in the continuous polymer matrix. Also, the matrix and flake permeabilities are assumed to be constant (concentration independent). Equation 2 has been shown to describe well permeation in selective-flake MMMs when the volume fraction is low and the aspect ratio high, as is the case with the MMMs studied here.

Using our permeation results at the 4 and 8 wt % loadings and given an average Cu(BDC) nanosheet aspect ratio of 80, Eq. 1 is used to determine flake permeability for CO_2 and N_2. Flake permeability values obtained for CO_2 are in the range of 0.7-1.9 Barrer and those for N_2 are in the range of 0.009-0.012 Barrer. It is worth noting that the flake permeabilities calculated here based on the permeation data from the MMMs are effective values and could be influenced by the structure of the MMMs and their fabrication history. As

discussed in section 4.4.3, effective flake permeability lower than the matrix permeability accounts for the observed reduction in permeability upon incorporation of Cu(BDC) nanosheets in the polymer matrix.

Flake selectivities in the range of 80-160 are estimated from the effective permeability values. Given that the adsorptive selectivity of the thermally de-solvated Cu(BDC) nanosheets for CO_2 over N_2 is in the range of 3-5[44,127], using Eq. 3,

$$\frac{P_i^F}{P_j^F} = \frac{D_i^F}{D_j^F} \times \frac{S_i^F}{S_j^F} \qquad (3)$$

where *D* is the diffusivity and *S* is the solubility, one would obtain a diffusive selectivity value for the Cu(BDC) flakes in the range of 20-50. It will be interesting if follow up studies can confirm such high diffusion selectivity for CO_2 over N_2. If indeed the Cu(BDC) nanosheets have the model-estimated permeabilities, then by appropriate selection of a polymer matrix, MMMs with even better performance can be obtained. For example, if the polymer matrix is selected to be 6FDA-DAT with CO_2 and N_2 permeabilities of 56 and 1.12 Barrer, respectively, then a 8 wt % MMM should theoretically exhibit CO_2 and N_2 permeance values of 16.23 and 0.17 Barrer, giving a selectivity of 98. However, as discussed below, it appears that there are inconsistencies with other reported MMM data, indicating that other factors such as the polymer matrix-Cu(BDC) interface may contribute to the observed permeances and selectivities.

We used the flake permeabilities obtained from our permeation data at 4 wt % loading of Cu(BDC) nanosheets in Matrimid to predict the performance of the 4 wt % Cu(BDC) based

MMMs reported in Refs. 44 and 132 (**Table 4-1**). The neat polymer selectivity values used for making the predictions are reported in the first column of **Table 4-1**.

	Selectivity			Permeability of CO_2 (Barrer)		
	Neat Polymer	4wt% Cu(BDC) MMM		Neat Polymer	4wt% Cu(BDC) MMM	
	Experimental	Experimental	Model Prediction	Experimental	Experimental	Model Prediction
Matrimid (Ref. 44)	58	68	70	5.78	4.74	5.3
Matrimid (This Work)	24	42	42	7.2	6.4	6.4
6FDA-DAM (Ref. 132)	30	43	48	590	430	73.7
PIM-1 (Ref. 132)	17	22	20	3100	2300	241.9

Table 4-1: Comparison of permeation results for 4 wt% Cu(BDC)-based MMMs in the literature. The model predictions were obtained using the modified Cussler equation as described in section 3.4. Flake permeabilities (PCO_2 = 1.92; PN_2 = 0.012) were determined from MMM (4 wt% Cu(BDC) in Matrimid matrix) permeation results and then used along with the corresponding matrix permeabilities to calculate the model predictions for MMM performance.

We see that the selectivities predicted from the modified Cussler equation (column three in **Table 4-1**) agree very well with the experimental values (column two). Also, the model predictions for CO_2 permeability for Matrimid-based MMMs (Ref. 44 and this work, column six) agree very well with the experimental data (column five). However, the model predictions for CO_2 permeability for 6FDA-DAM and PIM-1 MMMs are much lower than the values reported in Ref. 132. One possible explanation for the experimental results of Ref. 132 is that incorporation of Cu(BDC) nanosheets in 6FDA-DAM and PIM-1 leads to the formation of non-selective void space around the nanosheets through which the gases

can bypass, leading to the measured high permeabilities of CO_2 and CH_4[135,136]. However, this explanation cannot account for the observed selectivity improvements in the MMMs (43% for 6FDA-DAM MMM and 19 % for PIM-1), unless it is accompanied with a modification of the polymer matrix induced by the nanosheets and/or processing conditions.

4.5 Conclusions

Using direct syntheses carried out at 15° C, we obtained Cu(BDC) nanosheets with aspect ratios as high as 100 (average lateral size 2.5 µm and thickness of 25 nm). Dropwise addition of the metal to the linker solution under magnetic stirring followed by gentle mixing of the synthesis solution in a shaker resulted in high quality, dispersible nanosheets. It was found that reducing the synthesis temperature from 40° C to 15° C results in a ten-fold increase in the aspect ratio of Cu(BDC) nanosheets.

Solvent exchanging of the DMF-soaked sheets with $CHCl_3$ resulted in desolvation, and the de-solvated nanosheets were characterized in detail for the first time using high-resolution TEM imaging and electron and X-ray diffraction. When compared to the nominal crystal structure reported previously, the de-solvated nanosheets show presence of structural disorder.

Incorporation of de-solvated Cu(BDC) nanosheets in Matrimid led to a maximum 70 % increase in the CO_2/CH_4 mixture separation factor at 12 wt % loading and 20 bar pressure for a 50:50 CO_2:CH_4 feed. A CO_2 permeability of 6.1 Barrer was observed for the 12 wt % loaded MMM, as compared to a CO_2 permeability of 12 Barrer for Matrimid. Using the experimental permeation results obtained in this work with a mathematical model for

transport in mixed matrix membranes, the effective permeabilities of Cu(BDC) nanosheets were estimated and further used to predict the performance of Cu(BDC)-based mixed matrix membranes reported in the literature. Certain of the experimental permeability values reported are much higher than those predicted using the model, indicating the presence of defects at the matrix-flake interface. If one can avoid these defects while fabricating MMMs, a four-fold improvement in the selectivity should be achievable at 8 wt % loading of Cu(BDC) nanosheets in a polymer matrix that has a CO_2 permeability of around 60 Barrer.

Concluding Remarks

In conclusion, this dissertation discusses the development of synthetic tools to tailor the microstructure of 2D molecular sieve zeolite and MOF materials to optimize their performance with a focus on thin film applications.

A novel Langmuir trough coating technique was applied to isolate 2D MFI zeolite nanosheets and form monolayer coatings on versatile supports such as Si wafers. Monolayers of zeolite nanosheets open avenues for investigating the fundamental growth, adsorption, dielectric and transport properties of 2D zeolites.

Using the monolayer coatings as a prototype, growth conditions were developed that enabled unprecedented nanometer control of zeolite MFI growth at a scale approaching single-unit-cell dimensions. The slow and controllable growth conditions allowed us to precisely tailor the microstructure of MFI thin films and hierarchical catalysts. Zeolite MFI film having one of the lowest reported dielectric constant was fabricated using these growth conditions. Furthermore, it was demonstrated that these growth conditions are robust enough and can be transferred for nanoscale growth control of MFI crystals with varied morphologies supported on versatile substrates such as Si wafers, gold coated Si wafers, porous silica supports etc.

A scalable and direct synthesis for Cu(BDC) MOF nanosheets was developed and it was demonstrated that, in principle, simple, bottom-up synthesis conditions can be employed for obtaining nanosheets of MOF materials that exhibit an inherent growth anisotropy. A detailed structure characterization of Cu(BDC) MOF nanosheets was undertaken using X-Ray diffraction and electron microscopy. Such a characterization revealed presence of structural disorder prevalent in the Cu(BDC) MOF nanosheets that could potentially affect

their adsorption and diffusion properties. Hybrid nanocomposites were fabricated by incorporating Cu(BDC) MOF nanosheets in Matrimid polymer matrices that exhibited significant improvement in CO_2/CH_4 selectivity even under conditions of mixed gas and high feed pressures.

Future work can focus on incorporating Cu(BDC) nanosheets in high free volume polymer matrices such as PTMSP and 6FDA-Durene. Analysis of the single gas and mixed gas permeation data using modified Cussler's model for selective flake composites could reveal the effect Cu(BDC) nanosheets have on the microstructure of these polymer matrices. Furthermore, according to model predictions reported in Chapter 4, it is predicted that a polymer matrix having a CO_2 permeability of around 70-80 Barrer would give rise to a maximum increase in the selectivity of the mixed matrix membranes under ideal matrix/flake interface conditions. Two of the potential polymers that could be experimented with are the 6FDA-DAT and the poly (2,6-dimethyl-1,4-phenylene oxide). Some of the challenges in practical realization of the model predictions are defects at the matrix/flake interface such as a void creating a sieve-in-a-cage configuration or rigidification of the polymer around the flake. If one can successfully overcome these challenges, mixed matrix membranes based on Cu(BDC) nanosheets could result in a 4-fold improvement in the selectivity of CO_2/CH_4 over that of the neat polymer.

Bibliography

(1) Agrawal, R.; Singh, N. R.; Ribeiro, F. H.; Delgass, W. N. Sustainable Fuel for the Transportation Sector. *Proc. Natl. Acad. Sci.* **2007**, *104* (12), 4828–4833.

(2) Jain, A.; Ong, S. P.; Hautier, G.; Chen, W.; Richards, W. D.; Dacek, S.; Cholia, S.; Gunter, D.; Skinner, D.; Ceder, G.; et al. Commentary: The Materials Project: A Materials Genome Approach to Accelerating Materials Innovation. *APL Mater.* **2013**, *1* (1), 011002-1-011002-11.

(3) Furukawa, H.; Yaghi, O. M. Storage of Hydrogen, Methane, and Carbon Dioxide in Highly Porous Covalent Organic Frameworks for Clean Energy Applications. *J. Am. Chem. Soc.* **2009**, *131* (25), 8875–8883.

(4) Cortright, R. D.; Davda, R. R.; Dumesic, J. A. Hydrogen from Catalytic Reforming of Biomass-Derived Hydrocarbons in Liquid Water. *Nature* **2002**, *418* (6901), 964–967.

(5) Stöcker, M. Biofuels and Biomass-to-Liquid Fuels in the Biorefinery: Catalytic Conversion of Lignocellulosic Biomass Using Porous Materials. *Angew. Chem. Int. Ed. Engl.* **2008**, *47* (48), 9200–9211.

(6) Ragauskas, A. J.; Williams, C. K.; Davison, B. H.; Britovsek, G.; Cairney, J.; Eckert, C. A.; Frederick Jr., W. J.; Hallett, J. P.; Leak, D. J.; Liotta, C. L.; et al. The Path Forward for Biofuels and Biomaterials. *Science* **2006**, *311* (5760), 484–489.

(7) Gin, D. L.; Noble, R. D. Designing the Next Generation of Chemical Separation

Membranes. *Science* **2011**, *332*, 674–676.

(8) Tsapatsis, M. Toward High-Throughput Zeolite Membranes. *Science* **2011**, *334*, 767–768.

(9) Koros, W. J.; Zhang, C. Materials for Next-Generation Molecularly Selective Synthetic Membranes. *Nat. Mater.* **2017**, *16* (3), 289–297.

(10) Bae, Y. S.; Snurr, R. Q. Development and Evaluation of Porous Materials for Carbon Dioxide Separation and Capture. *Angew. Chem. Int. Ed. Engl.* **2011**, *50* (49), 11586–11596.

(11) D'Alessandro, D. M.; Smit, B.; Long, J. R. Carbon Dioxide Capture: Prospects for New Materials. *Angew. Chem. Int. Ed. Engl.* **2010**, *49* (35), 6058–6082.

(12) Wang, Q.; Luo, J.; Zhong, Z.; Borgna, A. CO_2 Capture by Solid Adsorbents and Their Applications: Current Status and New Trends. *Energy Environ. Sci.* **2011**, *4* (1), 42–55.

(13) Cundy, C. S.; Cox, P. A. The Hydrothermal Synthesis of Zeolites: History and Development from the Earliest Days to the Present Time. *Chem. Rev.* **2003**, *103* (3), 663–701.

(14) Corma, A. From Microporous to Mesoporous Molecular Sieve Materials and Their Use in Catalysis. *Chem. Rev.* **1997**, *97* (6), 2373–2420.

(15) http://www.iza-structure.org/databases.

(16) Yaghi, O. M.; O'Keeffe, M.; Ockwig, N. W.; Chae, H. K.; Eddaoudi, M.; Kim

Jaheon. Reticular Synthesis and the Design of New Materials. *Nature* **2003**, *423*, 705–712.

(17) Furukawa, H.; Cordova, K. E.; O'Keeffe, M.; Yaghi, O. M. The Chemistry and Applications of Metal-Organic Frameworks. *Science* **2013**, *341* (6149), 1230444-1-1230444–12.

(18) Blay, V.; Louis, B.; Miravalles, R.; Yokoi, T.; Peccatiello, K. A.; Clough, M.; Yilmaz, B. Engineering Zeolites for Catalytic Cracking to Light Olefins. *ACS Catal.* **2017**, *7*, 6542–6566.

(19) Tanabe, K.; Holderich, W. F. Industrial Application of Solid Acid–base Catalysts. *Appl. Catal. A Gen.* **1999**, *181* (2), 399–434.

(20) Huber, G. W.; Corma, A. Synergies between Bio- and Oil Refineries for the Production of Fuels from Biomass. *Angew. Chem. Int. Ed. Engl.* **2007**, *46* (38), 7184–7201.

(21) Lin, Y.-C.; Huber, G. W. The Critical Role of Heterogeneous Catalysis in Lignocellulosic Biomass Conversion. *Energy Environ. Sci.* **2009**, *2* (1), 68–80.

(22) Taarning, E.; Osmundsen, C. M.; Yang, X.; Voss, B.; Andersen, S. I.; Christensen, C. H. Zeolite-Catalyzed Biomass Conversion to Fuels and Chemicals. *Energy Environ. Sci.* **2011**, *4* (3), 793–804.

(23) Chang, C. D.; Silvestri, A. J. The Conversion of Methanol and Other O-Compounds to Hydrocarbons over Zeolite Catalysts. *J. Catal.* **1977**, *47*, 249–259.

(24) Chang, C.-C.; Green, S. K.; Williams, C. L.; Dauenhauer, P. J.; Fan, W. Ultra-

Selective Cycloaddition of Dimethylfuran for Renewable p-Xylene with H-BEA. *Green Chem.* **2014**, *16* (2), 585–588.

(25) Lai, Z.; Bonilla, G.; Diaz, I.; Nery, J. G.; Sujaoti, K.; Amat, M. A.; Kokkoli, E.; Terasaki, O.; Thompson, R. W.; Tsapatsis, M.; et al. Microstructural Optimization of a Zeolite Membrane for Organic Vapor Separation. *Science* **2003**, *300*, 456–460.

(26) Varoon, K.; Zhang, X.; Elyassi, B.; Brewer, D. D.; Gettel, M.; Kumar, S.; Lee, J. A.; Maheshwari, S.; Mittal, A.; Sung, C.-Y.; et al. Dispersible Exfoliated Zeolite Nanosheets and Their Application as a Selective Membrane. *Science* **2011**, *334* (6052), 72–75.

(27) Agrawal, K. V.; Topuz, B.; Pham, T. C. T.; Nguyen, T. H.; Sauer, N.; Rangnekar, N.; Zhang, H.; Narasimharao, K.; Basahel, S. N.; Francis, L. F.; et al. Oriented MFI Membranes by Gel-Less Secondary Growth of Sub-100 Nm MFI-Nanosheet Seed Layers. *Adv. Mater.* **2015**, *27* (21), 3243–3249.

(28) Jeon, M. Y.; Kim, D.; Kumar, P.; Lee, P. S.; Rangnekar, N.; Bai, P.; Shete, M.; Elyassi, B.; Lee, H. S.; Narasimharao, K.; et al. Ultra-Selective High-Flux Membranes from Directly Synthesized Zeolite Nanosheets. *Nature* **2017**, *543* (7647), 690–694.

(29) Elyassi, B.; Jeon, M. Y.; Tsapatsis, M.; Narasimharao, K.; Basahel, S. N.; Al-Thabaiti, S. Ethanol/Water Mixture Pervaporation Performance of b-Oriented Silicalite-1 Membranes Made by Gel-Free Secondary Growth. *AIChE J.* **2016**, *62* (504), 556–563.

(30) Tiriolo, R.; Rangnekar, N.; Zhang, H.; Shete, M.; Bai, P.; Nelson, J.; Karapetrova, E.; Macosko, C. W.; Siepmann, J. I.; Lamanna, E.; et al. Sub-Micrometer Zeolite Films on Gold-Coated Silicon Wafers with Single-Crystal-Like Dielectric Constant and Elastic Modulus. *Adv. Funct. Mater.* **2017**, *27* (25), 1–7.

(31) Lew, C. M.; Sun, M.; Liu, Y.; Wang, J.; Yan, Y. Pure-Silica-Zeolite Low-Dielectric Constant Materials. *Ordered Porous solids Recent Adv. Prospect.* **2009**, 335–364.

(32) Li, Z.; Johnson, M. C.; Sun, M.; Ryan, E. T.; Earl, D. J.; Maichen, W.; Martin, J. I.; Li, S.; Lew, C. M.; Wang, J.; et al. Mechanical and Dielectric Properties of Pure-Silica-Zeolite Low-k Materials. *Angew. Chem. Int. Ed. Engl.* **2006**, *45* (38), 6329–6332.

(33) Mintova, S.; Bein, T. Nanosized Zeolite Films for Vapor-Sensing Applications. *Microporous Mesoporous Mater.* **2001**, *50* (2–3), 159–166.

(34) Sahner, K.; Hagen, G.; Schönauer, D.; Reiß, S.; Moos, R. Zeolites - Versatile Materials for Gas Sensors. *Solid State Ionics* **2008**, *179* (40), 2416–2423.

(35) Mintova, S.; Mo, S.; Bein, T. Humidity Sensing with Ultrathin LTA-Type Molecular Sieve Films Grown on Piezoelectric Devices. *Chem. Mater.* **2001**, *13* (29), 901–905.

(36) Lee, J.; Farha, O. K.; Roberts, J.; Scheidt, K. A; Nguyen, S. T.; Hupp, J. T. Metal-Organic Framework Materials as Catalysts. *Chem. Soc. Rev.* **2009**, *38* (5), 1450–1459.

(37) García-García, P.; Müller, M.; Corma, A. MOF Catalysis in Relation to Their Homogeneous Counterparts and Conventional Solid Catalysts. *Chem. Sci.* **2014**, *5* (8), 2979–3007.

(38) McDonald, T. M.; Mason, J. A.; Kong, X.; Bloch, E. D.; Gygi, D.; Dani, A.; Crocellà, V.; Giordanino, F.; Odoh, S. O.; Drisdell, W. S.; et al. Cooperative Insertion of CO_2 in Diamine-Appended Metal-Organic Frameworks. *Nature* **2015**, *519* (7543), 303–308.

(39) Millward, A. R.; Yaghi, O. M. Metal-Organic Frameworks with Exceptionally High Capacity for Storage of Carbon Dioxide at Room Temperature. *J. Am. Chem. Soc.* **2005**, *127* (51), 17998–17999.

(40) Peng, Y.; Li, Y.; Ban, Y.; Jin, H.; Jiao, W.; Liu, X.; Yang, W. Metal-Organic Framework Nanosheets as Building Blocks for Molecular Sieving Membranes. *Science* **2014**, *346* (6215), 1356–1359.

(41) Ranjan, R.; Tsapatsis, M. Microporous Metal Organic Framework Membrane on Porous Support Using the Seeded Growth Method. *Chem. Mater.* **2009**, *21* (20), 4920–4924.

(42) Bachman, J. E.; Smith, Z. P.; Li, T.; Xu, T.; Long, J. R. Enhanced Ethylene Separation and Plasticization Resistance in Polymer Membranes Incorporating Metal–organic Framework Nanocrystals. *Nat. Mater.* **2016**, *15*, 845–849.

(43) Bachman, J. E.; Long, J. R. Plasticization-Resistant Ni_2(dobdc)/Polyimide Composite Membranes for the Removal of CO_2 from Natural Gas. *Energy*

Environ. Sci. Energy Environ. Sci **2016**, *9* (9), 2031–2036.

(44) Rodenas, T.; Luz, I.; Prieto, G.; Seoane, B.; Miro, H.; Corma, A.; Kapteijn, F.; Llabrés i Xamena, F. X.; Gascon, J. Metal – Organic Framework Nanosheets in Polymer Composite Materials for Gas Separation. *Nat. Mater.* **2015**, *14*, 48–55.

(45) Lee, J. S.; Jae, H. K.; Young, J. L.; Nak, C. J.; Kyung, B. Y. Manual Assembly of Microcrystal Monolayers on Substrates. *Angew. Chem. Int. Ed. Engl.* **2007**, *46* (17), 3087–3090.

(46) Mintova, S.; Olson, N. H.; Valtchev, V.; Bein, T. Mechanism of Zeolite A Nanocrystal Formation from Colloids at Room Temperature. *Science* **1999**, *283*, 958–960.

(47) Awala, H.; Gilson, J.-P.; Retoux, R.; Boullay, P.; Goupil, J.-M.; Valtchev, V.; Mintova, S. Template-Free Nanosized Faujasite-Type Zeolites. *Nat. Mater.* **2015**, *14* (4), 447–451.

(48) Zhang, X.; Liu, D.; Xu, D.; Asahina, S.; Cychosz, K. A.; Agrawal, K. V.; Al Wahedi, Y.; Bhan, A.; Al Hashimi, S.; Terasaki, O.; et al. Synthesis of Self-Pillared Zeolite Nanosheets by Repetitive Branching. *Science* **2012**, *336* (6089), 1684–1687.

(49) Choi, M.; Na, K.; Kim, J.; Sakamoto, Y.; Terasaki, O.; Ryoo, R. Stable Single-Unit-Cell Nanosheets of Zeolite MFI as Active and Long-Lived Catalysts. *Nature* **2009**, *461* (7261), 246–249.

(50) Na, K.; Jo, C.; Kim, J.; Cho, K.; Jung, J.; Seo, Y.; Messinger, R. J.; Chmelka, B.

F.; Ryoo, R. Directing Zeolite Structures into Hierarchically Nanoporous Architectures. *Science* **2011**, *333* (6040), 328–332.

(51) Vu, D. Van; Miyamoto, M.; Nishiyama, N.; Ichikawa, S.; Egashira, Y.; Ueyama, K. Catalytic Activities and Structures of Silicalite-1/H-ZSM-5 Zeolite Composites. *Microporous Mesoporous Mater.* **2008**, *115* (1–2), 106–112.

(52) Tsapatsis, M. 2-Dimensional Zeolites. *AIChE J.* **2014**, *60* (7), 2374–2381.

(53) Choi, J.; Jeong, H. .; Snyder, M. A.; Stoeger, J. A.; Masel, R.; Tsapatsis, M. Grain Broundry Defect Elimination in a Zeolite Membrane by Rapid Thermal Processing. *Science* **2009**, *325*, 590–593.

(54) Olson, D. H.; Kokotailo, G. T.; Lawton, S. L.; Meier, W. M. Crystal Structure and Structure-Related Properties of ZSM-5. *J. Phys. Chem.* **1981**, *85* (15), 2238–2243.

(55) Koningsveld, H. Van; Jansen, J. C.; Bekkum, H. Van. The Monoclinic Framework Structure of Zeolite H-ZSM-5. Comparison with the Orthorhombic Framework of as-Synthesized ZSM-5. *Zeolites* **1990**, *10*, 235–242.

(56) Meisel, S. L.; McCullough, J. P.; Lechthaler, C. H.; Weisz, P. B. Gasoline from Methanol in One Step. *Chemtech* **1976**, *6* (2), 86–89.

(57) Fan, W.; Snyder, M. A.; Kumar, S.; Lee, P. S.; Yoo, W. C.; McCormick, A. V.; Lee Penn, R.; Stein, A.; Tsapatsis, M. Hierarchical Nanofabrication of Microporous Crystals with Ordered Mesoporosity. *Nat. Mater.* **2008**, *7* (12), 984–991.

(58) Chen, H.; Wydra, J.; Zhang, X.; Lee, P. S.; Wang, Z.; Fan, W.; Tsapatsis, M.

Hydrothermal Synthesis of Zeolites with Three-Dimensionally Ordered Mesoporous-Imprinted Structure. *J. Am. Chem. Soc.* **2011**, *133* (32), 12390–12393.

(59) Lee, P. S.; Zhang, X.; Stoeger, J. A.; Malek, A.; Fan, W.; Kumar, S.; Yoo, W. C.; Hashimi, S. Al; Penn, R. L.; Stein, A.; et al. Sub-40 Nm Zeolite Suspensions via Disassembly of Three-Dimensionally Ordered Mesoporous-Imprinted Silicalite-1. *J. Am. Chem. Soc.* **2011**, *133* (3), 493–502.

(60) Agrawal, K. V.; Topuz, B.; Jiang, Z.; Nguenkam, K.; Elyassi, B.; Francis, L. F.; Tsapatsis, M. Solution-Processable Exfoliated Zeolite Nanosheets Purified by Density Gradient Centrifugation. *AIChE J.* **2013**, *59* (9), 3458–3467.

(61) Liu, Y.; Li, Y.; Yang, W. Fabrication of Highly B-Oriented MFI Film with Molecular Sieving Properties by Controlled in-Plane Secondary Growth. *J. Am. Chem. Soc.* **2010**, *132*, 1768–1769.

(62) Liu, Y.; Li, Y.; Cai, R.; Yang, W. Suppression of Twins in b-Oriented MFI Molecular Sieve Films under Microwave Irradiation. *Chem. Commun.* **2012**, *48* (54), 6782.

(63) Li, X.; Peng, Y.; Wang, Z.; Yan, Y. Synthesis of Highly b-Oriented Zeolite MFI Films by Suppressing Twin Crystal Growth during the Secondary Growth. *CrystEngComm* **2011**, *13*, 3657.

(64) Pham, T. C. T.; Nguyen, T. H.; Yoon, K. B. Gel-Free Secondary Growth of Uniformly Oriented Silica MFI Zeolite Films and Application for Xylene

Separation. *Angew. Chem. Int. Ed. Engl.* **2013**, *125* (33), 8855–8860.

(65) Hoffmann, R. Small but Strong Lessons from Chemistry for Nanoscience. *Angew. Chem. Int. Ed. Engl.* **2013**, *52* (1), 93–103.

(66) Corma, A.; Fornes, V.; Pergher, S. B.; Maesan, T. L. M.; Buglass, J. G. Delaminated Zeolite Precursors as Selective Acidic Catalysts. *Nature* **1998**, *396*, 353–356.

(67) Marler, B.; Gies, H. Hydrous Layer Silicates as Precursors for Zeolites Obtained through Topotactic Condensation: A Review. *Eur. J. Mineral.* **2012**, *24* (3), 405–428.

(68) Kim, W.; Nair, S. Membranes from Nanoporous 1D and 2D Materials: A Review of Opportunities, Developments, and Challenges. *Chem. Eng. Sci.* **2013**, *104*, 908–924.

(69) Jeong, H.-K.; Nair, S.; Vogt, T.; Dickinson, L. C.; Tsapatsis, M. A Highly Crystalline Layered Silicate with Three-Dimensionally Microporous Layers. *Nat. Mater.* **2003**, *2* (1), 53–58.

(70) Chlubná, P.; Roth, W. J.; Greer, H. F.; Zhou, W.; Shvets, O.; Zukal, A.; Jiří, Č.; Morris, R. E. 3D to 2D Routes to Ultrathin and Expanded Zeolitic Materials. *Chem. Mater.* **2013**, *25*, 542–547.

(71) Möller, K.; Bein, T. Pores within Pores-How to Craft Ordered Hierarchical Zeolites. *Science* **2011**, *333* (6040), 297–298.

(72) Xu, D.; Swindlehurst, G. R.; Wu, H.; Olson, D. H.; Zhang, X.; Tsapatsis, M. On

the Synthesis and Adsorption Properties of Single-Unit-Cell Hierarchical Zeolites made by Rotational Intergrowths. *Adv. Funct. Mater.* **2014**, *24* (2), 201–208.

(73) Hunt, H. K.; Lew, C. M.; Sun, M.; Yan, Y.; Davis, M. E. Pure-Silica Zeolite Thin Films by Vapor Phase Transport of Fluoride for Low-k Applications. *Microporous Mesoporous Mater.* **2010**, *128* (1–3), 12–18.

(74) Lew, C. M.; Cai, R.; Yan, Y. Zeolite Thin Films: From Computer Chips to Space Stations. *Acc. Chem. Res.* **2010**, *43* (2), 210–219.

(75) Varoon, K.; Zhang, X.; Elyassi, B.; Brewer, D. D.; Gettel, M.; Kumar, S.; Lee, J. A.; Maheshwari, S.; Mittal, A.; Sung, C.-Y.; et al. Dispersible Exfoliated Zeolite Nanosheets and Their Application as a Selective Membrane. *Science* **2011**, *334* (6052), 72–75.

(76) Blodgett, K. B. Monomolecular Films of Fatty Acids on Glass. *J. Am. Chem. Soc.* **1934**, *56* (2), 495.

(77) Langmuir, I.; Schaefer, V. J. Activities of Urease and Pepsin Monolayers. *J. Am. Chem. Soc.* **1938**, *60* (6), 1351–1360.

(78) Petty, M. C. *Langmuir-Blodgett Films An Introduction*; Cambridge University Press, 1996.

(79) Morawetz, K.; Reiche, J.; Kamusewitz, H.; Kosmella, H.; Ries, R.; Noack, M.; Brehmer, L. Zeolite Films Prepared via the Langmuir – Blodgett Technique. *Colloids Surf A Physicochem Eng Asp* **2002**, *198–200*, 409–414.

(80) Tosheva, L.; Valtchev, V. P.; Mihailova, B.; Doyle, A. M.; Cnrs, U.-. Zeolite Beta

Films Prepared via the Langmuir-Blodgett Technique. *J. Phys. Chem. C* **2007**, *111*, 12052–12057.

(81) Wang, Z.; Wee, L. H.; Mihailova, B.; Edler, K. J.; Doyle, A. M. Langmuir – Blodgett Deposited Monolayers of Silicalite-1 Seeds for Secondary Growth of Continuous Zeolite Films. *Chem. Mater.* **2007**, *19* (24), 5806–5808.

(82) Wee, L. H.; Wang, Z.; Tosheva, L.; Itani, L.; Valtchev, V.; Doyle, A. M. Silicalite-1 Films with Preferred Orientation. *Microporous Mesoporous Mater.* **2008**, *116* (1–3), 22–27.

(83) Li, J.; Liu, X.; Lv, X.; Zhang, B. Reliable Fabrication of Preferentially B-Oriented Silicalite-1 Monolayers on Various Substrates Using the Langmuir–Blodgett Technique. *Mater. Lett.* **2014**, *124*, 299–301.

(84) Makiura, R.; Motoyama, S.; Umemura, Y.; Yamanaka, H.; Sakata, O.; Kitagawa, H. Surface Nano-Architecture of a Metal-Organic Framework. *Nat. Mater.* **2010**, *9* (7), 565–571.

(85) Imperiali, L.; Liao, K.; Clasen, C.; Fransaer, J.; Macosko, C. W.; Vermant, J. Interfacial Rheology and Structure of Tiled Graphene Oxide Sheets. *Langmuir* **2012**, *28* (21), 7990–8000.

(86) Corma, A.; Díaz, U.; García, T.; Sastre, G.; Velty, A. Multifunctional Hybrid Organic-Inorganic Catalytic Materials with a Hierarchical System of Well-Defined Micro- and Mesopores. *J. Am. Chem. Soc.* **2010**, *132* (42), 15011–15021.

(87) Pham, T. C. T.; Kim, H. S.; Yoon, K. B. Growth of Uniformly Oriented Silica MFI

and BEA Zeolite Films on Substrates. *Science* **2011**, *334* (6062), 1533–1538.

(88) Nagahara, L. A.; Fujishima, A.; Snowden-lfft, D.; Price, P. B. Mica Etch Pits as a Height Calibration Source for Atomic Force Microscopy. *J Vac Sci Technol B Nanotechnol Microelectron* **1994**, *12* (3), 1694.

(89) Kumar, P.; Agrawal, K. V.; Tsapatsis, M.; Mkhoyan, K. A. Quantification of Thickness and Wrinkling of Exfoliated Two-Dimensional Zeolite Nanosheets. *Nat. Commun.* **2015**, *6*, 7128–7135.

(90) Geus, E. R.; Bekkum, H. Van. Calcination of Large MFI-Type Single Crystals , Part 2 : Crack Formation and Thermomechanical Properties in View of the Preparation of Zeolite Membranes. *Zeolites* **1995**, *15*, 333–341.

(91) Davis, T. M.; Drews, T. O.; Ramanan, H.; He, C.; Dong, J.; Schnablegger, H.; Katsoulakis, M. A.; Kokkoli, E.; McCormick, A. V.; Penn, R. L.; et al. Mechanistic Principles of Nanoparticle Evolution to Zeolite Crystals. *Nat. Mater.* **2006**, *5* (5), 400–408.

(92) Chaikittisilp, W.; Suzuki, Y.; Mukti, R. R.; Suzuki, T.; Sugita, K.; Itabashi, K.; Shimojima, A.; Okubo, T. Formation of Hierarchically Organized Zeolites by Sequential Intergrowth. *Angew. Chem. Int. Ed. Engl.* **2013**, *52* (12), 3355–3359.

(93) Davis, M. E. Ordered Porous Materials for Emerging Applications. *Nature* **2002**, *417*, 813–821.

(94) Caro, J.; Noack, M.; Kölsch, P.; Schäfer, R. Zeolite Membranes - State of Their Development and Perspective. *Microporous Mesoporous Mater.* **2000**, *38* (1), 3–

24.

(95) Snyder, M. A.; Tsapatsis, M. Hierarchical Nanomanufacturing: From Shaped Zeolite Nanoparticles to High-Performance Separation Membranes. *Angew. Chem. Int. Ed. Engl.* **2007**, *46* (40), 7560–7573.

(96) Rangnekar, N.; Mittal, N.; Elyassi, B.; Caro, J.; Tsapatsis, M. Zeolite Membranes – a Review and Comparison with MOFs. *Chem. Soc. Rev.* **2015**, *44* (20), 7128–7154.

(97) Bein, T. Sythesis and Applications of Molecular Sieve Layers and Membranes. *Chem. Mater.* **1996**, *8* (8), 1636–1653.

(98) Corma, A. State of the Art and Future Challenges of Zeolites as Catalysts. *J. Catal.* **2003**, *216* (1–2), 298–312.

(99) Karwacki, L.; Kox, M. H. F.; De Winter, D. A. M.; Drury, M. R.; Meeldijk, J. D.; Stavitski, E.; Schmidt, W.; Mertens, M.; Cubillas, P.; John, N.; et al. Morphology-Dependent Zeolite Intergrowth Structures Leading to Distinct Internal and Outer-Surface Molecular Diffusion Barriers. *Nat. Mater.* **2009**, *8* (12), 959–965.

(100) Agger, J. R.; Hanif, N.; Cundy, S. C.; Wade, A. P.; Dennison, S.; Rawlinson, P. A.; Anderson, M. W. Silicalite Crystal Growth Investigated by Atomic Force Microscopy. *J. Am. Chem. Soc.* **2003**, *125* (5), 830–839.

(101) Meza, L. I.; Anderson, M. W.; Agger, J. R.; Cundy, C. S.; Chong, C. B.; Plaisted, R. J. Controlling Relative Fundamental Crystal Growth Rates in Silicalite: AFM Observation. *J. Am. Chem. Soc.* **2007**, *129* (49), 15192–15201.

(102) Rangnekar, N.; Shete, M.; Agrawal, K. V.; Topuz, B.; Kumar, P.; Guo, Q.; Ismail, I.; Alyoubi, A.; Basahel, S.; Narasimharao, K.; et al. 2D Zeolite Coatings: Langmuir-Schaefer Deposition of 3 Nm Thick MFI Zeolite Nanosheets. *Angew. Chem. Int. Ed. Engl.* **2015**, *54* (22), 6571–6575.

(103) Lupulescu, A. I.; Rimer, J. D. In Situ Imaging of Silicalite-1 Surface Growth Reveals the Mechanism of Crystallization. *Science* **2014**, *344* (6185), 729–732.

(104) Fedeyko, J. M.; Rimer, J. D.; Lobo, R. F.; Vlachos, D. G. Spontaneous Formation of Silica Nanoparticles in Basic Solutions of Small Tetraalkylammonium Cations. *J. Phys. Chem. B* **2004**, *108* (33), 12271–12275.

(105) Brukett, S. L.; Davis, M. E. Mechanism of Structure Direction in the Synthesis of Pure-Silica Zeolites. 2. Hydrophobic Hydration and Structural Specificity. *Chem. Mater.* **1995**, *7* (2), 1453–1463.

(106) Goretsky, A.; Beck, L.; Zones, S.; Davis, M. Influence of the Hydrophobic Character of Structure-Directing Agents for the Synthesis of Pure-Silica Zeolites. *Microporous Mesoporous Mater.* **1999**, *28* (3), 387–393.

(107) Bonilla, G.; Diaz, I.; Tsapatsis, M.; Jeong, H.; Lee, Y.; Vlachos, D. G. Zeolite (MFI) Crystal Morphology Control Using Organic Structure-Directing Agents. *Chem. Mater.* **2004**, *382* (13), 5697–5705.

(108) Tuel, A.; Taarit, Y. Ben. Synthesis of TS-1 from Titanosilicate Gels Containing TPAOH/TEAOH and TPAOH/NH_4OH Mixtures. *Microporous Mater.* **1993**, *1* (3), 179–189.

(109) Murray, L. J.; Dincă, M.; Long, J. R. Hydrogen Storage in Metal–organic Frameworks. *Chem. Soc. Rev.* **2009**, *38* (5), 1294.

(110) Li, J.-R.; Sculley, J.; Zhou, H. Metal-Organic Frameworks for Separations. *Chem. Rev.* **2012**, *112* (2), 869–932.

(111) Seoane, B.; Coronas, J.; Gascon, I.; Benavides, M. E.; Karvan, O.; Caro, J.; Kapteijn, F.; Gascon, J. Metal–organic Framework Based Mixed Matrix Membranes: A Solution for Highly Efficient CO_2 Capture? *Chem. Soc. Rev.* **2015**, *44* (8), 2421–2454.

(112) Zhao, M.; Wang, Y.; Ma, Q.; Huang, Y.; Zhang, X.; Ping, J.; Zhang, Z.; Lu, Q.; Yu, Y.; Xu, H.; et al. Ultrathin 2D Metal-Organic Framework Nanosheets. *Adv. Mater.* **2015**, *27* (45), 7372–7378.

(113) Wang, X.; Chi, C.; Zhang, K.; Qian, Y.; Gupta, K. M.; Kang, Z.; Jiang, J.; Zhao, D. Reversed Thermo-Switchable Molecular Sieving Membranes Composed of Two-Dimensional Metal-Organic Nanosheets for Gas Separation. *Nat. Commun.* **2017**, *8*, 14460.

(114) Robeson, L. M. The Upper Bound Revisited. *J. Memb. Sci.* **2008**, *320* (1–2), 390–400.

(115) Mahajan, R.; Koros, W. J. Factors Controlling Successful Formation of Mixed-Matrix Gas Separation Materials. *Ind. Eng. Chem. Res.* **2000**, *39* (8), 2692–2696.

(116) Koros, W. J.; Mahajan, R. Pushing the Limits on Possibilities for Large Scale Gas Separation: Which Strategies? *J. Memb. Sci.* **2000**, *175* (1), 181–196.

(117) Galizia, M.; Chi, W. S.; Smith, Z. P.; Merkel, T. C.; Baker, R. W.; Freeman, B. D. 50th Anniversary Perspective : Polymers and Mixed Matrix Membranes for Gas and Vapor Separation: A Review and Prospective Opportunities. *Macromolecules* **2017**, *50* (20), 7809–7843.

(118) Cussler, E. L. Membranes Containing Selective Flakes. *J. Memb. Sci.* **1990**, *52*, 275–288.

(119) Jeong, H.-K.; Krych, W.; Ramanan, H.; Nair, S.; Marand, E.; Tsapatsis, M. Fabrication of Polymer/Selective-Flake Nanocomposite Membranes and Their Use in Gas Separation. *Chem. Mater.* **2004**, *16* (9), 3838–3845.

(120) Choi, S.; Coronas, J.; Jordan, E.; Oh, W.; Nair, S.; Onorato, F.; Shantz, D. F.; Tsapatsis, M. Layered Silicates by Swelling of AMH-3 and Nanocomposite Membranes. *Angew. Chem. Int. Ed. Engl.* **2008**, *47* (3), 552–555.

(121) Li, P.-Z.; Maeda, Y.; Xu, Q. Top-down Fabrication of Crystalline Metal–organic Framework Nanosheets. *Chem. Commun.* **2011**, *47* (29), 8436.

(122) Toby, B. H.; Von Dreele, R. B. GSAS-II: The Genesis of a Modern Open-Source All Purpose Crystallography Software Package. *J. Appl. Crystallogr.* **2013**, *46* (2), 544–549.

(123) Mori, W.; Inoue, F.; Yoshida, K.; Nakayama, H.; Takamizawa, S.; Kishita, M. Synthesis of New Adsorbent Copper(II) Terephthalate. *Chem. Lett.* 1997, 1219–1220.

(124) Xin, Z.; Bai, J.; Shen, Y.; Pan, Y. Hierarchically Micro- and Mesoporous

Coordination Polymer Nanostructures with High Adsorption Performance. *Cryst. Growth Des.* **2010**, *10* (6), 2451–2454.

(125) Yim, C.; Jeon, S. Direct Synthesis of Cu-BDC Frameworks on a Quartz Crystal Microresonator and Their Application to Studies of n-Hexane Adsorption. *RSC Adv.* **2015**, *5* (83), 67454–67458.

(126) Carson, C. G.; Hardcastle, K.; Schwartz, J.; Liu, X.; Hoffmann, C.; Gerhardt, R. A.; Tannenbaum, R. Synthesis and Structure Characterization of Copper Terephthalate Metal-Organic Frameworks. *Eur. J. Inorg. Chem.* **2009**, 2338–2343.

(127) Carson, C. G.; Brunnello, G.; Lee, S. G.; Jang, S. S.; Gerhardt, R. A.; Tannenbaum, R. Structure Solution from Powder Diffraction of Copper 1,4-Benzenedicarboxylate. *Eur. J. Inorg. Chem.* **2014**, 2140–2145.

(128) Seki, K.; Takamizawa, S.; Mori, W. Characterization of Microporous Copper(II) Dicarboxylates (Fumarate, Terephthalate, and Trans-1,4-Cyclohexanedicarboxylate) by Gas Adsorption. *Chem. Lett.* **2001**, 122–123.

(129) Chung, T. S.; Chan, S. S.; Wang, R.; Lu, Z.; He, C. Characterization of Permeability and Sorption in Matrimid/C_{60} Mixed Matrix Membranes. *J. Memb. Sci.* **2003**, *211* (1), 91–99.

(130) Zhang, Y.; Musselman, I. H.; Ferraris, J. P.; Balkus, K. J. Gas Permeability Properties of Matrimid® Membranes Containing the Metal-Organic Framework Cu-BPY-HFS. *J. Memb. Sci.* **2008**, *313* (1–2), 170–181.

(131) Hacarlioglu, P.; Toppare, L.; Yilmaz, L. Effect of Preparation Parameters on

Performance of Dense Homogeneous Polycarbonate Gas Separation Membranes. *J. Appl. Polym. Sci.* **2003**, *90* (3), 776–785.

(132) Yang, Y.; Goh, K.; Wang, R.; Bae, T.-H. High-Performance Nanocomposite Membranes Realized by Efficient Molecular Sieving with CuBDC Nanosheets. *Chem. Commun.* **2017**, *53* (30), 4254–4257.

(133) Sheffel, J. A.; Tsapatsis, M. A Model for the Performance of Microporous Mixed Matrix Membranes with Oriented Selective Flakes. *J. Memb. Sci.* **2007**, *295* (1–2), 50–70.

(134) Sheffel, J. A.; Tsapatsis, M. A Semi-Empirical Approach for Predicting the Performance of Mixed Matrix Membranes Containing Selective Flakes. *J. Memb. Sci.* **2009**, *326* (2), 595–607.

(135) Mahajan, R.; Koros, W. J. Mixed Matrix Membrane Materials with Glassy Polymers. Part 1. *Polym. Eng. Sci.* **2002**, *42* (7), 1420–1431.

(136) Moore, T. T.; Koros, W. J. Non-Ideal Effects in Organic-Inorganic Materials for Gas Separation Membranes. *J. Mol. Struct.* **2005**, *739* (1–3), 87–98.